

The role of the electron trajectory in scanning tunneling microscopy : elastic and inelastic tunneling through NO on Rh(111)

Citation for published version (APA):

Hagelaar, J. H. A. (2008). *The role of the electron trajectory in scanning tunneling microscopy : elastic and inelastic tunneling through NO on Rh(111)*. [Phd Thesis 1 (Research TU/e / Graduation TU/e), Applied Physics and Science Education]. Technische Universiteit Eindhoven. <https://doi.org/10.6100/IR633633>

DOI:

[10.6100/IR633633](https://doi.org/10.6100/IR633633)

Document status and date:

Published: 01/01/2008

Document Version:

Publisher's PDF, also known as Version of Record (includes final page, issue and volume numbers)

Please check the document version of this publication:

- A submitted manuscript is the version of the article upon submission and before peer-review. There can be important differences between the submitted version and the official published version of record. People interested in the research are advised to contact the author for the final version of the publication, or visit the DOI to the publisher's website.
- The final author version and the galley proof are versions of the publication after peer review.
- The final published version features the final layout of the paper including the volume, issue and page numbers.

[Link to publication](#)

General rights

Copyright and moral rights for the publications made accessible in the public portal are retained by the authors and/or other copyright owners and it is a condition of accessing publications that users recognise and abide by the legal requirements associated with these rights.

- Users may download and print one copy of any publication from the public portal for the purpose of private study or research.
- You may not further distribute the material or use it for any profit-making activity or commercial gain
- You may freely distribute the URL identifying the publication in the public portal.

If the publication is distributed under the terms of Article 25fa of the Dutch Copyright Act, indicated by the "Taverne" license above, please follow below link for the End User Agreement:

www.tue.nl/taverne

Take down policy

If you believe that this document breaches copyright please contact us at:

openaccess@tue.nl

providing details and we will investigate your claim.

The role of the electron trajectory in scanning tunneling microscopy

elastic and inelastic tunneling through NO on Rh(111)

PROEFSCHRIFT

ter verkrijging van de graad van doctor
aan de Technische Universiteit Eindhoven,
op gezag van de Rector Magnificus,
prof.dr.ir. C.J. van Duijn,
voor een commissie aangewezen
door het College voor Promoties
in het openbaar te verdedigen
op maandag 31 maart 2008 om 16.00 uur

door

Joris Hubertus Antonius Hagelaar

geboren te Geldrop

Dit proefschrift is goedgekeurd door de promotor:

prof.dr.ir. R.A.J. Janssen

Copromotor:

dr.ir. C.F.J. Flipse

CIP-DATA LIBRARY TECHNISCHE UNIVERSITEIT EINDHOVEN

Hagelaar, Joris Hubertus Antonius

The role of the electron trajectory in scanning tunneling microscopy : elastic and inelastic tunneling through NO on Rh(111) / by Joris Hagelaar. - Eindhoven : Technische Universiteit Eindhoven, 2008.

Proefschrift.

ISBN 978-90-386-1234-8

NUR 924

Trefwoorden: rastertunnelmicroscopie / stikstofoxiden / rhodium / simulatie / intermoleculaire wisselwerkingen / vibratiespectroscopie

Subject headings: scanning tunneling microscopy / nitric oxide / rhodium / simulation / lateral interaction / inelastic electron tunneling spectroscopy

Printed by *Gildeprint*, Enschede

This research was financially supported by the stichting voor fundamenteel onderzoek der materie (FOM).

Contents

1	Introduction	1
1.1	Catalysis	1
1.2	STM	4
1.3	Inelastic electron tunneling spectroscopy	5
	References	6
2	Background on STM	9
2.1	Scanning tunneling microscopy	9
2.2	Scanning tunneling spectroscopy	13
2.2.1	Measuring the LDOS of the sample	14
2.2.2	Inelastic electron tunneling spectroscopy	14
2.3	Experimental	19
2.3.1	The STM set-up	19
2.3.2	Sample preparation	19
2.3.3	Tip preparation	21
	References	23
3	Determination of adsorbate lateral interactions	27
3.1	Introduction	27
3.2	Computational details	30
3.2.1	Determination of lateral interactions	30
3.2.2	Kinetic Monte Carlo simulations	31
3.3	Results and discussion	34
3.3.1	Simulations	34
3.3.2	Experiment	47
3.4	Conclusion	52
	References	53
4	STM appearances of NO on Rh(111)	59
4.1	Introduction	59
4.2	Experiment	60
4.3	Theory	61
4.3.1	GREEN formalism	61
4.3.2	Extended Hückel theory	64
4.3.3	STM configurations	66

CONTENTS

4.4	Results and discussion	68
4.4.1	(2 × 2) – 2NO	68
4.4.2	(4 × 2) – 4NO	83
4.5	Conclusion	86
	References	88
5	STM-IETS on NO on Rh(111)	93
5.1	Introduction	93
5.2	Results and discussion	96
5.2.1	Loss peaks coming from the molecules on the substrate	96
5.2.2	Loss peaks coming from a tip adsorbate	106
5.3	Conclusion	114
	References	115
	Appendix A Using a Lock-in amplifier to measure $\frac{dI}{dV}$ and $\frac{d^2I}{dV^2}$	119
	Appendix B Other experimental structures	123
	Summary	127
	Samenvatting	131
	Dankwoord	135
	Curriculum Vitae	137

Chapter 1

Introduction

In this thesis the system of nitric oxide (NO) adsorbed on the Rh(111) sample surface is used as a model system for studying different phenomena. The importance in car catalytic converters strongly motivated the choice for this combination of metal and molecule. Furthermore, binding upright on specific adsorption sites on the sample surface, the NO molecule is the ideal candidate to use for well-defined STM experiments. Finally, because diatomic molecules only have a few vibrational modes, the interpretation of the obtained vibrational spectra can provide more insight into the selection rules in inelastic electron tunneling spectroscopy (IETS). In this chapter, each of these topics is introduced, the position of the field is sketched and the contribution of this work is highlighted.

1.1 Catalysis

Catalysis is almost everywhere: from the petrochemical industry on the large scale, where zeolite is used to crack large hydrocarbon molecules, down to the cell in which enzymes are the catalysts of the metabolic pathway. In fact, over 80% of our chemical products is produced using catalysis.

Generally, a catalyst is a substance that accelerates a chemical reaction without being consumed. When a molecule binds to a catalyst, one or more of its internal bonds is weakened. As it is easier to break a weak bond, catalysts facilitate chemical reactions. After reacting, the reaction products desorb thereby restoring the catalyst

1. Introduction

and a new reaction cycle can take place.

Together with carbon monoxide (CO) and hydrocarbon compounds, NO is one of the gases produced in a combustion engine of a car that are responsible for air pollution such as smog or acid rain. Therefore, it is desirable to remove these gases before they exit the exhaust and this is where the car catalyst comes in. Adsorption of an NO molecule on the catalyst's surface at elevated temperatures will break the molecule's internal bond. As a result it falls apart in an N and an O atom. When two N atoms meet on the surface, they will react into N₂ and desorb. The O atom will usually react with the other molecules present on the catalyst's surface such as CO and hydrocarbons, and comes off in the form of CO₂ or H₂O. From the platinum group metals, rhodium is the most effective catalyst to reduce NO.

In order to understand how a catalyst can weaken a molecule's chemical bond, it is instructive first to look at the bonds in an isolated molecule. Imagine bringing two atoms so close together that their atomic orbitals will start to overlap. This overlap results in two new types of orbitals, called molecular orbitals (MO): one with a lower and one with a higher energy than the individual atomic orbitals. This is illustrated in Fig. 1.1(a). The low energy MO is called the bonding and the high energy MO anti-bonding orbital. In the bonding orbital the electrons are located mainly in the area between the atomic nuclei, acting as the glue that keeps the atoms bonded. In the anti-bonding orbital, however, the electrons are localized around their own nucleus thereby destabilizing the molecular bond. Since both MOs are originating from the same atomic orbitals, they usually have the same name. In order to make the distinction, the anti-bonding state is indicated by an asterisk.

The electronic configuration of the NO molecule consists of five pairs of bonding and anti-bonding orbitals, originating from the overlap of the five atomic orbitals (1s, 2s, 2p_x, 2p_y and 2p_z) of the separate N and O atom. The fifteen electrons of the atoms are redistributed over the MOs according to the Hund's rule. This is illustrated in Fig. 1.1(b). Note that when an MO is symmetric around the axis of the molecule, it is called a σ bond whereas π orbitals do not have this symmetry. The subscript of the orbital names in Fig. 1.1(b) indicates what atomic orbitals the MO is originating from.

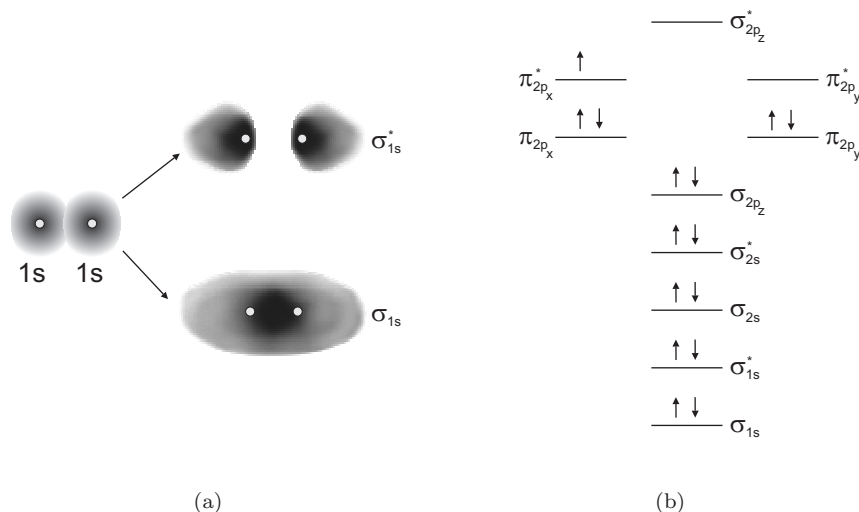


Figure 1.1: (a) When two atomic orbitals overlap, a low energy bonding and high energy anti-bonding molecular orbital will form. The small bright dots represent the atomic nuclei. In (b), the electronic configuration of the NO molecule is shown.

The stability of the molecule can be expressed by the bond order: the number of electrons occupying the bonding orbitals minus the ones occupying the anti-bonding state divided by two. The higher this number, the more stable the bond. If the bond order is negative or zero, the molecule will not form. Indeed with a bond order of 2.5, the NO molecule is stable.

Now, using the electronic picture of NO, the catalytic function of the rhodium can be understood. According to the Blyholder model [1], the NO molecule will donate electrons from its σ_{2p_z} orbital to the metal when it binds to the rhodium substrate. From the metal there is a back donation of electrons into the anti-bonding $\pi_{2p_{xy}}^*$ of the molecule. Overall, the bond order is lowered causing a weakening of the molecular bond. For a detailed description of the bonding of NO on the Rh(111) surface, see [2].

It is important to note that not only the catalyst itself is changing the reactivity of a molecule. When two molecules are adsorbed close together on the catalyst surface, their lateral interaction also influences their binding strength, affecting the activation energies and hence the reaction rates. Therefore it is important to quantify these lateral interactions.

1. Introduction

In chapter 3 of this work, the lateral interactions between NO molecules on the Rh(111) substrate are studied. As lateral interactions are responsible for a specific ordering of the molecules on the surface, the structures obtained by simulation using calculated values for the interactions can be directly compared to experimentally observed configurations. The match between theory and experiment gives good confidence in the values for the calculated interactions.

It must be noted that there is a large difference between the conditions under which the catalyst normally operates and fundamental experimental studies are performed. An industrial catalyst usually consists of small metal particles that are dispersed over a porous ceramic material in order to maximize the active surface area. Furthermore it operates in a high pressure ($p \approx 1$ bar) mixture of gases. Systematic studies, however, require a well-defined system. Therefore, the small particles are replaced by a piece of single crystal material with known orientation. The gas the single crystal is exposed to usually consists of only one or two different components. In order to prevent contamination of the sample surface by air, these experiments are mostly conducted under high vacuum conditions ($p < 10^{-6}$ mbar) [3, 4]. These differences in pressure and shape of the catalyst could make the model catalyst behave differently from the industrial one [5]. Nevertheless, data obtained from fundamental investigations provide a better understanding of the processes on a molecular level so that these kinds of studies still contribute significantly to the unraveling of the highly complex catalytic reactions.

1.2 STM

The experiments throughout this study are performed using a scanning tunneling microscope (STM) [6]. Most surface sensitive techniques, such as low energy electron diffraction (LEED), high resolution electron energy loss spectroscopy (HREELS) or temperature programmed desorption (TPD) only give information averaged over a certain macroscopic area (typically 1 mm^2) of the surface. The STM, however, makes it possible to locally study the system in real space. An example is the study of a phase transition between two different structures of NO on Rh(111) in which the

1.3 Inelastic electron tunneling spectroscopy

nucleation and growth of patches was observed [7]. However, the STM is not only used to passively study the surface [8], the tip itself can even be used to actively bring atoms and molecules together [9, 10] and make them react [11, 12].

However, despite these great possibilities, the presence of the tip also makes the STM a complex tool. After all, as opposed to light or electron microscopy, the appearance of the topographic image in STM does not only depend on the sample, but also on the tip. A change in the electronic structure of the tip may lead to another type of imaging of the surface. The role of the tip in the appearance of the STM imaging is studied in detail in chapter 4 and the experimentally found images could be well reproduced theoretically. It is found that electrons can take several pathways to tunnel from tip to sample or vice versa. Due to the wave-like nature of particles in quantum mechanics, these different electron trajectories can give rise to interference effects. For some tips, these effects are so strong that they completely dominate the image. As a result the bright spots in the topographic image do not correspond to the positions of the molecules. Ultimately this could result in misinterpretation of the measured data.

1.3 Inelastic electron tunneling spectroscopy

In inelastic electron tunneling spectroscopy (IETS), vibrations of molecules adsorbed inside a metal-oxide-metal tunnel junction can be detected from the I-V curve [13]. Only recently, the STM gained enough stability to use its great zooming capability for performing IETS on single molecules [14]. As each molecule has its own fingerprint of vibrational energies, the STM can thus be used as a chemical sensitive microscope. This way, the success of a tip-induced reaction can be checked by looking at vibrations of the bond that should have formed [15].

However, by far not all the possible molecular vibrations are observed in STM-IETS and, as opposed to infrared spectroscopy or HREELS, the selection rules are unknown. A proper understanding of these selection rules will greatly help understanding electron transport through molecules in general. Moreover, it has been suggested that IET is the responsible mechanism behind the sense of smell in mam-

1. Introduction

mals [16, 17]. In this theory, similar to vision, smell is a spectroscopic sense related to the vibrational frequencies of molecular bonds. Instead of the red, blue and green of vision, smell is estimated to have ten vibrational sensitive bands. However, even if a molecule has vibrations in the sensitive area of smell, if they are inactive in IETS, it could not be detected by the nose.

In chapter 5, the NO on Rh(111) system is used to study the selection rules of IETS. As the NO molecule only has a few vibrational modes, the obtained vibrational spectra are relatively easy to interpret. It is shown that the IET intensity is even more sensible to the electronic structure of the tip than the imaging. As the surface is scanned prior to taking an IET spectrum, the topographic data derived in chapter 4 is used to make a correlation between the intensity of the signal and the electron trajectory that is contributing mainly to the current. Based on this information, an attempt is made to understand the selection rules using intuitive arguments. Note that without proper theoretical simulations, this relationship could not be made. Moreover, vibrational contributions from molecules adsorbed at the tip apex were observed. Due to the different adsorption geometry of these molecules, vibrational modes become active that are inactive for molecules adsorbed at the substrate.

References

- [1] G. J. Blyholder, ‘Molecular orbital view of chemisorbed carbon monoxide,’ *J. Phys. Chem.*, **68**, 2772–2777 (1964).
- [2] D. Loffreda, D. Simon and P. Sautet, ‘Molecular and dissociative chemisorption of NO on palladium and rhodium (100) and (111) surfaces: a density-functional periodic study,’ *J. Chem. Phys.*, **108**, 6447–6457 (1998).
- [3] G. A. Somorjai, ‘Modern surface science and surface technologies: an introduction,’ *Chem. Rev.*, **96**, 1223–1235 (1996).
- [4] J. H. Larsen and I. Chorkendorff, ‘From fundamental studies of reactivity on single crystals to the design of catalysts,’ *Surf. Sci. Rep.*, **35**, 163–222 (1999).

1.3 References

- [5] B. E. Bent, ‘Mimicking aspects of heterogeneous catalysis: generating, isolating, and reacting proposed surface intermediates on single crystals in vacuum,’ *Chem. Rev.*, **96**, 1361–1390 (1996).
- [6] G. Binnig, H. Rohrer, C. Gerber and E. Weibel, ‘Surface studies by scanning tunneling microscopy,’ *Phys. Rev. Lett.*, **49**, 57–61 (1982).
- [7] K. B. Rider, K. S. Hwang, M. Salmeron and G. A. Somorjai, ‘Structure and dynamics of dense monolayers of NO adsorbed on Rh(111) in equilibrium with the gas phase in the torr pressure range,’ *Phys. Rev. Lett.*, **86**, 4330 (2001).
- [8] T. Zambelli, J. Trost, J. Wintterlin and G. Ertl, ‘Diffusion and atomic hopping of N atoms on Ru(0001) studied by scanning tunneling microscopy,’ *Phys. Rev. Lett.*, **76**, 795–798 (1996).
- [9] D. M. Eigler and E. K. Schweizer, ‘Positioning single atoms with a scanning tunnelling microscope,’ *Nature*, **344**, 524–526 (1990).
- [10] A. J. Heinrich, C. P. Lutz, J. A. Gupta and D. M. Eigler, ‘Molecule cascades,’ *Science*, **298**, 1381–1387 (2002).
- [11] S. W. Hla, L. Bartels, G. Meyer and K. H. Rieder, ‘Inducing all steps of a chemical reaction with the scanning tunneling microscope tip: towards single molecule engineering,’ *Phys. Rev. Lett.*, **85**, 2777–2780 (2000).
- [12] R. Martel, P. Avouris and I. W. Lyo, ‘Molecularly adsorbed oxygen species on Si(111)-(7×7): STM-induced dissociative attachment studies,’ *Science*, **272**, 385–388 (1996).
- [13] J. Lambe and R. C. Jaklevic, ‘Molecular vibration spectra by inelastic electron tunneling,’ *Phys. Rev.*, **165**, 821–832 (1968).
- [14] B. C. Stipe, M. A. Rezaei and W. Ho, ‘Single-molecule vibrational spectroscopy and microscopy,’ *Science*, **280**, 1732–1735 (1998).
- [15] H. J. Lee and W. Ho, ‘Single-bond formation and characterization with a scanning tunneling microscope,’ *Science*, **286**, 1719–1722 (1999).

1. Introduction

- [16] L. Turin, 'A spectroscopic mechanism for primary olfactory reception,' *Chem. Sens.*, **21**, 773–791 (1996).
- [17] L. Turin, 'A method for the calculation of odor character from molecular structure,' *J. Theor. Biol.*, **216**, 367–385 (2002).

Chapter 2

Background on STM

2.1 Scanning tunneling microscopy

The scanning tunneling microscope (STM) was the first instrument with which atoms could be imaged in real space. It was invented 1981 by Gerd Binnig and Heinrich Rohrer [1] who were awarded the 1986 Nobel prize in physics for it. The operation principle of STM is based on the quantum mechanical phenomenon of tunneling: if a conductive probe (the tip) is brought within a few atomic distances from the sample surface, quantum mechanics allows for transmission of an electron from the tip to the sample through the potential barrier of the vacuum (see Fig. 2.1(a)). In the Newtonian world, a particle can never be in a region where its potential energy U_0 is greater than its total energy E . Although possible in quantum mechanics, the wave function ψ falls off exponentially inside the barrier as:

$$\psi \propto e^{-z\sqrt{\frac{2m(U_0-E)}{\hbar^2}}}, \quad (2.1.1)$$

with z the width of the barrier, m the mass of the electron and $\hbar = \frac{h}{2\pi}$, the reduced Planck constant.

The tunneling current between a metallic STM tip and sample is determined by the amount of energy levels available at the tip and sample at energy E , the so-called density of states (DOS) ρ_t and ρ_s , respectively, and the tunnel probability $|M(E)|^2$. Considering only elastic currents at $T = 0$, this amounts to the well-known Bardeen

2. Background on STM

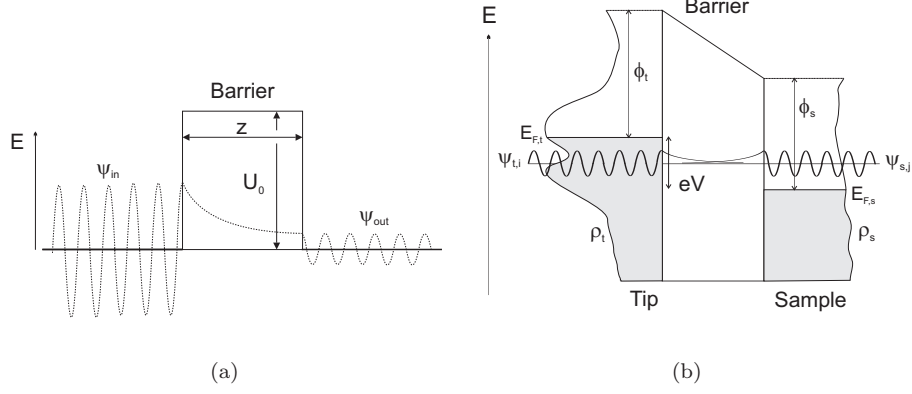


Figure 2.1: (a) Schematic picture showing the tunneling process. The electron's energy is lower than the barrier height. Therefore the amplitude of the incoming free electron wave function ψ_{in} falls off exponentially in the barrier and emerges into the outgoing free electron wave function ψ_{out} with a smaller amplitude. (b) In an STM, the tunneling current is determined by the DOS of both tip and sample (ρ_t and ρ_s) and the transmission probability that includes the amount of overlap of the wave functions. At $T = 0$, the DOS is filled up to the Fermi energy E_F , as is indicated by the shaded area. The work function ϕ is the energy needed to remove an electron at E_F from the metal to the vacuum and can be considered as the barrier height for tunneling.

formula [2]:

$$I = \frac{4\pi e}{\hbar} \int_0^{eV} \rho_s(E_{F,s} + E) \rho_t(E_{F,t} - eV + E) |M(E_{F,s} + E)|^2 dE, \quad (2.1.2)$$

where e is the electronic charge and V is the bias voltage applied between tip and sample. This equation is schematically illustrated in Fig. 2.1(b). The Fermi energy E_F is the energy up to which the DOS is filled and is different for different materials. Upon contact, the Fermi energy of two materials will equalize. However, as one of the contacts is biased, $E_{F,s} = E_{F,t} - eV$. An alternative way of writing the tunneling current gives more insight in the tunnel probability $|M(E)|^2$:

$$I = \frac{2\pi e}{\hbar} \int_0^{eV} \sum_{i,j} |M_{ij}(E_{F,s} + E)|^2 dE. \quad (2.1.3)$$

The tunneling matrix element $M_{ij}(E)$ contains information about the shape (s, p or d-like) of the tip and sample wave functions ($\psi_{t,i}$ and $\psi_{s,j}$ in Fig. 2.1(b), respec-

2.1 Scanning tunneling microscopy

tively) and their overlap at energy E . The Bardeen expression for M is a first order approximation that corresponds to the Fermi golden rule and is written as

$$M_{ij}(E) = -\frac{\hbar^2}{2m} \iint_{d\vec{S}} (\psi_{t,i}^* \nabla \psi_{s,j} - \psi_{s,j} \nabla \psi_{t,i}^*) \delta(E - E_i) \delta(E - E_j). \quad (2.1.4)$$

The surface integral is taken over any arbitrary surface \vec{S} lying entirely within the vacuum barrier region separating tip and sample. Tersoff and Hamann [3] were the first to evaluate M for the STM configuration showing that when the tip wave functions $\psi_{t,i}$ are modeled as a single s-orbital, $M_{ij} = M_j \propto \psi_{s,j}$. Since $|M_j|^2 = |\psi_{s,j}|^2 \equiv \rho_s$, equation (2.1.3), when taken at small bias voltages, simplifies to:

$$I \propto eV \rho_s(E_{F,s}), \quad (2.1.5)$$

i.e., the tunneling current is directly proportional the DOS of the substrate. Extension of the model for any other atomic orbital ($p_x, p_y, p_z, d_{x^2-y^2}, d_{r^2-z^2}, d_{xy}, d_{xz}$ and d_{yz}) showed [4, 5] that equation (2.1.5) only holds for s-orbitals. Generally, the tunneling current at the point where the axes of symmetry in the z -direction of the orbitals of tip and sample coincide, is maximum if the orbitals are symmetric and have the same orientation. If their shape is anti-symmetric or their orientation is orthogonal, the tunneling current is zero. Considering the above, it is clear that M has a large influence on the resolution and appearance of the scan. In chapter 4, the effect of the tip wave function on the image appearance is studied in more detail.

Although the exact details depend on the system to be studied, we can intuitively state that $|M|^2$ is proportional to the overlap of the filled (empty) tip and empty (filled) sample wave functions that decay exponentially into the vacuum. The barrier height U_0 in equation (2.1.1) is approximated to be the average barrier height between tip and sample $\frac{\phi_t + \phi_s + eV}{2}$ (see Fig. 2.1(b)), where the work function ϕ is the minimum energy needed to remove an electron from a material to the vacuum. An experimental $I(z)$ curve in which the tunneling current indeed goes down exponentially with the tip-sample distance is shown Fig. 2.2(a).

This strong distance dependence of the tunneling current is utilized in STM. In constant current mode, the current I is set at a certain setpoint value (typically

2. Background on STM

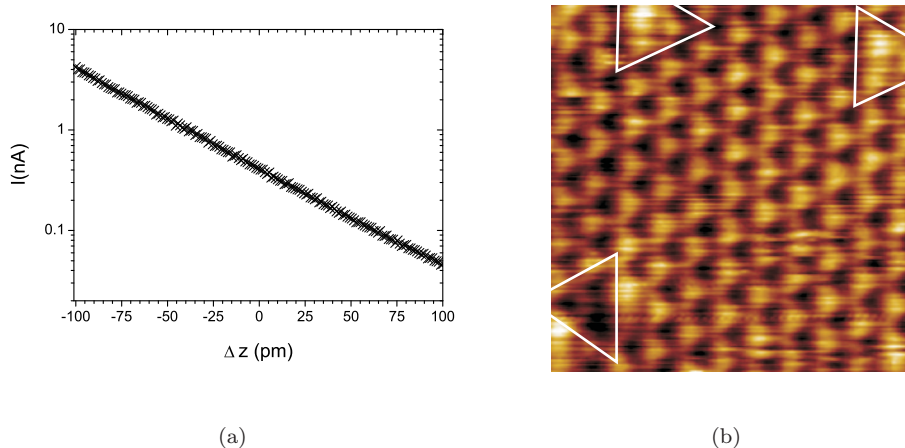


Figure 2.2: (a) Experimentally recorded $I(z)$ curve that shows an exponential behavior as expected from equation (2.1.1). (b) Atomic resolution image ($2.5 \times 2.5 \text{ nm}^2$) showing the hexagonal packing of the rhodium atoms in the (111) surface. White triangles are drawn around anomalies in the lattice. The dark dot in the lower left corner is a vacancy. The two bright spots in the top of the image are attributed to sub-surface impurities. (Scanning parameters $V = 3 \text{ mV}$, $I = 3.95 \text{ nA}$).

ranging from 1 pA to 10 nA). A feedback loop is continuously maintaining the setpoint current by moving the tip towards or away from the substrate, see Fig. 2.3. Accurate tip height displacements (Δz) and scanning movements (x and y) smaller than 10 pm can be accomplished by applying voltages to the piezo-electric scanning tube on which the STM tip is mounted. Typical piezo sensitivities are a few nanometers per applied volt.

As the tip is moved over the sample surface, the change in tip-height Δz is recorded at each point (x, y) . This way a 'topographic' image is created. An atomic resolution image of the freshly cleaned Rh(111) surface is shown in Fig. 2.2(b). Since the tip-sample distance is $z < 1 \text{ nm}$, a good vibrational decoupling of the STM from its environment is an essential condition to prevent the tip from touching the sample.

In the previous sentence, quotes are used around the word topographic since the image does not represent pure topography. As is clear from equations (2.1.1) and (2.1.2), laterally, the tunneling current does not only depend on tip-sample distance z at point (x, y) , but also on the DOS of the sample at that position, the

2.2 Scanning tunneling spectroscopy

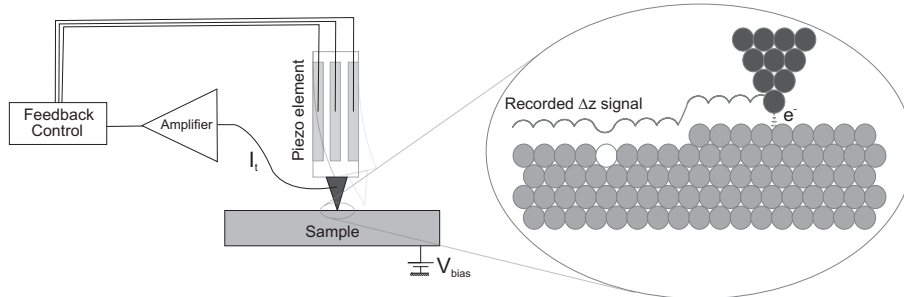


Figure 2.3: Schematic picture of the STM. The feedback control maintains the tunneling current I_t at the setpoint value by moving the tip further from or closer to the substrate. Inset: the z image produced is not a pure topographic one. Schematically this is indicated by the 'recorded Δz signal' in the picture. As long as a substrate consisting of the same material (indicated by grey filled circles) is scanned, the electronic properties do not change too much. Hence, the image gives a good representation of the topography. However, an impurity atom (white filled circle) locally changes the DOS of the sample and could be imaged completely different than might have been expected based on topography.

so-called local DOS or LDOS $\rho_s(x, y)$. As a result the height of the tip will also be adjusted. This is schematically illustrated in the inset of Fig. 2.3. The figure shows the operation principle of STM in general.

2.2 Scanning tunneling spectroscopy

Scanning tunneling spectroscopy (STS) experiments are usually performed to get more information out of the measurement than just a topographic image. In STS, the tip is positioned at an interesting spot on the surface after which the feedback loop is opened (the tunneling current now is allowed to vary), the bias voltage is swept over the energy range of interest and the current is recorded. In the following two subsections it is discussed what kind of information can be obtained from the resulting $I(V)$ curve.

2. Background on STM

2.2.1 Measuring the LDOS of the sample

The first derivative of the $I(V)$ curve gives information about the charge density distribution of a sample surface. In the Tersoff-Hamann approximation,¹ the first derivative of equation (2.1.3) is:

$$\frac{dI}{dV}(V) \propto \rho_s(x, y, E_{F,t} + eV). \quad (2.2.1)$$

This way the LDOS at position (x, y) on the surface can be measured. In determining the LDOS from $\frac{dI}{dV}$, the important information comes from the *elastic* tunnel current, i.e. the electrons that have the same energy before and after tunneling (see Fig. 2.4(a)). Inelastic processes, in which the electron does lose energy are considered below.

2.2.2 Inelastic electron tunneling spectroscopy

In inelastic electron tunneling spectroscopy (IETS), electron loss processes, like molecular vibrations in the tunneling barrier, can be determined from the $I(V)$ curve. It was first demonstrated in 1968 by Jaklevic and Lambe [6] for molecules adsorbed at the metal-insulator interface in a metal-insulator-metal tunnel junction. Because of the complexity of sample preparation and ill defined bonding of the molecules in their environment, the technique was not very popular. This changed in 1998 when the STM gained enough stability [7] to do IETS measurements on single molecules [8]². The STM could now not only scan molecules with sub-angstrom resolution and probe the local electronic properties, but also chemically identify them from their characteristic vibrational energies. However, by far, not all the vibronic modes are observed in STM-IETS. As opposed to other spectroscopic techniques like infrared or Raman spectroscopy, IETS does not have definite selection rules, although, for certain systems propensity rules have recently been derived, based on pathway and symmetry

¹For relatively blunt tips, M has much more s-wave character than for sharp tips. In the latter case, the equation loses validity and the tip DOS has to be taken into account explicitly (equation (2.1.2)) in the observed spectrum.

²parallel to the progress in STM, other techniques like the mechanically controllable break junctions (MCBJ) [9] and micro fabricated electrodes [10] were developed for contacting single molecules. These methods have the advantage of a more symmetric junction. However, it is experimentally very challenging to create a junction with exactly one molecule between the electrodes. In STM, this can be verified by scanning the surface prior to spectroscopy.

2.2 Scanning tunneling spectroscopy

arguments [11, 12, 13].

When a molecule is adsorbed on the substrate, the electrons will tunnel from the tip via the molecular energy level of the adsorbate to the substrate as is illustrated in Fig. 2.4(a). In a tunneling process like this, there are two important time scales: the tunneling traversal time and the dephasing time. The former is the time the electron stays on the molecule during tunneling, whereas the latter is the time it takes for an electron to lose its phase due to interactions. The position of the electronic state of the molecule with respect to the Fermi energy of the leads is E_m . The state has a width Δ that depends on the amount of electronic coupling to the leads. If E_m is large, the electron will tunnel through the tail of the electronic level and the traversing time can be written as $\tau_t \sim \frac{\hbar}{E_m}$. If E_m is small, the width of the electronic level Δ is the important parameter: $\tau_t \sim \frac{\hbar}{\Delta}$. In total we can write [14]:

$$\tau_t = \frac{\hbar}{\sqrt{E_m^2 + \Delta^2}}. \quad (2.2.2)$$

The dephasing time τ_d inversely depends on the electron-phonon coupling parameter M :

$$\tau_d = \frac{\hbar}{M}. \quad (2.2.3)$$

By comparing these times, two regimes can be distinguished.

If $\tau_t \gg \tau_d$ the electronic motion is incoherent and can be described by hopping, where at each site complete local thermalization is achieved. When the electron hops on the bridge state, τ_t is large enough for the molecule to react to the presence of the electron and a charged molecule or polaron will form. If the electronic broadening Δ is smaller than the energy of the vibrational quantum of the molecule $\hbar\omega$, electrons can tunnel directly via the vibronic states of the molecular ion. These states are observed as peaks in the $\frac{dI}{dV}$ signal around the molecule's electronic level [10, 15, 16, 17, 18]. This mechanism is called *resonant* inelastic tunneling spectroscopy (RIETS) and is illustrated in Fig. 2.5.

In the regime of IETS, i.e. when $\tau_t \ll \tau_d$, the molecule does not have time to react to the extra charge. While traversing, the moving electron can only be scattered off

2. Background on STM

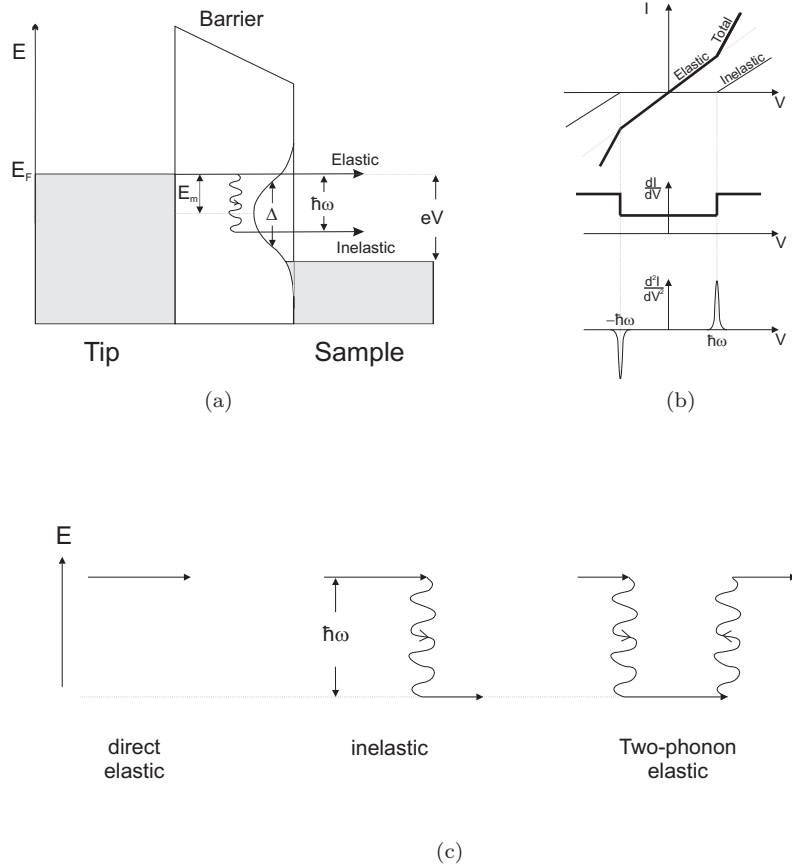


Figure 2.4: (a) Diagram illustrating the mechanism of IETS. When the energy difference between tip and sample is large enough ($eV \geq \hbar\omega$), electrons can excite a vibrational quantum $\hbar\omega$ of the adsorbate and still tunnel into the empty states of the sample. (b) In $I(V)$ curves, inelastic processes emerge as kinks at the vibrational threshold value $\hbar\omega$. These kinks in $I(V)$ show up as steps in the first derivative and peaks in d^2I/dV^2 , that is being measured in practice. (c) If the molecular electronic level is close to resonance ($E_m < 2\Delta$), a third tunneling process becomes important, in which an electron emits and reabsorbs a vibrational quantum while tunneling. In this two-phonon process, the initial and final state of the electron have the same energy and hence, this process is elastic.

2.2 Scanning tunneling spectroscopy

the molecule, leaving it behind in a vibrationally excited state. By exciting the molecule, the electron will lose an energy $\hbar\omega$ equal to the energy of the vibrational quantum of the molecule. After scattering, however, the electron can only proceed to the sample when there is an empty state available, i.e. at $eV \geq \hbar\omega$, as is illustrated in Fig. 2.4(a). When the electron's energy is smaller than $\hbar\omega$, it can only tunnel elastically. At $\hbar\omega$, an extra, inelastic tunneling path opens, giving rise to a kink in the $I(V)$ curve, as is shown in Fig. 2.4(b). A kink in $I(V)$ will show up as a step in $\frac{dI}{dV}$ and a peak in $\frac{d^2I}{dV^2}$ ³, which is the quantity to be measured. Usually, a lock-in amplifier rather than mathematical differentiation is used to measure the derivatives of $I(V)$ directly because of better signal to noise ratios. In appendix A, the principle of this measurement is explained. The change in differential conductance $\Delta\sigma = \Delta(\frac{dI}{dV})$ associated with vibrational excitation is obtained by integrating $\frac{d^2I}{dV^2}$ over the peak area. The normalized change in differential conductance $\frac{\Delta\sigma}{\sigma}$ is obtained by normalizing $\Delta\sigma$ to the conductance below the vibrational excitation energy and is directly proportional to the cross section for inelastic excitation.

At $eV = \hbar\omega$, however, the opening of the inelastic channel does not always lead to an increase in the conductance. This only happens when $E_m > 2\Delta$. If the level is close to resonance, elastic tunneling through virtual emission and reabsorption of a vibrational quantum starts to play an important role [19]. This mechanism of so-called two-phonon elastic tunneling is explained in Fig. 2.4(c). For both direct and two-phonon elastic tunneling, the electron's initial and final states are the same. As IETS processes are coherent processes, electrons taking these different elastic pathways will interfere. The total measured conductance is the sum of the positive inelastic and the interfered elastic signal. As a result, depending on the exact position of E_m with respect to E_F , the peak might change into a dip or derivative-like shape [20, 21, 22, 23].

It is important to note that IETS spectra show up anti-symmetric in bias voltage. In other words, if a peak will show up at $eV = +\hbar\omega$, a dip will appear at $eV = -\hbar\omega$. The height of the peak and dip are generally not the same due to the asymmetry in

³In point contact spectroscopy like MCBJ, the transmission probability for an electron is nearly 1, as opposed to STM. Because of this strong coupling, the states that are supposed to be filled in the energy window, could be partially depleted, and hence both contacts will contain empty states. In this case, the onset of inelastic scattering can give rise to increased reflection and consequently a dip in $\frac{d^2I}{dV^2}$.

2. Background on STM

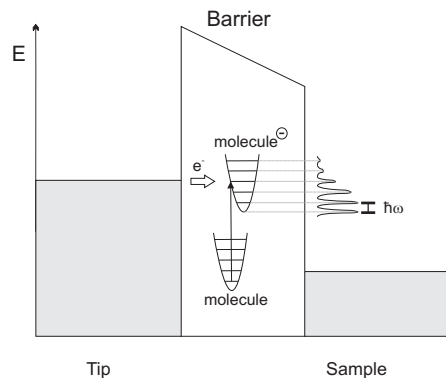


Figure 2.5: Diagram illustrating the mechanism of electron tunneling via a molecule in the regime of $\tau_t \gg \tau_d$. Because τ_t is large, the molecular nuclei have time to respond to the extra charge and a molecular ion will form. This is indicated by the vertical arrow from molecule to molecule^{ominus}. Molecule^{ominus} will have vibronic levels around its electronic level and if $\Delta < \hbar\omega$, these levels can be resolved as peaks in $\frac{dI}{dV}$.

the tunnel junction [24, 25]. Suppose the molecule is adsorbed at the surface. An electron tunneling from tip to adsorbate will tunnel through the barrier at energy E . At the adsorbate it will lose a vibrational quantum of energy $\hbar\omega$ and continues to the substrate. An electron going from sample to tip will first lose $\hbar\omega$ at the molecule before tunneling to the tip at an energy of $E - \hbar\omega$. Equation (2.1.1) shows that the tunneling probability and thus the IETS peak for an electron tunneling with E is higher than with $E - \hbar\omega$.

On top of the natural line width, two experimental parameters contribute to the width of the IETS peak: thermal broadening and modulation voltage broadening. Thermal excitations of electrons across the Fermi level increase the width of the Fermi distribution with temperature. Modulation voltage broadening arises from the amplitude of the AC modulation voltage V_{AC} used to measure the $\frac{d^2I}{dV^2}$ directly using a lock-in amplifier (appendix A). Taking all effects into account the variation in full width half maximum is [6, 24, 26]:

$$W^2 = W_{intrinsic}^2 + (1.7V_{AC})^2 + (5.4kT/e)^2. \quad (2.2.4)$$

2.3 Experimental

2.3.1 The STM set-up

The STM used in this work is a commercial LT-STM from Omicron GmbH. The base pressure in the chamber is $p < 10^{-10}$ mbar. The STM can be cooled down to a minimum operating temperature of 4.8 K by a system of two separate concentric bath cryostats. The outer cryostat is filled by liquid nitrogen. Surrounding the inner cryostat, that is filled by liquid helium (or liquid nitrogen), it acts as a heat shield. The STM is mounted in two copper cups that are attached below and in thermal contact with the cryostats. Working at low temperature together with an efficient vibration isolation using spring suspension with eddy current damping, average drifts of $< 2 \text{ \AA}/\text{hour}$ can be reached [27]. A detail of the set-up is shown in Fig. 2.6 for clarification.

Molecules can be deposited in situ by a tube connected to a variable leak valve that can be screwed in through a hole in the radiation shields down to a minimum distance of 5 mm from the sample, as is illustrated in Fig. 2.6. However, as the surfaces of the cups and cryostats are cold, the sticking probability of the molecules will be close to 1 everywhere, preventing them from forming a homogeneous pressure inside the cold space. As a result, the exposure of the sample to the gas cannot be quantified.

Moreover, the configuration of the STM is such, that the tip has to be present in the STM during exposure of the gas to the substrate. Consequently, not only the sample surface, but also the tip itself will be covered by molecules. A tip that is terminated by a molecule has localized states that might have a great influence on both imaging and spectroscopy (equation (2.1.2)). This influence of adsorbates on the tip will be further discussed in chapter 4 and 5.

2.3.2 Sample preparation

A clean Rh(111) single crystal was mounted on a sample plate and is cleaned by repeated cycles of Ar^+ sputtering at 500°C ($1.5 \mu\text{A}$ for 90 minutes) and annealing at 500, 600 and 700°C , 20 minutes for each temperature. The sample was then flashed

2. Background on STM

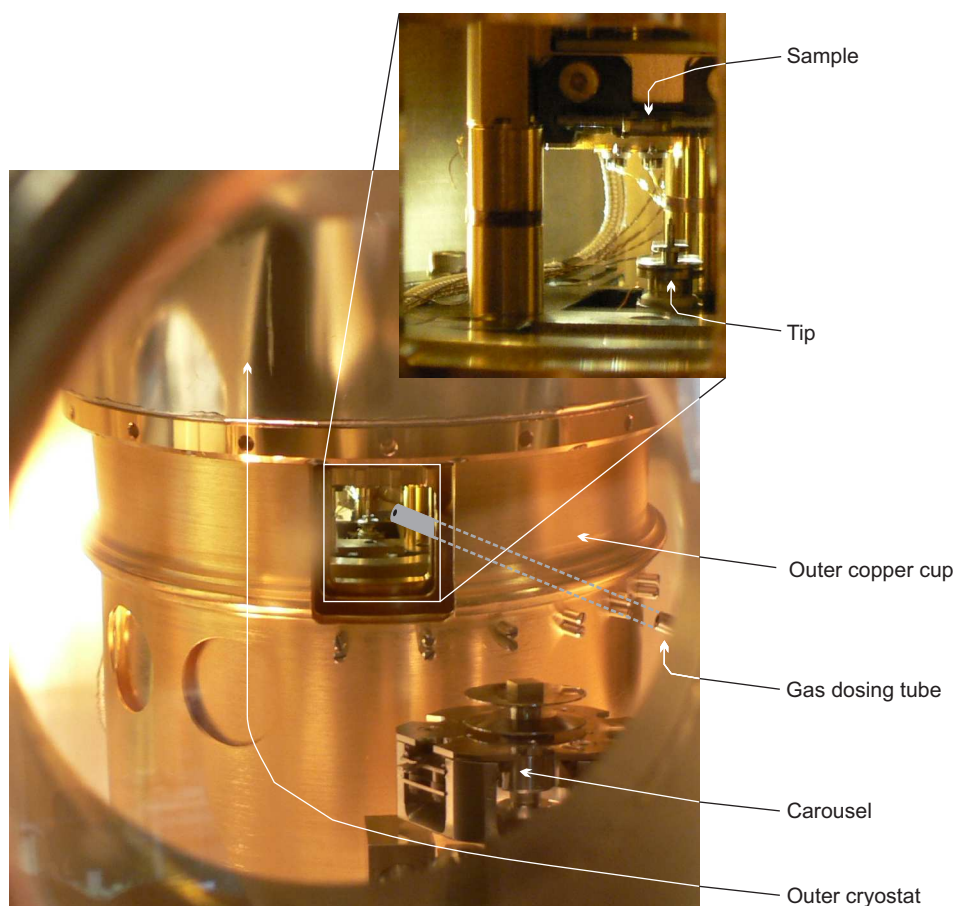


Figure 2.6: Implementation of the STM in the Omicron GmbH LT-STM. The STM is mounted in two copper cups in thermal contact with the cryostats. Protecting from significant thermal input, the cold walls of these cups ensure the space within to stay in thermal equilibrium as long as the cryostats are filled. Gas molecules can be deposited on the sample in situ by a the gas dosing tube, that can be screwed in through a hole in the copper cups to a minimum distance of 5 mm from the sample, as is schematically depicted. All openings in the cups can be closed by a door facilitating easy tip and sample exchange between STM and carousel. The inset shows the tip and the sample.

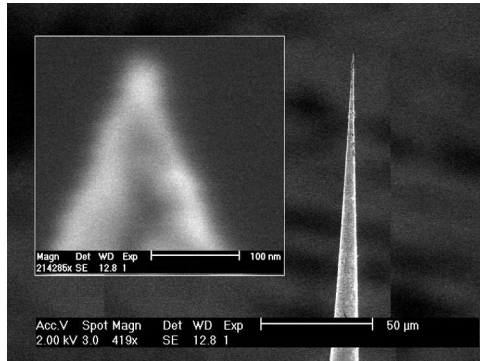


Figure 2.7: SEM picture of an etched tip. The inset shows a zoom on the tip apex, the scale bar is 100 nm, meaning that the radius of curvature of the tip is around ~ 15 nm. The fuzzy white area around the tip is tungsten oxide WNO_3 that is removed by heating before using it in the STM experiment.

to 1200°C . The $\text{Ag}(100)$ sample was cleaned by repeated cycles of Ar^+ sputtering at room temperature and subsequent annealing at 500°C . Each procedure in the cycle is done for about 30 minutes.

An STM image of the clean $\text{Rh}(111)$ surface showing atomic resolution is depicted in Fig. 2.2(b). Three lattice anomalies are indicated by white triangles. The dark dot in the lower left corner is a vacancy, the other two bright dots in the top of the image are attributed to subsurface impurities. Studies of clean $\text{Pd}(111)$ [28] showed subsurface impurities (O, S and Si) that resemble the ones observed in Fig. 2.2(b). These impurities locally change the LDOS, enhancing or inhibiting molecular adsorption and reaction on the surface. The density of subsurface impurities is however determined to be less than 2%, meaning that their overall influence on the formation of molecular structures will be small.

2.3.3 Tip preparation

The tips are electrochemically etched from polycrystalline tungsten wire ($\varnothing 0.35$ mm), using the standard etching techniques (see for instance [29]). After etching, the tips were rinsed with water and blown dry with nitrogen. An example of an etched tip is shown in Fig. 2.7. To remove the tungsten oxide (WNO_3) layer that forms in air, the tips are heated up to temperatures $> 1200^\circ\text{C}$, above which the WNO_3 sublimates and

2. Background on STM

a clean tungsten tip will result.

The electron beam heater that is used for this is normally used solely for heating samples as is illustrated in Fig. 2.8(a): the heater consists of a thoriated tungsten filament, biased at a negative voltage of -650 V. It is positioned right under the sample stage that is grounded. When a current is run through the filament, electrons will escape the wire and are accelerated towards the sample. This way, sample temperatures of 1200°C can be reached.

Tips are mounted in tip transfer plates to facilitate easy handling inside the vacuum. As opposed to a single sample plate, the Omicron GmbH tip transfer plate consists of a double plate design. The tips are held in place by a magnet. In order to heat the tip, both the tip transfer plate and the electron beam heater were modified (see Fig. 2.8(b)). The sample stage was electrically connected to the filament at -650 V and an isolated contact spring was added to the stage to contact the top plate of the tip transfer plate to a voltage of +650 V. In order to prevent a short-circuit between the top and bottom plate, they were electrically isolated from each other. Furthermore, an extra plate similar to the top plate was put in between the top and bottom plate and biased at -650 V. This way, the entire space between the filament and the second plate has a potential of -650 V, except for the tip, which is at +650 V. The total potential difference of 1300 V together with the sharpness of the tip creates a large field around the region of the tip, focussing all the electrons at the tip end (see Fig. 2.8(b)). This way, only the tip itself is heated to temperatures larger than 1300°C. Finally, as the magnet that is used in the original design to hold the tip in place would be heated well above the Curie temperature, it is replaced by a spring. Toggling from the tip to sample heating configuration is done by a switch on the electronics of the heater.

After heating, the tip is mounted in the STM. There, the tip apex can be further modified/sharpened in two ways. The first option is the generation of a high electric field at the tip apex by applying voltage pulses up to ± 10 V between tip and sample. Dipping the tip into the metal (up to 2 nm) is a second way of tip modification. As tungsten is usually harder than the substrate metal material, a neck consisting of substrate material will be pulled during retraction of the tip. When the neck breaks,

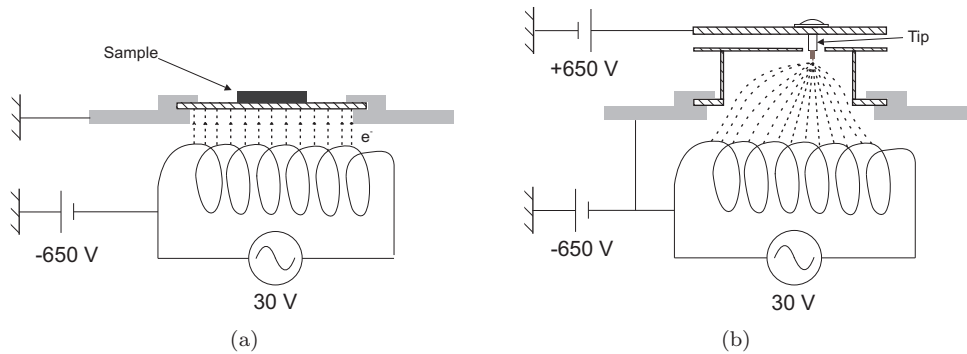


Figure 2.8: In (a) the normal operation of the e-beam heater for heating samples. In (b) the modified e-beam heater that is made suitable for heating tips as well. The gray area is the sample stage, the hashed objects are the sample (a) or tip transfer plate (b) and the dotted lines represent the electric field lines.

a sharp tip will result. Note that using this method, the apex of the tip will be contaminated with atoms of the substrate material.

References

- [1] G. Binnig, H. Rohrer, C. Gerber and E. Weibel, ‘Surface studies by scanning tunneling microscopy,’ *Phys. Rev. Lett.*, **49**, 57–61 (1982).
- [2] C. J. Chen, *Introduction to scanning tunneling microscopy*, Oxford University Press, New York (1993).
- [3] J. Tersoff and D. R. Hamann, ‘Theory and application for the scanning tunneling microscope,’ *Phys. Rev. Lett.*, **50**, 1998–2001 (1983).
- [4] C. J. Chen, ‘Theory of scanning tunneling spectroscopy,’ *J. Vac. Sci. Technol. A*, **6**, 319–322 (1988).
- [5] C. J. Chen, ‘Tunneling matrix elements in three-dimensional space: The derivative rule and the sum rule,’ *Phys. Rev. B*, **42**, 8841–8857 (1990).
- [6] J. Lambe and R. C. Jaklevic, ‘Molecular vibration spectra by inelastic electron tunneling,’ *Phys. Rev.*, **165**, 821–832 (1968).

2. Background on STM

- [7] B. C. Stipe, M. A. Rezaei and W. Ho, ‘A variable-temperature scanning tunneling microscope capable of single-molecule vibrational spectroscopy,’ *Rev. Sci. Instr.*, **70**, 137–143 (1999).
- [8] B. C. Stipe, M. A. Rezaei and W. Ho, ‘Single-molecule vibrational spectroscopy and microscopy,’ *Science*, **280**, 1732–1735 (1998).
- [9] R. H. M. Smit, Y. Noat, C. Untiedt, N. D. Lang, M. C. van Hemert and J. M. van Ruitenbeek, ‘Measurement of a conductance of a hydrogen molecule,’ *Nature*, **419**, 906–909 (2002).
- [10] H. Park, J. Park, A. K. L. Lim, E. H. Anderson, A. P. Alivisatos and P. L. McEuen, ‘Nanomechanical oscillations in a single-C₆₀ transistor,’ *Nature*, **407**, 57–60 (2000).
- [11] A. Troisi and M. A. Ratner, ‘Propensity rules for inelastic electron tunneling spectroscopy of single-molecule transport junctions,’ *J. Chem. Phys.*, **125**, 214709 (2006).
- [12] A. Troisi and M. A. Ratner, ‘Molecular transport junctions: propensity rules for inelastic electron tunneling spectra,’ *Nano Lett.*, **6**, 1784–1788 (2006).
- [13] A. Gagliardi, G. C. Solomon, A. Pecchia, T. Frauenheim, A. D. Carlo, N. S. Hush and J. R. Reimers, ‘A priori method for propensity rules for inelastic electron tunneling spectroscopy of single-molecule conduction,’ *Phys. Rev. B*, **75**, 174306 (2007).
- [14] M. Galperin, M. A. Ratner and A. Nitzan, ‘Molecular transport junctions: vibrational effects,’ *J. Phys.: Condens. Matter*, **19**, 103201 (2007).
- [15] S. W. Wu, G. V. Nazin, X. Chen, X. H. Qiu and W. Ho, ‘Control of relative tunneling rates in single molecule bipolar electron transport,’ *Phys. Rev. Lett.*, **93**, 236802 (2004).
- [16] X. H. Qiu, G. V. Nazin and W. Ho, ‘Vibronic states in single molecule electron transport,’ *Phys. Rev. Lett.*, **92**, 206102 (2004).

2.3 References

- [17] S. Braig and K. Flensberg, ‘Vibrational sidebands and dissipative tunneling in molecular transistors,’ *Phys. Rev. B*, **68**, 205324 (2003).
- [18] M. Galperin, A. Nitzan and M. A. Ratner, ‘Resonant inelastic tunneling in molecular junctions,’ *Phys. Rev. B*, **173**, 045314 (2006).
- [19] B. N. J. Persson and A. Baratoff, ‘Inelastic electron tunneling from a metal tip: the contribution from resonant processes,’ *Phys. Rev. Lett.*, **59**, 339–342 (1987).
- [20] M. Galperin, M. A. Ratner and A. Nitzan, ‘Inelastic electron tunnelling spectroscopy in molecular junctions: peaks and dips,’ *J. Chem. Phys.*, **121**, 11965–11979 (2004).
- [21] A. Bayman, P. K. Hansma and W. C. Kaska, ‘Shifts and dips in inelastic-electron-tunneling spectra due to the tunnel-junction environment,’ *Phys. Rev. B*, **25**, 2449–2454 (1981).
- [22] T. Mii, S. G. Tikhodeev and H. Ueba, ‘Spectral features of inelastic electron transport via a localized state,’ *Phys. Rev. B*, **68**, 205406 (2003).
- [23] J. R. Hahn, H. J. Lee and W. Ho, ‘Electronic resonance and symmetry in single-molecule inelastic electron tunneling,’ *Phys. Rev. Lett.*, **85**, 1914–1917 (2000).
- [24] L. J. Lauhon and W. Ho, ‘Effects of temperature and other experimental variables on single molecule vibrational spectroscopy with the scanning tunneling microscope,’ *Rev. Sci. Instr.*, **72**, 216–223 (2001).
- [25] M. Galperin, A. Nitzan, M. A. Ratner and D. R. Stewart, ‘Molecular transport junctions: asymmetry in inelastic tunneling processes,’ *J. Phys. Chem. B*, **109**, 8519–8522 (2005).
- [26] J. Klein, A. Léger, M. Belin, D. Défourneau and M. J. L. Sangster, ‘Inelastic-electron-tunneling spectroscopy of metal-insulator-metal junctions,’ *Phys. Rev. B*, **7**, 2336–2348 (1973).
- [27] T. Becker, H. Hövel, M. Tschudy and B. Reihl, ‘Applications with a new low-temperature UHV STM at 5 K,’ *Appl. Phys. A*, **66**, S27–S30 (1997).

2. Background on STM

- [28] M. K. Rose, A. Borg, T. Mitsui, D. F. Ogletree and M. Salmeron, ‘Subsurface impurities in Pd(111) studied by scanning tunneling microscopy,’ *J. Chem. Phys.*, **115**, 10927–10934 (2001).
- [29] J. B. Ibe, P. P. Bey Jr., S. L. Brandow, R. A. Brizzolara, N. A. Burnham, D. P. DiLella, K. P. Lee, C. R. K. Marrian and R. J. Colton, ‘On the electrochemical etching of tips for scanning tunneling microscopy,’ *J. Vac. Sci. Technol. A*, **8**, 3570–3575 (1990).

Chapter 3

Determination of adsorbate lateral interactions

3.1 Introduction

The binding strength of molecules adsorbed on a surface can be perturbed by the presence of neighboring species. These lateral interactions between adsorbates can be direct or indirect in nature [1, 2, 3, 4, 5, 6, 7]. Interactions in which the substrate is involved are considered indirect and can be divided into electronic and elastic interactions. Electronic interactions alter the binding strength when a substrate atom is shared by several adsorbates and elastic interactions are binding perturbations due to changes in the substrate's surface geometry induced by other adsorbates. Direct interactions, on the other hand, have an electrostatic or a chemical origin. When the molecules' dipole moments are all oriented in the same direction, the electrostatic dipole-dipole coupling can destabilize the adsorbate-surface bond. Alternating dipoles, however, can stabilize this bond. Finally, chemical interactions arise from the overlap of orbitals of neighboring molecules.

Together, the lateral interactions are responsible for the formation of specific ad-layer structures of the adsorbates on the surface and this relationship will be studied in this chapter. Notice that not only the configuration of the formed structures can be influenced by the interactions but also reaction rates and hence the selectivity of processes. It might even become feasible to make use of them as they can change

3. Determination of adsorbate lateral interactions

reaction routes that would otherwise be unfavorable [8] and in the end, more efficient catalytic processes could be made.

Different techniques can be used to quantify lateral interactions. The experimental results obtained from methods like calorimetry and temperature programmed desorption (TPD) have been simulated by kinetic Monte Carlo (kMC) calculations in order to obtain the lateral interactions by fitting the simulated curve to the experimental one [9, 10]. Field ion microscopy (FIM) and later on scanning tunneling microscopy (STM) were used to derive pairwise lateral interactions from the distribution of molecules over the surface [11, 12, 13, 14, 15]. Here, it is important to note that, at finite temperatures, it is not the adlayer structure with minimal internal energy U that forms, but with minimal free energy:

$$A = U - TS, \tag{3.1.1}$$

where T is the temperature and the entropy $S = k_b \ln \Omega$. Here, k_b is Boltzmann's constant and Ω is the number of microstates the structure visits in the course of its thermal fluctuations. Suppose structure A and B are the only configurations possible for a certain coverage and that $U_A < U_B$ and $S_A < S_B$. Obviously at zero temperature $A = U$ and structure A will form. However, as the importance of the entropy increases with temperature, there is a certain temperature at which structure B has the lowest free energy and prevails. Although the structure having the lowest free energy will form, it is the structure with minimal U from which the lateral interactions should be determined. Usually, the complication of entropic forces is overcome by taking the limit of zero coverage [11, 14, 16]. Theoretically, the lateral interactions can be directly derived from total energy (U) calculations of different coverages using density functional theory (DFT) [17, 18, 19]. The effect of entropy is included by performing kinetic Monte Carlo simulations using the obtained kinetic parameters [20]. Recently, it was shown using STM that pairwise interactions are not always sufficient to describe the formed patterns [16, 17] and many-body effects have to be taken into account.

This chapter focusses on the lateral interactions of NO molecules on a Rh(111) substrate. Similar to [20], three of the above described methods are used to determine the lateral interactions. Experimentally, structures of NO adsorbed at 200 K on a

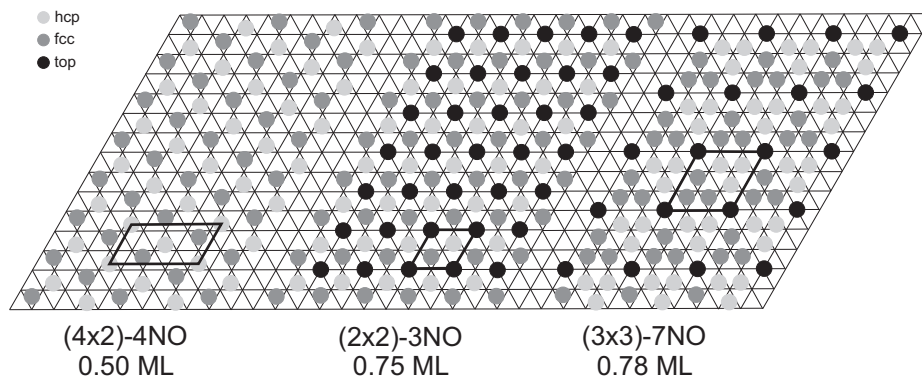


Figure 3.1: Top view of experimentally obtained structures of NO on Rh(111) reported in literature. The grid represents the Rh(111) surface: the intersections of the lines symbolize the top Rh atoms and triangles pointing upwards (downwards) are hcp (fcc) sites. As indicated by the legend, the filled circles represent the NO molecules on one of the three aforementioned adsorption sites. The unit cell of each structure is shown by a black parallelogram. Directly under each structure, its name and coverage are given.

Rh(111) single crystal are studied in real space by STM. On the theoretical side, kMC simulations using DFT derived values for the lateral interactions are performed. As kMC includes entropy effects, the thus calculated structures can be directly compared to the structures observed in the experiment.

From previous studies it is known that NO adsorbs molecularly on Rh(111) at low coverage below $T \sim 250$ K. Two different ordered structures have been reported using LEED [21, 22, 23] and are depicted schematically in Fig. 3.1: at 0.50 ML a zigzag-like $(4 \times 2) - 4\text{NO}$ structure was deduced. In this structure the NO molecules are adsorbed in the fcc and hcp sites of the surface¹. At 0.75 ML, a $(2 \times 2) - 3\text{NO}$ structure is reported in which the NO molecules occupy the fcc, hcp and top positions. The occupation of adsorption sites in between two surface rhodium atoms (bridge sites) is not observed experimentally and therefore not included in this work. A more recent study, to our knowledge the only STM study performed on the system of NO on Rh(111) thus far, showed that at room temperature, patches of the 0.78 ML

¹The (111) surfaces of fcc metals have an ABCABC... stacking sequence. As a result, there are two different threefold coordinated hollow adsorption sites. Hollow sites having an atom directly underneath in the second (B) layer are called hcp sites whereas for fcc sites this atom is located in the third (C) layer. Top adsorption sites are directly on top of the atoms in the first (A) layer.

3. Determination of adsorbate lateral interactions

$(3 \times 3) - 7\text{NO}$ structure (see Fig. 3.1) started to grow from within the $(2 \times 2) - 3\text{NO}$ structure as soon as the torr pressure range was reached [24].

3.2 Computational details

3.2.1 Determination of lateral interactions

Theoretically, the determination of lateral interactions involves two steps. First several adlayer structures of NO on Rh(111) are calculated using the VASP code [25, 26, 27]. It is important to choose adlayer structures of different coverage and different adsorption sites to assure that all possible interactions are taken into account. The second step involves the derivation of the lateral interactions from the DFT calculated adsorption energies which will be explained in the rest of this section.

The influence of the lateral interactions on the average binding strength of an NO molecule in adlayer structure m , E_{ads}^m can be written as:

$$E_{ads}^m = \sum_i b_i^m E_{ads,i}^0 + \sum_n c_n^m \phi_n, \quad (3.2.1)$$

where b_i^m is the fraction of the NO molecules adsorbed at site i in structure m so that $\sum_i b_i^m = 1$ for each m , $E_{ads,i}^0$ is the adsorption energy for an isolated NO molecule at site i , ϕ_n is the lateral interaction of type n and c_n^m is the number of such interactions per NO molecule in structure m . The summation runs in principle over an infinite number of interactions so that E_{ads}^m should approximate the DFT calculated adsorption energy $E_{ads}^{m,DFT}$. The lateral interactions ϕ_n including $E_{ads,i}^0$ are called the kinetic parameters and are obtained by a linear regression procedure in which

$$\chi^2 = \sum_m \left[E_{ads}^m - E_{ads}^{m,DFT} \right]^2 \quad (3.2.2)$$

is minimized.

It is important to know the reliability of the obtained kinetic parameters for the correct prediction of an adlayer energy that has not been taken into account in the DFT calculation. Usually this is checked by cross validation [28, 29, 30, 31], in which the energy of one or more of the DFT calculated structures has to be predicted by the

kinetic parameters without taking them into account in the least squares method of equation (3.2.2). An alternative way of verification is based on Bayesian statistics [32] and is adapted for the reliability calculation of lateral interactions by C. Popa and A. P. J. Jansen [33]. Here, the probability of existence of the lateral interaction can be derived from its prediction of the structural adsorption energies.

3.2.2 Kinetic Monte Carlo simulations

In the kMC simulation, the surface is represented by a lattice in which every point is labeled according to the type of site (hcp, fcc or top) and its occupation. Such a labeled lattice is called a configuration and can be transformed into another one by means of a reaction. The evolution of the system as a function of time can be described by a master equation [34]:

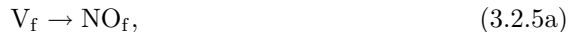
$$\frac{dP_a(t)}{dt} = \sum_{a \neq b} [k_{ba}P_b(t) - k_{ab}P_a(t)]. \quad (3.2.3)$$

Here, $P_a(t)$ denotes the probability to find the system in configuration a at time t , k_{ab} is the transition probability per unit time of the reaction (e.g. adsorption or diffusion) that transfers configuration a into b . This transition probability can be interpreted as a microscopic rate constant and can be described by the Arrhenius equation

$$k_{ab} = \nu_{ab} e^{-\frac{E_{act}}{k_b T}}, \quad (3.2.4)$$

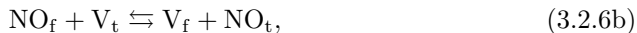
where E_{act} stands for the activation energy, ν_{ab} is the pre-exponential factor of the reaction that transforms a into b , k_b is Boltzmann's constant and T the temperature. Reactions that can occur in our system are:

adsorption:



3. Determination of adsorbate lateral interactions

diffusion:



and desorption:



where V_f , V_h and V_t stand for a vacant and NO_f , NO_h and NO_t for an occupied position of type fcc, hcp or top, respectively. As opposed to diffusion and desorption, adsorption is not a thermally activated but a random process of gas molecules impinging on the surface and therefore has no activation barrier (equation (3.2.4)). If an NO molecule is adsorbed at an energetically unfavorable site, it will either diffuse away or desorb.

The lateral interactions are included in the simulation by changing the activation energy in the rate equation (3.2.4) according to:

$$E_{act} = E_{act}^0 + \alpha \left(\sum_n a_n^f \phi_n - \sum_n a_n^i \phi_n \right). \quad (3.2.8)$$

Here, E_{act}^0 is the activation barrier without lateral interactions, α is the Brønsted-Polanyi parameter, ϕ_n the lateral interaction of type n and $a_n^{i(f)}$ the number of interactions acting on the molecule in the initial (final) state of the reaction. The parameter α is a measure of how much the lateral interactions influence the activation energy, which is the energy of the transition state in a reaction. It can vary between $0 \leq \alpha \leq 1$. If the transition state 'looks' like the initial state, they will both experience the same interactions. Hence, the lateral interactions do not affect this kind of reactions so that $\alpha = 0$. Similarly, $\alpha = 1$ when the transition state is equal to the final state. In our model, desorption of NO molecules from the Rh(111) surface is

3.2 Computational details

direct: molecules go directly to the gas phase and hence, α is taken to be 1. For the process of hopping over the surface from one site to another, α is taken 0.5, so that in the equilibrium diffusion process between the two sites (hopping back and forth), lateral interactions are taken fully into account.

The master equation (3.2.3) is solved using the so-called first reaction method (FRM) [35]. In the FRM a list containing all possible reactions is created. The time for each reaction is computed according to:

$$\Delta t_{ab} = -\frac{1}{k_{ab}} \ln r, \quad (3.2.9)$$

where r is a random number between 0 and 1. Then the following steps are repeatedly carried out:

- (1) The reaction with the shortest reaction time is selected from the list of all reactions.
- (2) The configuration is adjusted according to the reaction.
- (3) The time is set to $t \rightarrow t + \Delta t_{ab}$.
- (4) The event list is recomputed.

In principle, the time obtained from equation (3.2.9) in the kMC simulation can be directly compared to the time of the experiment. However, this can only be done if the reaction constants appearing in equation (3.2.4) are well known for each reaction. Although some value for the diffusion barrier of NO on Rh(111) has been estimated [36], due to the exponential behavior of equation (3.2.4), small deviations from the experimental diffusion barrier will result in orders of magnitude differences in the rate constant. Moreover, as explained in section 2.3.1, the pressure of the NO gas during deposition and hence the adsorption rate cannot be determined in our experiment. Consequently, a direct comparison of times between experiment and simulation is not useful.

However, absolute numbers for the reaction constants are not important for the type of structure that forms. Instead, the formation of a certain structure is completely governed by the difference in free energies between the structures, e.g. the

3. Determination of adsorbate lateral interactions

ratio between structure A and B with free energies A_A and A_B on the surface would be $\frac{\theta_A}{\theta_B} = e^{-(A_A - A_B)/k_b T}$. As these energies only depend on temperature and the kinetic parameters of equation (3.2.1), a structural comparison with the experiment can still be made without knowing the exact reaction constants.

In this study, the activation energy for desorption is chosen to be equal to the adsorption energy of the molecule's adsorption site. The order of magnitude of the prefactors for diffusion and desorption relates to the vibrational frequency of the molecule on the surface, and is typically $\sim 10^{13} \text{ s}^{-1}$. The energy barrier of diffusion is chosen such that diffusion is fast enough to keep the adlayer at equilibrium, but slow enough to speed up the simulation time. The different adsorption energies for the fcc, hcp and top sites are included in diffusion by changing its barrier accordingly.

3.3 Results and discussion

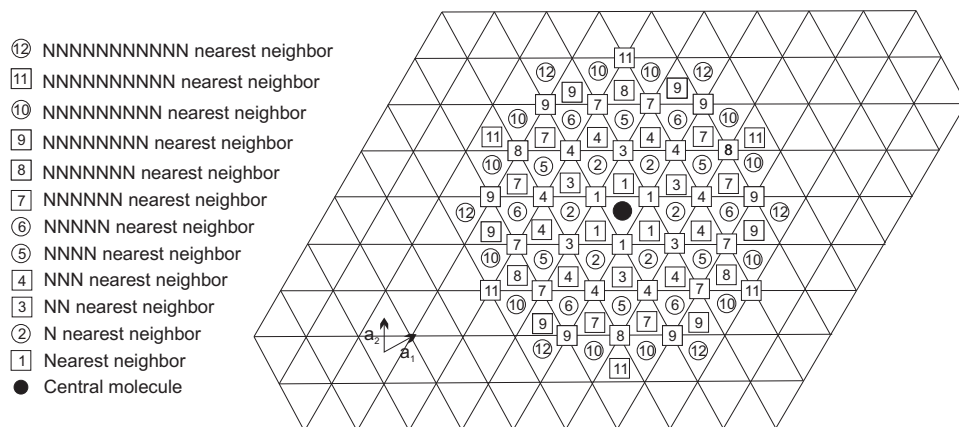
3.3.1 Simulations

In this study, the derivation of the kinetic parameters as described in section 3.2.1 and the construction of the zero temperature phase diagram is the work of C. Popa and A. P. J. Jansen [33].

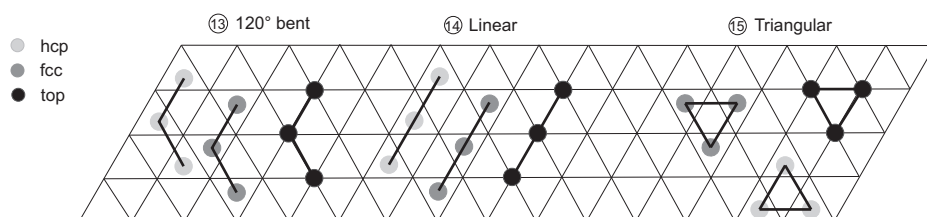
Kinetic parameters

Some of the interactions that are taken into account in the second sum of equation (3.2.1), are shown in Fig. 3.2. Fig. 3.2(a) shows the pair interactions. The interactions are numbered according to the distance from the central molecule over which they act and can be divided into heterogeneous and homogeneous interactions. The latter act between molecules adsorbed at the same type of adsorption sites (hcp-hcp, fcc-fcc or top-top) and are indicated by a circle. A box is drawn when it concerns a heterogeneous interaction between different type of adsorption sites (hcp-fcc, hcp-top or fcc-top). The central molecule can have one or more of each of the numbered interactions.

In Fig. 3.2(b) the homogeneous three particle interactions are shown. Interactions ⑬, ⑭ and ⑮ have their adsorbates arranged under a 120° angle, linearly and in a triangle, respectively. The heterogeneous three particle interactions and homogeneous



(a)



(b)

Figure 3.2: (a) Pair interactions taken into account in the Bayesian calculation for the lateral interactions. The Rh(111) lattice is depicted similarly as in Fig. 3.1. The interactions are numbered according to the distance over which they act. In this picture, the central molecule is depicted at the fcc site. Interactions for the hcp bound molecule are obtained by shifting the central molecule and all its neighbors up by a_2 . For a top adsorbed molecule, they should be shifted along a_1 . The interactions can be divided into two groups. Heterogeneous interactions act between molecules at different adsorption sites and are recognized by a box that is drawn around the number of the interaction. Interactions between molecules adsorbed at the same type of site are called homogeneous and are indicated by a circle. Heterogeneous interactions have 3-fold symmetry whereas homogeneous interactions are 6-fold symmetric. (b) The homogeneous three-particle interactions. The numerical values of these interactions are listed in Table 3.2.

3. Determination of adsorbate lateral interactions

four particle interactions that were also taken into account are not shown here as they had a negligible probability of existence.

The results of the Bayesian fit for the adsorption energy for the different adsorption sites are listed in Table 3.1 ². An isolated NO molecule binds strongest to the hollow sites with the hcp site being favored over the fcc site by only 3%. The binding strength on top of a rhodium surface atom is 75% of the strength when the molecule is adsorbed at the hollow sites.

The values of the interactions that were found to be reliable (alternatively, in Bayesian terms, the interactions that have a large probability of existence) are shown in Table 3.2. Positive values denote repulsive interactions, negative values attractive. The shaded area in the table helps to make the distinction between the homogeneous and heterogeneous interactions. Interaction $\boxed{1}$ could not be determined because, in the DFT calculation, structures with NO molecules located this close together were unstable. Therefore, for this interaction, a value close to the desorption energy of a hollow site is chosen. This ensures desorption of a molecule when it is experiencing interaction $\boxed{1}$ but is impeded to diffuse away due to other neighboring molecules. The total number of kinetic parameters (i.e. the adsorption energies and the pairwise, three and four particle interactions) to take into account in the kMC simulations is only 16 out of a possible 93. Furthermore, only the short range pair interactions $\textcircled{2}$ and $\textcircled{3}$ seem to be important. As the hcp site has the lowest binding energy, this site becomes occupied first at low coverage. It is therefore reasonable also to expect the longer range pair interactions $\textcircled{5}$ and $\textcircled{6}$ to exist for the hcp site only. Finally, next to the pair interactions, the homogeneous linear three particle interactions $\textcircled{14}$ for the hcp and fcc sites appear to be important, but all other three and four particle interactions do not play a role.

Table 3.1: Numerical result of the Bayesian calculation for the adsorption energies of the three different adsorption sites in kJ/mol [33].

	hcp	fcc	top
E_{ads}^0	-253 ± 1	-246 ± 1	-190 ± 1

²Note that 1 eV=96.5 kJ/mol.

Table 3.2: The numerical results of the Bayesian calculation for the lateral interactions indicated in Fig. 3.2. The gray shaded areas help the eye to distinguish between homogeneous and heterogeneous interactions. Interactions that do not appear in the list, had a low probability of existence.

		Interaction Energy (kJ/mol)					
Interaction		$E_{\text{hcp-hcp}}$	$E_{\text{fcc-fcc}}$	$E_{\text{top-top}}$	$E_{\text{hcp-fcc}}$	$E_{\text{hcp-top}}$	$E_{\text{fcc-top}}$
pair interaction	①				250	250	250
	②	14 ± 2	18 ± 2	19 ± 1			
	③				4 ± 1	6 ± 2	6 ± 2
	④				-	-	-
	⑤	2 ± 1	-	-			
	⑥	3 ± 1	-	-			
3 particle interaction	⑬	-	-	-			
	⑭	9 ± 2	8 ± 2	-			
	⑮	-	-	-			

Zero temperature phase diagram

Fig. 3.3 shows the phase diagram of NO on Rh(111) at $T=0$ K as a function of coverage. Each (black) cross in the graph represents the DFT calculated adsorption energy per NO molecule of a structure. In total, 73 structures with different coverages have been calculated. The (red) plus symbols indicate the adsorption energy calculated according to equation (3.2.1) using the fitted kinetic parameters of Table 3.1 and Table 3.2. The (black) full line connects the DFT calculated data points that have the lowest energy of adsorption with the lowest possible slope. The (red) dashed line similarly connects the fitted data points. Although deviating, the points connected by both lines represent the same structures. In the coverage range 0.50-0.80 ML, each point with the lowest adsorption energy is labeled according to the name of the structure it belongs to. The configuration for each of these structures is shown in Fig. 3.1 and Fig. 3.4.

The zero temperature phase diagram of Fig. 3.3 shows what structure is en-

3. Determination of adsorbate lateral interactions

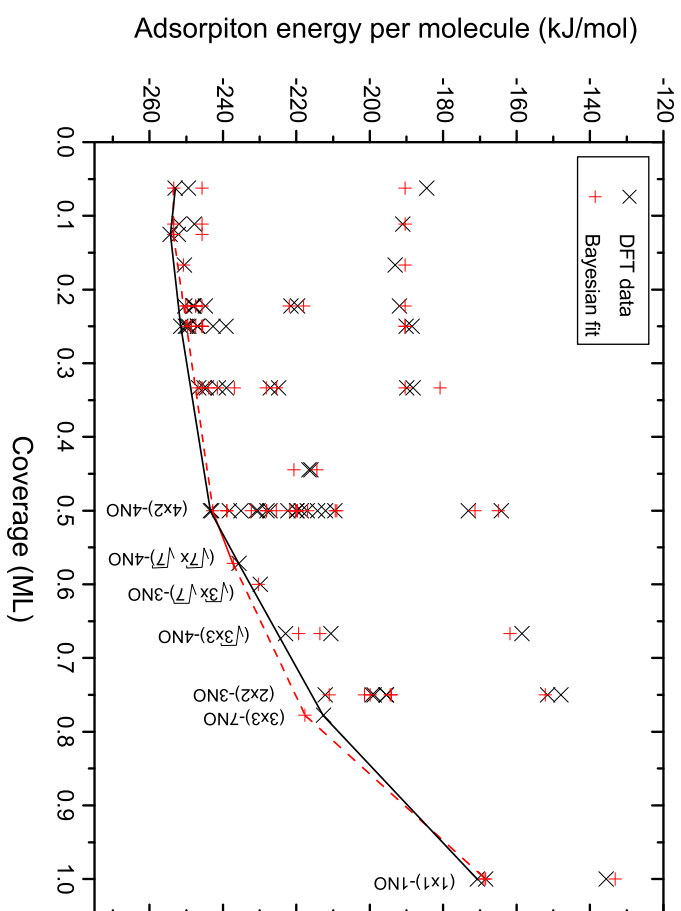


Figure 3.3: Graph showing the zero temperature phase diagram [33]. Each of the 73 (black) crosses represents the DFT calculated adsorption energy per molecule for a structure of a certain coverage. The (red) plus symbols denote the adsorption energy calculated from the fitted kinetic parameters (equation (3.2.1)). The full and dashed lines connect data points of the structures with minimum energy for the DFT calculated and fitted values, respectively.

ergetically most favorable. For example, at 0.50 ML coverage, this will be the $(4 \times 2) - 4\text{NO}$ structure, at 0.57 ML the $(\sqrt{7} \times \sqrt{7}) - 4\text{NO}$ structure and at 0.78 ML the $(3 \times 3) - 7\text{NO}$ configuration. An adlayer with a coverage on the line drawn between two data points will consist of patches of the two structures belonging to these data points. The area occupied by each patch is inversely proportional to the distance to the data point to which the structure corresponds.

As is explained by equation (3.1.1), at finite temperatures, the phase diagram might start to deviate from Fig. 3.3. In order to include the entropy, kMC simulations are performed. Note that when structures in kMC were found that have not been included in the derivation of the lateral interactions, the interactions had to be determined again including the omitted structure. This procedure is repeated until all configurations found in kMC have been used for deriving the lateral interactions³.

Kinetic Monte Carlo Simulations

The results of the kMC simulation performed at 200 K using the kinetic parameters of Table 3.1 and Table 3.2 are shown in Fig. 3.5 to Fig. 3.8 for increasing coverage of the surface. Increasing coverage is achieved by increasing the adsorption rate of the molecules on the surface. However, in order to stay in equilibrium, the diffusion rate constant has to be increased simultaneously.

Just as in Fig. 3.1, the brightest dots in the images denote the hcp bound molecules, the dark gray dots the fcc molecules and the black dots the top bound molecules. At an overall coverage of around 0.40 ML, the first ordered patches start to form. In Fig. 3.5, it is shown that these patches consist of the 0.50 ML $(4 \times 2) - 4\text{NO}$ structure (see Fig. 3.1). The zigzag lines in the picture help to see the orientation of the different domains. Indeed, based on the zero temperature phase diagram of Fig. 3.3, this structure would have been expected to form at 0.50 ML coverage. Moreover, this structure was repeatedly reported in literature [21, 22, 23].

When increasing the coverage, the $(4 \times 2) - 4\text{NO}$ structure transforms into another zigzag-like structure, as depicted in Fig. 3.6. This previously unreported $(\sqrt{3} \times \sqrt{7}) - 3\text{NO}$ structure with a coverage of 0.60 ML is shown schematically in

³In fact, this is how the $(\sqrt{7} \times \sqrt{7}) - 4\text{NO}$, the $(\sqrt{3} \times \sqrt{7}) - 3\text{NO}$ and the $(\sqrt{3} \times 3) - 4\text{NO}$ structures were found.

3. Determination of adsorbate lateral interactions

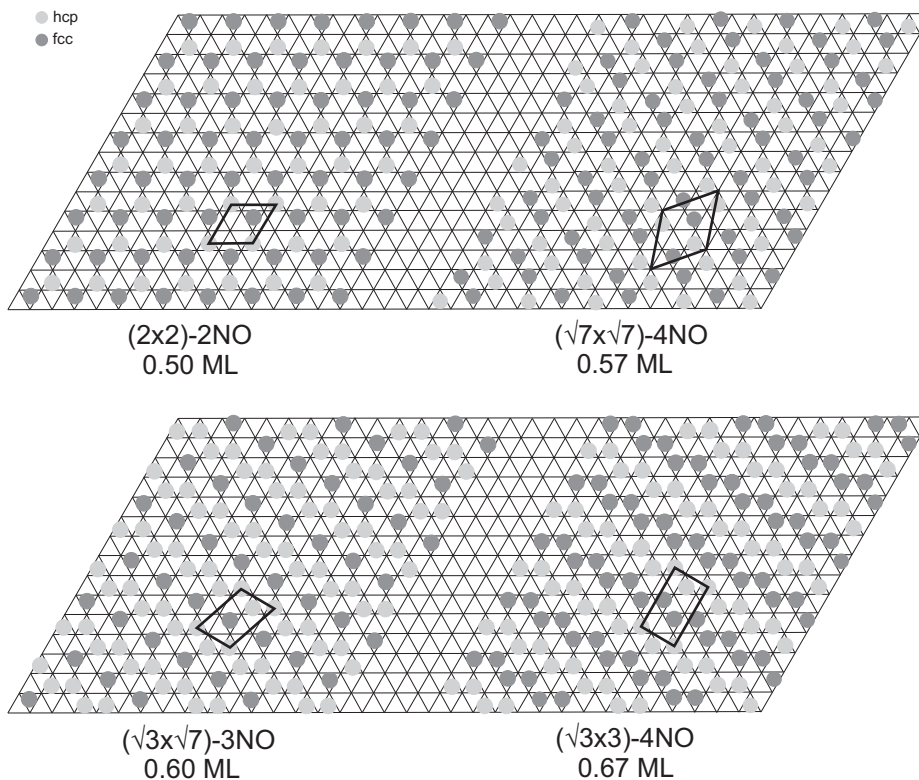


Figure 3.4: Top view of ordered structures of NO on Rh(111) obtained in this study. The representation of the structures is similar to Fig. 3.1.

Fig. 3.4. Whereas the adsorption site of the molecules along the zigzag line of the $(4 \times 2) - 4\text{NO}$ structure alternates between fcc and hcp, here, the zigzag patterns are made up of hcp adsorbed molecules only. In between these wiggly lines, straight lines of wider spaced fcc molecules are formed. In order to guide the eye, the hcp zigzag lines are highlighted in parts of the adlayer of Fig. 3.6. The transition from the $(4 \times 2) - 4\text{NO}$ structure to the $(\sqrt{3} \times \sqrt{7}) - 3\text{NO}$ structure is rather fast since it can start from within the $(4 \times 2) - 4\text{NO}$ domains themselves, i.e. the molecules only have to move closer together without having to reassemble completely. According to Fig. 3.3, at $T=0$ K, the $(\sqrt{7} \times \sqrt{7}) - 4\text{NO}$ structure would be preferred to form above the $(\sqrt{3} \times \sqrt{7}) - 3\text{NO}$ structure, which is located slightly above the minimum energy

3.3 Results and discussion

line. This discrepancy can be explained by the entropy of the $(\sqrt{3} \times \sqrt{7}) - 3\text{NO}$ being larger than the entropy of the $(\sqrt{7} \times \sqrt{7}) - 4\text{NO}$ adlayer, as was explained in equation (3.1.1).

Increasing the coverage even further, the density along the line formed by the fcc molecules is doubled by transforming from a straight line into a zigzag line, see Fig. 3.7. In parts of the picture, the zigzag pattern is indicated by zigzag lines. The schematic diagram of this unreported $(\sqrt{3} \times 3) - 4\text{NO}$ structure with a coverage of 0.67 ML is depicted in Fig. 3.4. Similar to the transition from the $(4 \times 2) - 4\text{NO}$ structure to the $(\sqrt{3} \times \sqrt{7}) - 3\text{NO}$ structure, the transformation from the $(\sqrt{3} \times \sqrt{7}) - 3\text{NO}$ to the $(\sqrt{3} \times 3) - 4\text{NO}$ structure can happen within the $(\sqrt{3} \times \sqrt{7}) - 3\text{NO}$ patch itself: the lines only need to move closer together. In fact, in Fig. 3.6, some areas of the $(\sqrt{3} \times 3) - 4\text{NO}$ structure can already be discerned. Just as the $(\sqrt{3} \times \sqrt{7}) - 3\text{NO}$, the $(\sqrt{3} \times 3) - 4\text{NO}$ structure is located slightly above the line of minimal energy in Fig. 3.3 but can be accounted for by the entropy.

Finally, the adlayer forming after the $(\sqrt{3} \times 3) - 4\text{NO}$ structure is the $(3 \times 3) - 7\text{NO}$ structure with a density of 0.78 ML, see Fig. 3.8 and Fig. 3.1. This structure was reported experimentally at room temperature in the torr pressure range [24]. In some areas of Fig. 3.8, the $(3 \times 3) - 7\text{NO}$ structure is indicated by lines connecting the top molecules and triangles illustrating the triangular arrangement of the fcc and hcp molecules. As opposed to the previously discussed transitions, this transformation is slow as the molecules have to rearrange completely. Therefore this structure can only start growing from the boundaries between the different patches of the $(\sqrt{3} \times 3) - 4\text{NO}$ structure. In some parts of Fig. 3.8 some small grains of a 0.81 ML $(4 \times 4) - 13\text{NO}$ structure can be seen. This structure has a similar molecular arrangement as the $(3 \times 3) - 7\text{NO}$ structure. The top atom sits at the corner of the unit cell with two triangular groups of six molecules adsorbed at the fcc and hcp sites each. In the picture of Fig. 3.8, the $(4 \times 4) - 13\text{NO}$ structure is indicated by thick lines in a similar way as for the $(3 \times 3) - 7\text{NO}$ configuration.

In Table 3.3 it is shown how much time it takes for a certain structure to form in the kMC simulations of Fig. 3.5 to Fig. 3.8. In order to make a proper comparison, all simulation times are scaled from the values indicated in the caption of each figure to

3. Determination of adsorbate lateral interactions

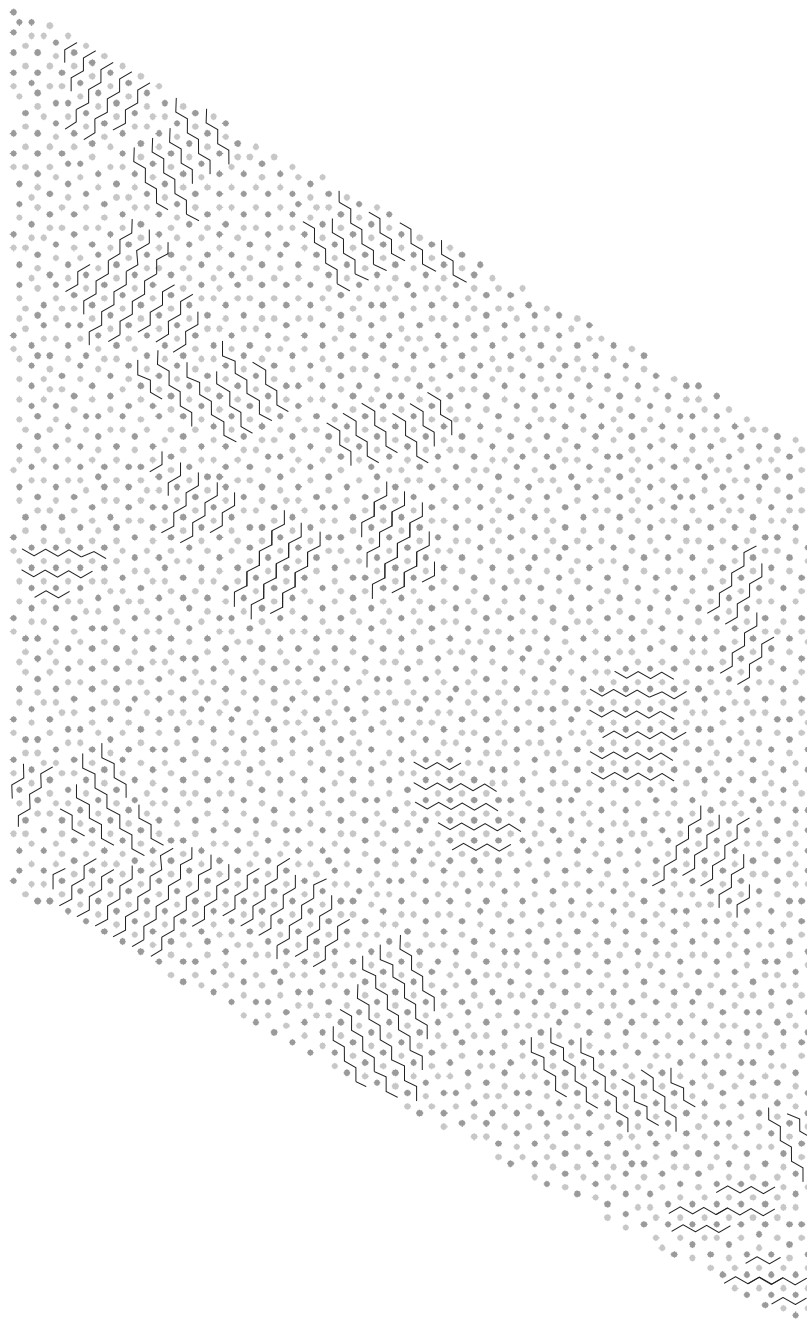


Figure 3.5: Adsorbate distribution from the kMC simulation ($\theta = 0.54$ ML) showing patches of the $(4 \times 2) - 4\text{NO}$ structure of different orientation. The zigzag lines are drawn to guide the eye. Each side of the parallelogram is 20.5 nm. Simulation parameters are: $T = 200$ K, $E_{diff} = 47$ kJ/mol, $\nu_{diff} = 1 \cdot 10^{13}$ s $^{-1}$, $E_{des} = -E_{ads}$, $\nu_{des} = 3 \cdot 10^{13}$ s $^{-1}$ and an adsorption rate of 0.01 which equals a pressure of 10^{-8} mbar.

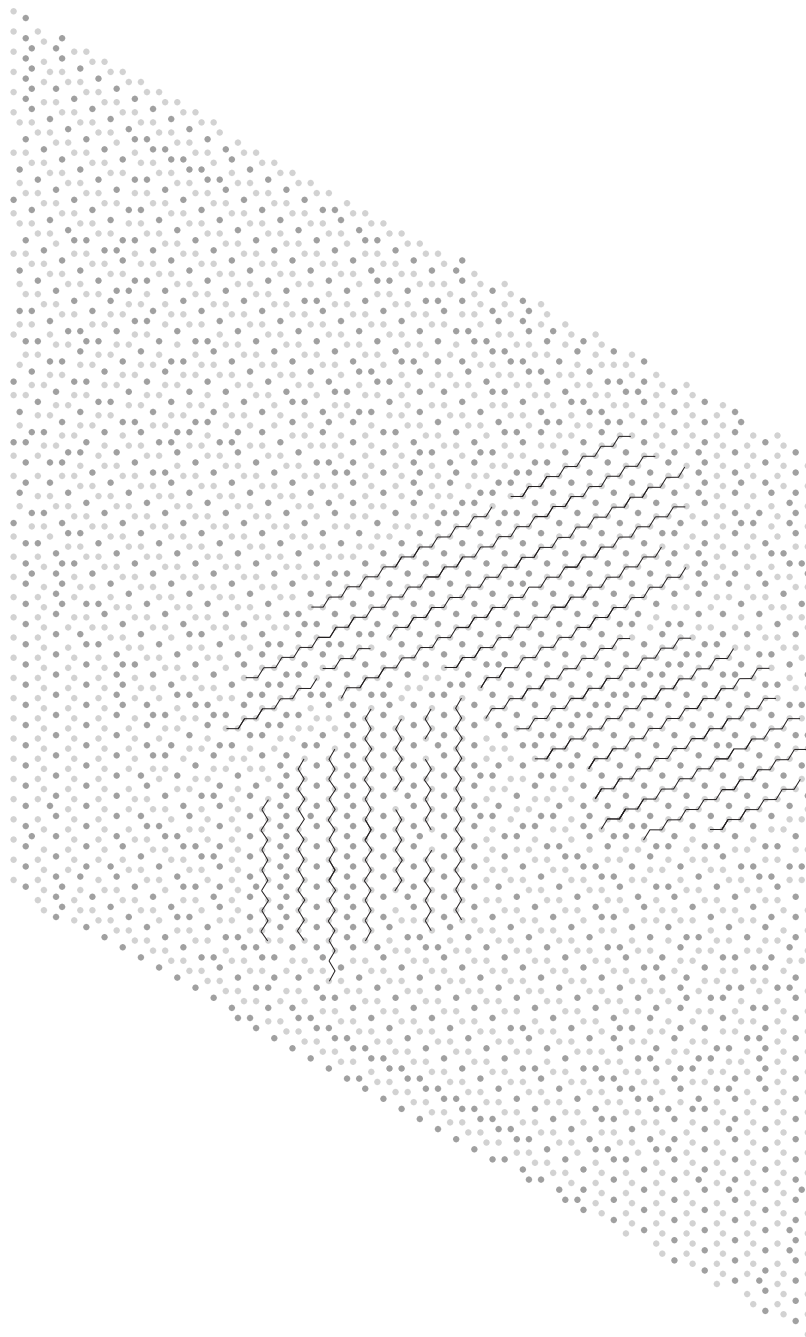


Figure 3.6: Adsorbate distribution from the kMC simulation ($\theta = 0.61$ ML). The dominant structure is the $(\sqrt{3} \times \sqrt{7}) - 3\text{NO}$ with small areas of the $(\sqrt{3} \times 3) - 4\text{NO}$ structure. The zigzag lines are drawn to guide the eye. Each side of the parallelogram is 20.5 nm. Simulation parameters are: $T = 200$ K, $E_{diff} = 47$ kJ/mol, $\nu_{diff} = 1 \cdot 10^{14} \text{ s}^{-1}$, $E_{des} = -E_{ads}$, $\nu_{des} = 3 \cdot 10^{13} \text{ s}^{-1}$ and an adsorption rate of 1 which equals a pressure of 10^{-6} mbar.

3. Determination of adsorbate lateral interactions

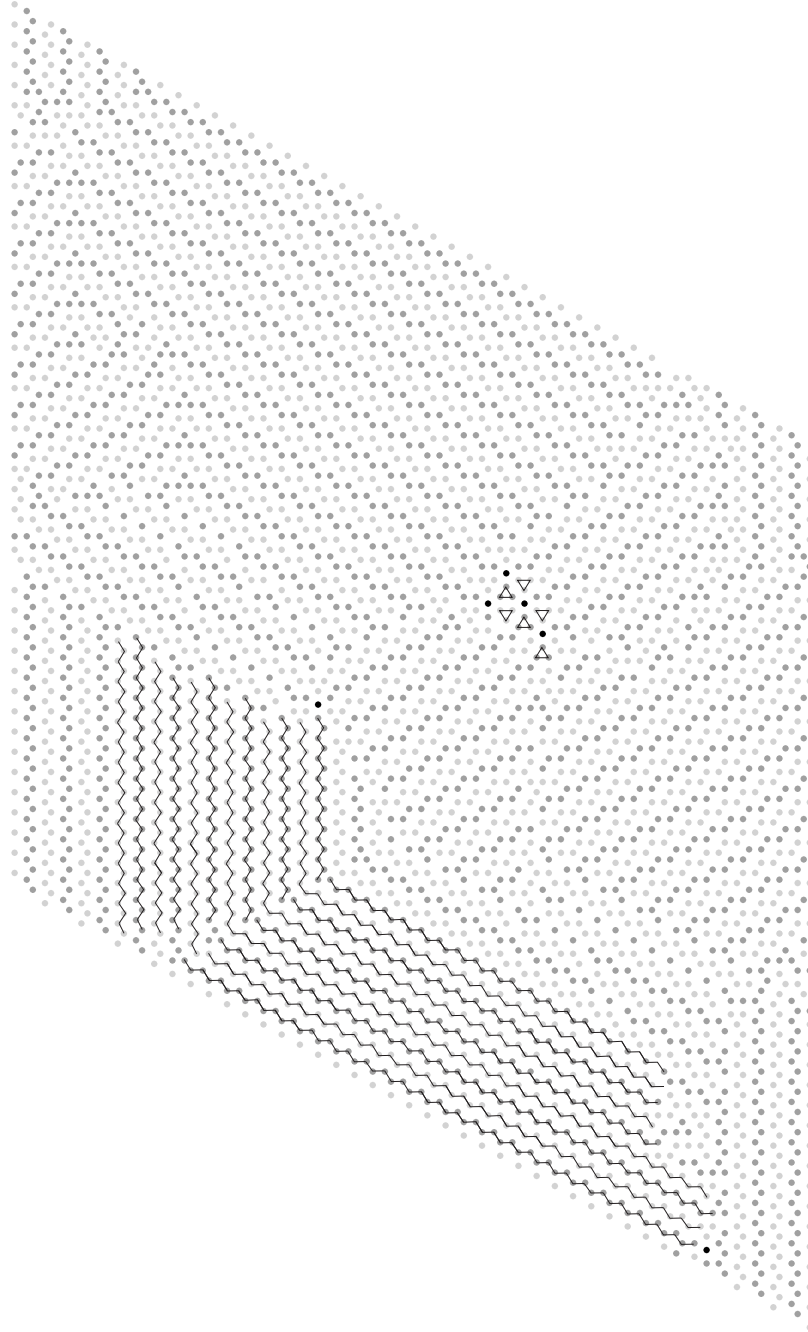


Figure 3.7: Adsorbate distribution from the kMC simulation ($\theta = 0.67$ ML) showing the $(\sqrt{3} \times 3) - 4\text{NO}$ structure. The zigzag lines guide the eye. Each side of the parallelogram is 20.5 nm. In the middle of the picture, at the boundary between two grains, a seed of the $(3 \times 3) - 7\text{NO}$ is already visible as indicated by the triangles. Simulation parameters are: $T = 200$ K, $E_{diff} = 47$ kJ/mol, $\nu_{diff} = 1 \cdot 10^{14} \text{ s}^{-1}$, $E_{des} = -E_{ads}$, $\nu_{des} = 3 \cdot 10^{13} \text{ s}^{-1}$ and an adsorption rate of 1 which equals a pressure of 10^{-6} mbar.

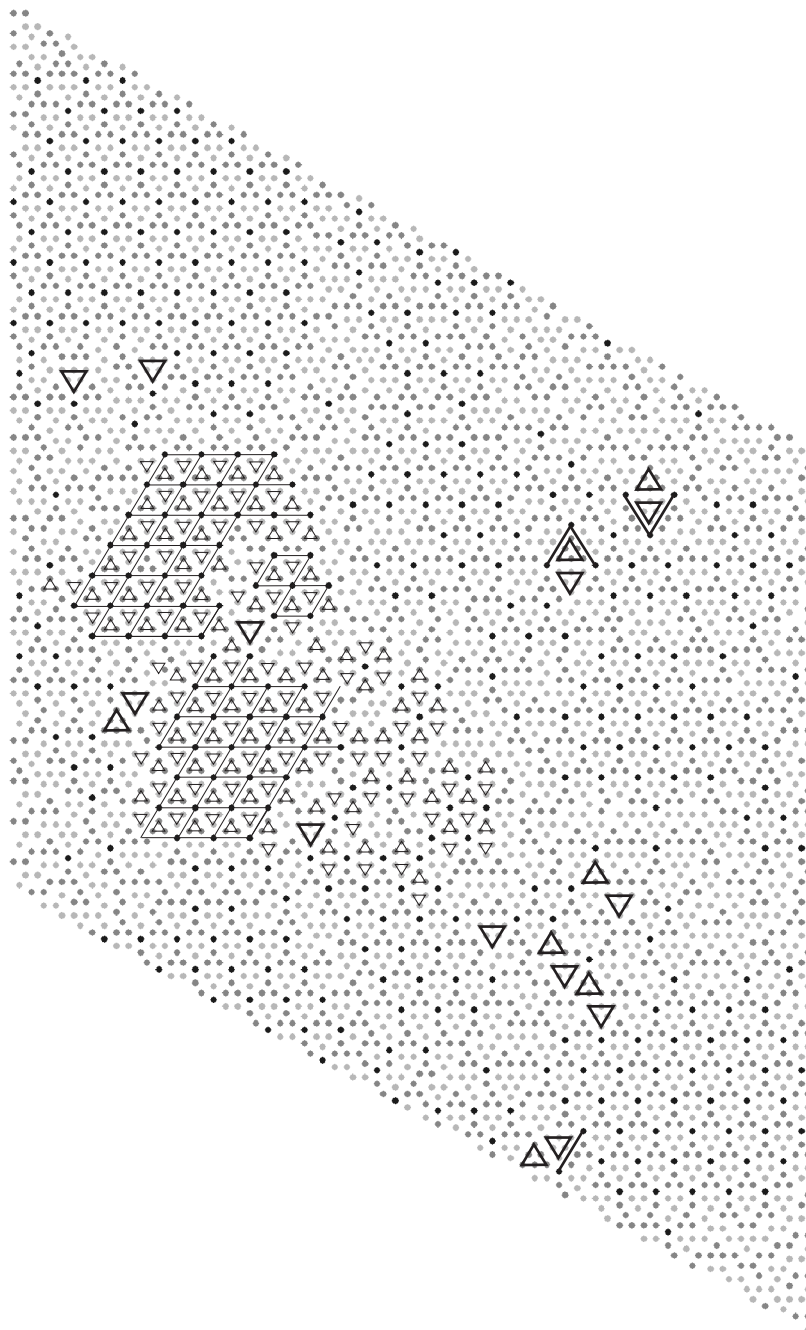


Figure 3.8: Adsorbate distribution from the kMC simulation ($\theta = 0.76$ ML) showing patches of the $(3 \times 3) - 7\text{NO}$ structure. The configuration is indicated by the lines connecting the top molecules and triangles highlighting the groups of fcc and hcp molecules. The large triangles highlight groups consisting of six fcc and hcp molecules. Each side of the parallelogram is 20.5 nm. Simulation parameters are: $T = 200$ K, $E_{diff} = 47$ kJ/mol, $\nu_{diff} = 1 \cdot 10^{16} \text{ s}^{-1}$, $E_{des} = -E_{ads}$, $\nu_{des} = 3 \cdot 10^{13} \text{ s}^{-1}$ and an adsorption rate of 100000 which equals a pressure of 10^{-1} mbar.

3. Determination of adsorbate lateral interactions

Table 3.3: The kMC time it takes to form the structures of Fig. 3.5 to Fig. 3.8. The times are scaled to $\nu_{diff}=10^{13} \text{ s}^{-1}$ and $k_{ads}=1 \text{ s}^{-1}$ to make them comparable. The transition factor in the last column is the ratio of the time of formation between the structure before and after the transition.

structure	scaled kMC time	transition factor
$(4 \times 2) - 4\text{NO}$	2.5 s	\Downarrow 15 \times
$(\sqrt{3} \times \sqrt{7}) - 3\text{NO}$	37.5 s	\Downarrow 13 \times
$(\sqrt{3} \times 3) - 4\text{NO}$	8.3 min	\Downarrow 195 \times
$(3 \times 3) - 7\text{NO}$	27 h	

$\nu_{diff}=10^{13} \text{ s}^{-1}$ and $k_{ads}=1 \text{ s}^{-1}$. In the last column, the transition factor indicates how much time it takes for a structure to form during a phase transition between two structures. It is expressed in multiples of the formation time of the phase before the phase transition took place. Indeed, the transitions described above as fast have a transition factor of about 15 whereas for the slow transition from the $(\sqrt{3} \times 3) - 4\text{NO}$ to the $(3 \times 3) - 7\text{NO}$ structure it is 195.

It is interesting to note that in [37], the saturation coverage of NO on Rh(111) at $T = 120 \text{ K}$ and $p = 10^{-7} \text{ mbar}$ was determined to be 0.68 ML. The configuration of this adlayer, however, could not be derived. At 120 K, diffusion is slow and it might therefore be expected that only the easy transformations can occur within a reasonable amount of time. The configuration with the highest possible structure that can be obtained this way is the $(\sqrt{3} \times 3) - 4\text{NO}$ structure with a coverage of 0.67 ML, in accordance to the experimentally determined value.

Our kMC simulations can be compared directly to a similar theoretical study on the same system, in which only pairwise interactions up to the next-next nearest neighbor (interaction $\boxed{3}$ see Fig. 3.2(a)) were taken into account [10]. There, at 0.50 ML coverage, the formation of either the $(4 \times 2) - 4\text{NO}$ or the $(2 \times 2) - 2\text{NO}$ structure, that is depicted in Fig. 3.4, strongly depended on the value of the next-next nearest neighbor. Due to the error margin of the calculation this value could not be determined. The $(2 \times 2) - 2\text{NO}$ structure on average has 1.5 next-next nearest neighbors per adsorbate, whereas the $(4 \times 2) - 4\text{NO}$ structure has only 1. Large

repulsive interactions of 5 kJ/mol therefore resulted in the $(4 \times 2) - 4\text{NO}$ structure. For interactions of the order of the simulation temperature of 200 K (2 kJ/mol), however, islands of both structures were observed. A structure with high density was then easily formed by filling the honeycombs of the $(2 \times 2) - 2\text{NO}$ structure with top bound NO molecules, resulting in the 0.75 ML $(2 \times 2) - 3\text{NO}$ structure (Fig. 3.1). However, our study reveals that interaction $\boxed{3}$ is 4 kJ/mol, too large for the $(2 \times 2) - 2\text{NO}$ structure to be formed and although the $(2 \times 2) - 3\text{NO}$ structure was also reported in literature [21, 22, 23], it was not obtained in our kMC simulations. Possible reasons for this deviation will be discussed in the next section.

3.3.2 Experiment

Before performing the STM experiments, the Rh(111) sample was cleaned and exposed to the NO gas at 200 K as is described in section 2.3.1. At low dosage, the surface is partly covered by patches of the $(4 \times 2) - 4\text{NO}$ structure as is shown in Fig. 3.9. On the Rh(111) surface, there are three possible orientations of the $(4 \times 2) - 4\text{NO}$ domains, all of which are present in the image as elucidated by the white zigzag lines. The inset is a zoom on a patch in which the individual molecules are resolved. In between the patches, single molecules are found. Comparing Fig. 3.9 to the simulated adlayer of Fig. 3.5, both images show patches of the $(4 \times 2) - 4\text{NO}$ structure of different orientation. Moreover, this structure is in accordance with the experimentally found structure at 0.50 ML [21, 22, 23]. In the kMC image the formation of $(4 \times 2) - 4\text{NO}$ patches started at a total coverage of about 0.40 ML. This can be understood by realizing that all lateral interactions are repulsive (Table 3.2). Therefore, the molecules would like to stay as far apart as possible. Only when approaching 0.50 ML coverage, the optimal solution is the formation of the $(4 \times 2) - 4\text{NO}$ structure. However, this is not what is observed in the experimental image of Fig. 3.9. Here, the coverage is estimated to be 0.30 ML but islands of the $(4 \times 2) - 4\text{NO}$ structure are already formed despite the fact that there is still space for the molecules to spread out further in between the patches. This difference might be explained by the presence of subsurface impurities that are known to serve as nucleation centers for CO on Pd(111) [38]. The subsurface density of our sample is estimated to be less

3. Determination of adsorbate lateral interactions

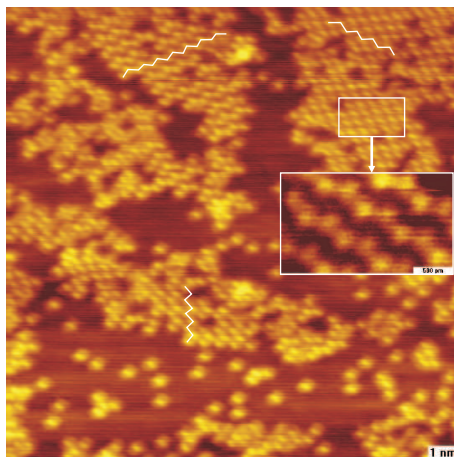


Figure 3.9: STM image ($15 \times 15 \text{ nm}^2$) taken at 77 K of the low coverage phase of NO on Rh(111) deposited at 200 K. About 50% of the surface is covered by single molecules. The other half is ordered in the $(4 \times 2) - 4\text{NO}$ structure. White zigzag lines are drawn to guide the eye. Inset: $2 \times 1.5 \text{ nm}^2$ zoom on the $(4 \times 2) - 4\text{NO}$ structure showing individual molecules ($V = 109 \text{ mV}$, $I = 416 \text{ pA}$).

then 2% (section 2.3.2), so that the $15 \times 15 \text{ nm}^2$ image in Fig. 3.9 is expected to have less than 50 nucleation sites, which is in accordance to the observation. Yet, the fact that these impurities cause premature nucleation of domains does not seem to affect the type of structure that is formed.

Upon higher dose, the structure of Fig. 3.10(a) is obtained. The image is a $50 \times 50 \text{ nm}^2$ overview showing lines running all over the sample surface in three different directions. Fig. 3.10(b) is a $15 \times 15 \text{ nm}^2$ zoom on picture (a) emphasizing the linear structure. Three to seven lines run in parallel to each other and in between these lines, features can be discerned that are not imaged as bright as the lines. In the inset, the individual molecules are resolved and white circles are drawn to highlight their position. The structure consists of bright zigzagging lines alternated by straight lines in which the molecules are imaged less bright. This adlayer is therefore identified as the $(\sqrt{3} \times \sqrt{7}) - 3\text{NO}$ structure (Fig. 3.4). The resemblance between Fig. 3.10(b) and Fig. 3.6 is strikingly high.

In Fig. 3.10(c), the resulting image is depicted after an even higher dosage of NO to the Rh(111). It shows two different adlayer configurations, separated from each

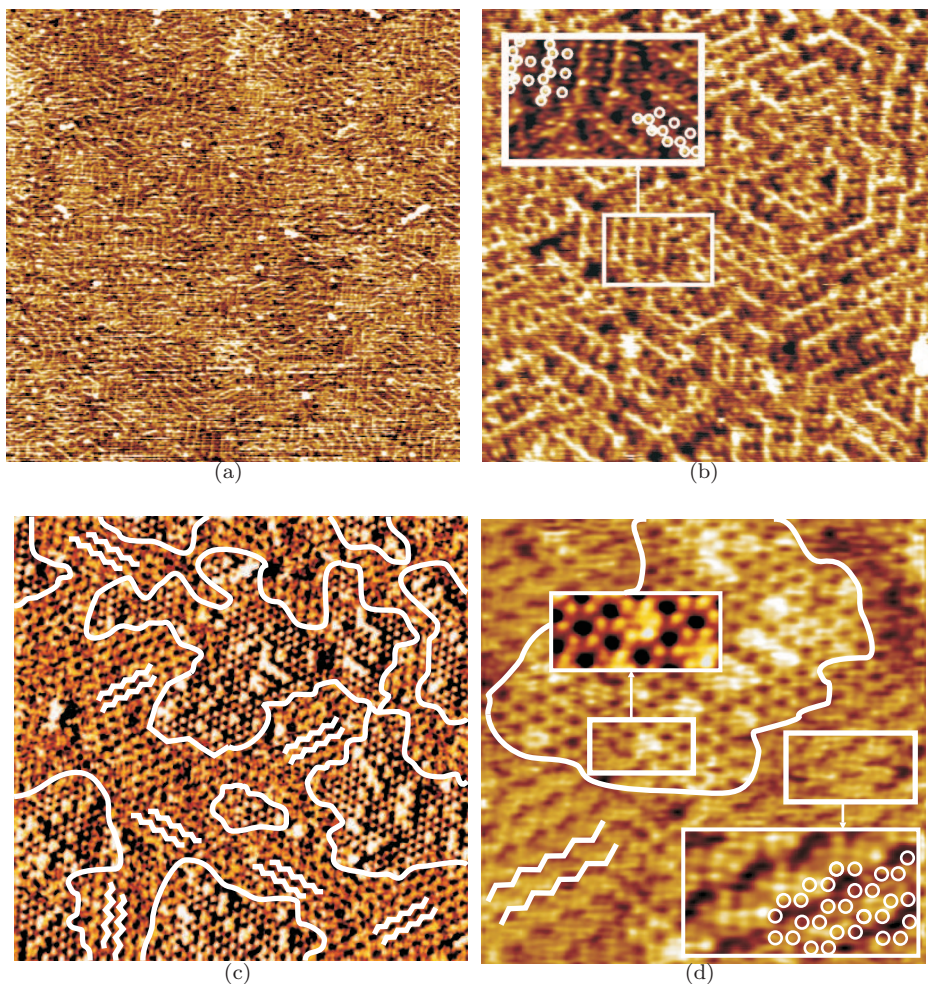


Figure 3.10: (a) $50 \times 50 \text{ nm}^2$ STM image taken at 200 K showing the linear nature of the adlayer. (b) $15 \times 15 \text{ nm}^2$ zoom on the structure of (a), inset: $6 \times 4 \text{ nm}^2$ zoom resolving the individual molecules of the $(\sqrt{3} \times \sqrt{7}) - 3\text{NO}$ structure the positions of which are indicated by the white circles. (c) $30 \times 30 \text{ nm}^2$ image showing two types of structures on the surface. White full lines help to see the boundaries between the different configurations. The wiggly white lines indicate the orientation of the different patches of the zigzag-like structure. (d) $15 \times 15 \text{ nm}^2$ zoom on (c). Left inset: $2.8 \times 1 \text{ nm}^2$ zoom on the $(2 \times 2) - 2\text{NO}$ structure showing individual molecules. The middle honeycomb is filled by an NO molecule adsorbed on the top site. Lower right inset ($4 \times 2 \text{ nm}^2$): Although the individual molecules of the zigzag structure are not well resolved, the positions of the molecules of the $(\sqrt{3} \times 3) - 4\text{NO}$ structure, to which this configuration is tentatively assigned, are superimposed as white circles. Measurement parameters for all images: $V = -99 \text{ mV}$, $I = 440 \text{ pA}$.

3. Determination of adsorbate lateral interactions

other by white lines to guide the eye. One of the structures again shows a zigzag-like pattern. The different orientations of this structure are indicated by the white zigzag lines. The other structure has a hexagonal symmetry and about one fifth of the pattern is covered by bright dots. Fig. 3.10(d) is a zoom on Fig. 3.10(c). The inset in the lower right corner is a zoom on the zigzag structure. Although it is hard to identify the individual molecules in the image, projecting the positions of the molecules of the $(\sqrt{3} \times 3) - 4\text{NO}$ structure (see Fig. 3.4) over it gives a reasonable match. Therefore, this structure is tentatively assigned to the $(\sqrt{3} \times 3) - 4\text{NO}$ structure. Comparing Fig. 3.10(c) to Fig. 3.7, both pictures show patches in which several zigzag lines run parallel to each other. The hexagonal structure could be resolved with molecular resolution as is shown in the left inset of Fig. 3.10(d). The molecules are arranged in a honeycomb structure, similar to the $(2 \times 2) - 2\text{NO}$ structure of Fig. 3.4. The blurry bright spots in the patch arise from top bound NO molecules at the center of the honeycombs. This means that the structure is actually a mixture between the 0.50 ML $(2 \times 2) - 2\text{NO}$ and 0.75 ML $(2 \times 2) - 3\text{NO}$ configurations (compare Fig. 3.1 and Fig. 3.4).

Fig. 3.11 shows the diffusion at 200 K of the top bound NO molecules in the $(2 \times 2) - 2\text{NO}$ structure over time. Isolated top molecules make multiple hops from one honeycomb to another within minutes. Apparently, the physical barrier formed by the two NO molecules at the fcc and hcp site do not prevent the molecule from diffusing. From this figure, we can estimate the activation barrier for this type of diffusion by rewriting equation (3.2.4):

$$E_{act} = -k_b T \ln \frac{k_{diff}}{\nu}.$$

From Fig. 3.11, the rate constant for top diffusion of an isolated top bound NO molecule can be estimated to be of the order of $k_{diff} \sim 0.01 \text{ s}^{-1}$. A typical value for the prefactor ν is $\sim 10^{13} \text{ s}^{-1}$ and with $T = 200 \text{ K}$ this amounts to $E_{act} = 70 \text{ kJ/mol}$. The error of this calculation depends on the uncertainty of the determination of k_{diff} and ν . However, as E_{act} depends only logarithmically on the ratio $\frac{k_{diff}}{\nu}$, even if our estimate is off by 2 orders of magnitude, the error in the activation barrier is still only 13%.

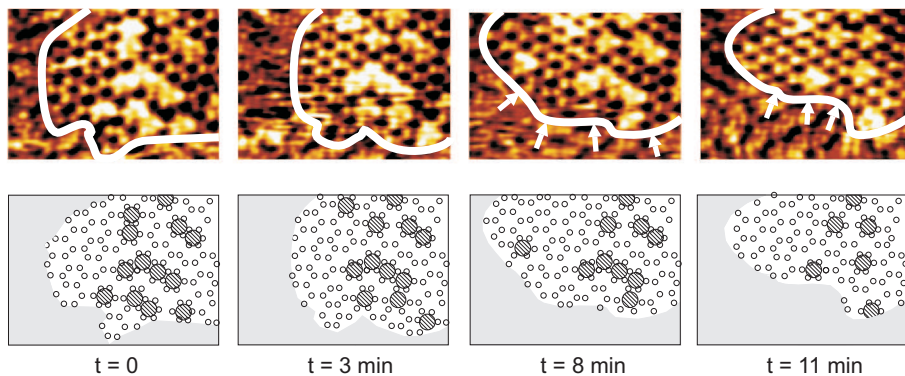


Figure 3.11: Sequence of $4 \times 3 \text{ nm}^2$ STM images taken at 200 K ($V=99 \text{ mV}$, $I=440 \text{ pA}$) to illustrate the diffusion of the top adsorbed NO molecules over the $(2 \times 2) - 2\text{NO}$ structure. The white lines mark the boundary between the $(2 \times 2) - 2\text{NO}$ and $(\sqrt{3} \times 3) - 4\text{NO}$ configurations. The movement of this boundary over time is indicated by the white arrows. For clarity, the bottom row is a schematic representation of the STM images. The open circles stand for the NO molecules in the $(2 \times 2) - 2\text{NO}$ structure. The larger dashed circles depict the top bound molecules and the grey area is the area of the $(\sqrt{3} \times 3) - 4\text{NO}$ structure.

It is remarkable that the dilute 0.50 ML $(2 \times 2) - 2\text{NO}$ structure forms at high exposures of the substrate to the NO gas. After all, as is shown in Fig. 3.5 and Fig. 3.9, at 0.50 ML coverage, it is the $(4 \times 2) - 4\text{NO}$ structure that prevails. Taking into account the higher density of the coexisting $(\sqrt{3} \times 3) - 4\text{NO}$ structure, the appearance of the $(2 \times 2) - 2\text{NO}$ patches cannot be explained as a transition structure in the transformation from the $(\sqrt{3} \times 3) - 4\text{NO}$ structure to the denser 0.75 ML $(2 \times 2) - 3\text{NO}$ adlayer. Even when accounting for the fact that about one fifth of the honeycombs in Fig. 3.10(d) is filled, this still amounts to a coverage of only 0.55 ML. Taking a closer look at Fig. 3.11, however, the patch of the $(2 \times 2) - 2\text{NO}$ structure is decreasing in size over time, as is illustrated by the arrows in the consecutive images. This means that the system is undergoing a phase transition. Probably, the exposure of the substrate to a relatively high NO gas pressure resulted in patches of the 0.67 ML $(\sqrt{3} \times 3) - 4\text{NO}$ and the 0.75 ML $(2 \times 2) - 3\text{NO}$ structures. However, when the NO gas was removed from the chamber prior to starting the experiment, the system had to reach a new equilibrium. The molecules adsorbed at the top sites of the $(2 \times 2) - 3\text{NO}$ structure have the weakest bond to the substrate and will there-

3. Determination of adsorbate lateral interactions

fore desorb first, leaving the patch behind in the $(2 \times 2) - 2\text{NO}$ configuration. Being unstable, this configuration slowly transforms into the $(\sqrt{3} \times 3) - 4\text{NO}$ structure, as is observed in Fig. 3.11

Although the $(\sqrt{3} \times 3) - 4\text{NO}$ structure was found in the kMC simulations of Fig. 3.7, the $(2 \times 2) - 3\text{NO}$ structure is not. Instead, the $(3 \times 3) - 7\text{NO}$ structure is preferred. Nevertheless, next to this work, the $(2 \times 2) - 3\text{NO}$ structure has been reported in many other experimental studies [21, 22, 23, 24, 39]. Several reasons for this mismatch between theory and experiment can be given. First, it can be attributed to the error in the DFT calculations. According to the Bayesian analysis, the average error of all the DFT calculated adlayer configurations is 3.51 kJ/mol, which is comparable to the difference in adsorption energy between the $(2 \times 2) - 3\text{NO}$ and $(3 \times 3) - 7\text{NO}$ structure, see Fig. 3.3. Being an average value, the error for these specific structures could be even larger, resulting in the preference for the $(3 \times 3) - 7\text{NO}$ structure. Alternatively, it is known that DFT calculations underestimate the stability of CO molecules bound to top adsorption sites [40]. If this is also true for NO molecules, the adsorption energy for the $(2 \times 2) - 3\text{NO}$ structure would be calculated to be higher than the adsorption energy of the $(3 \times 3) - 7\text{NO}$ configuration since it has more top adsorbed molecules per unit area. Finally, deviations between the DFT calculated adsorption energies and the adsorption energies calculated from the fitted kinetic parameters might be the cause, see Fig. 3.3. Overall, the fitted data points match the DFT values rather well. However, the fitted adsorption energy for the $(3 \times 3) - 7\text{NO}$ configuration is well below the DFT calculated point. As a result, this is the point where both lines of minimal adsorption energy deviate most. Consequently, the difference in adsorption energy at 0.75 ML between the data point of the $(2 \times 2) - 3\text{NO}$ structure and the (red) dashed line is approximately two times larger than for the (black) full line. This energy difference could be too large for the entropy to overcome and hence, the $(3 \times 3) - 7\text{NO}$ structure is favored to form.

3.4 Conclusion

In this work, the kinetic parameters of NO molecules adsorbed on a Rh(111) substrate are obtained from 73 DFT calculated structures. It is shown that pairwise

and homogeneous three particle interactions are important and that heterogeneous three and homogeneous four particle interactions do not play a role. Deviations from the zero temperature phase diagram as a result of entropy effects are studied by kinetic Monte Carlo simulations. Experimentally, structures with different coverage are studied by STM and compared to the simulations. The first adlayer structure that is found to form is the well-known 0.50 ML $(4 \times 2) - 4\text{NO}$ configuration. The onset of patch formation is observed at 0.30 ML in the experiment whereas theoretically domain growth only starts at 0.40 ML. This difference is attributed to subsurface impurities in the rhodium single crystal that serve as nucleation centers. In the simulations, two new structures were found at coverages of 0.60 ML and 0.67 ML that were confirmed experimentally. As these three structures all have a similar zigzag-like nature, the transition between them can be performed without a complete reordering of the molecules. Yet, these rearrangements are necessary when going to higher coverage. At these densities, however, the kinetic Monte Carlo simulations did not produce the experimentally observed 0.75 ML $(2 \times 2) - 3\text{NO}$ structure but instead a 0.78 ML $(3 \times 3) - 7\text{NO}$ configuration formed. In the STM experiment at 200 K, a metastable 0.50 ML $(2 \times 2) - 2\text{NO}$ structure was observed that seems to have originated from desorption of the top molecules of the $(2 \times 2) - 3\text{NO}$ structure. The few top molecules that remained were found to diffuse over the honeycombs of the $(2 \times 2) - 2\text{NO}$ structure on a timescale of minutes.

References

- [1] T. L. Einstein and J. R. Schrieffer, 'Indirect interaction between adatoms on a tight-binding solid,' *Phys. Rev. B*, **7**, 3629–3648 (1973).
- [2] H. P. Bonzel, 'Alkali-metal-affected adsorption of molecules on metal surfaces,' *Surf. Sci. Rep.*, **8**, 43–125 (1988).
- [3] S. J. Lombardo and A. T. Bell, 'A review of theoretical models of adsorption, diffusion, desorption, and reaction of gases on metal surfaces,' *Surf. Sci. Rep.*, **13**, 3–72 (1991).

3. Determination of adsorbate lateral interactions

- [4] W. A. Brown, R. Kose and D. A. King, ‘Femtomole adsorption calorimetry on single-crystal surfaces,’ *Chem. Rev.*, **98**, 797–832 (1998).
- [5] R. Brako and D. Šokčević, ‘Adsorbate-adsorbate interaction mediated by substrate lattice,’ *Surf. Sci.*, **454-456**, 623–627 (2000).
- [6] M. L. Merrick, W. Luo and K. A. Fichthorn, ‘Substrate-mediated interactions on solid surfaces: theory, experiment, and consequences for thin-film morphology,’ *Prog. Surf. Sci.*, **72**, 117–134 (2003).
- [7] J. K. Nørskov, *Coadsorption, promoters and poisons*, Elsevier, Amsterdam (1993).
- [8] R. M. van Hardeveld, R. A. van Santen and J. W. Niemantsverdriet, ‘C-N Coupling in reactions between atomic nitrogen and ethylene on Rh(111),’ *J. Phys. Chem. B*, **101**, 7901–7907 (1997).
- [9] J. T. Stuckless, C. E. Wartnaby, N. Al-Sarraf, S. J. Dixon-Warren, M. Kovar and D. A. King, ‘Oxygen chemisorption and oxide film growth on Ni(100), (110), and (111): sticking probabilities and microcalorimetric adsorption heats,’ *J. Chem. Phys.*, **106**, 2012–2030 (1997).
- [10] C. G. M. Hermse, F. Frechard, A. P. van Bavel, J. J. Lukkien, J. W. Niemantsverdriet, R. A. van Santen and A. P. J. Jansen, ‘Combining density-functional calculations with kinetic models: NO/Rh(111),’ *J. Chem. Phys.*, **118**, 7081–7089 (2003).
- [11] T. T. Tsong, ‘Field-ion microscope observations of indirect interaction between adatoms on metal surfaces,’ *Phys. Rev. Lett.*, **31**, 1207–1210 (1973).
- [12] F. Watanabe and G. Ehrlich, ‘Direct mapping of adatom-adatom interactions,’ *Phys. Rev. Lett.*, **62**, 1146–1149 (1989).
- [13] J. Trost, T. Zambelli, J. Wintterlin and G. Ertl, ‘Adsorbate-adsorbate interactions from statistical analysis of STM images: N/Ru(0001),’ *Phys. Rev. B*, **54**, 17850–17857 (1996).

-
- [14] J. Repp, F. Moresco, G. Meyer, K. H. Rieder, P. Hyldgaard and M. Persson, ‘Substrate mediated long-range oscillatory interaction between adatoms: Cu/Cu(111),’ *Phys. Rev. Lett.*, **85**, 2981–2984 (2000).
- [15] N. Knorr, H. Brune, M. Epple, A. Hirstein, M. A. Schneider and K. Kern, ‘Long-range adsorbate interactions mediated by a two-dimensional electron gas,’ *Phys. Rev. B*, **65**, 115420 (2002).
- [16] L. Österlund, M. Ø. Petersen, I. Stensgaard, E. Lægsgaard and F. Besenbacher, ‘Quantitative determination of adsorbate-adsorbate interactions,’ *Phys. Rev. Lett.*, **83**, 4812–4815 (1999).
- [17] L. Köhler, G. Kresse, E. Lundgren, J. Gustafson, A. Mikkelsen, M. Borg, J. Yuhara, J. N. Andersen, M. Marsman and P. Varga, ‘High-coverage oxygen structures on Rh(111): adsorbate repulsion and site preference is not enough,’ *Phys. Rev. Lett.*, **93**, 266103 (2004).
- [18] T. J. Stasevich, T. L. Einstein and S. Stolbov, ‘Extended lattice gas interactions of Cu on Cu(111) and Cu(001): ab initio evaluation and implications,’ *Phys. Rev. B*, **73**, 115426 (2006).
- [19] W. Luo and K. A. Fichthorn, ‘First-principles study of substrate-mediated interactions on a compressed Ag(111) surface,’ *Phys. Rev. B*, **72**, 115433 (2005).
- [20] J. Wintterlin, J. Trost, R. Schuster, A. Eichler and J. S. McEwen, ‘Two-dimensional roughening of adsorbate islands in thermodynamic equilibrium,’ *Phys. Rev. Lett.*, **96**, 166102 (2006).
- [21] C. T. Kao, G. S. Blackman, M. A. van Hove and G. A. Somorjai, ‘The surface structure and chemical reactivity of Rh(111)-(2×2)-3NO by HREELS and dynamical LEED analysis,’ *Surf. Sci.*, **224**, 77–96 (1989).
- [22] D. G. Castner, B. A. Sexton and G. A. Somorjai, ‘LEED and thermal desorption studies of small molecules (H₂, O₂, CO, CO₂, NO, C₂H₄, C₂H₂ and C) chemisorbed on the rhodium (111) and (100) surfaces,’ *Surf. Sci.*, **71**, 519–540 (1978).

3. Determination of adsorbate lateral interactions

- [23] I. Zasada, M. A. van Hove and G. A. Somorjai, ‘Reanalysis of the Rh(111)-(2×2)-3NO structure using automated tensor LEED,’ *Surf. Sci.*, **418**, L89–L93 (1998).
- [24] K. B. Rider, K. S. Hwang, M. Salmeron and G. A. Somorjai, ‘Structure and dynamics of dense monolayers of NO adsorbed on Rh(111) in equilibrium with the gas phase in the torr pressure range,’ *Phys. Rev. Lett.*, **86**, 4330 (2001).
- [25] G. Kresse and J. Furthmüller, ‘Efficiency of ab-initio total energy calculations for metals and semiconductors using a plane-wave basis set,’ *Comput. Mater. Sci.*, **6**, 15–20 (1996).
- [26] G. Kresse and J. Furthmüller, ‘Efficient iterative schemes for ab-initio total-energy calculations using a plane-wave basis set,’ *Phys. Rev. B*, **54**, 11169–11186 (1996).
- [27] G. Kresse and J. Hafner, ‘Norm-conserving and ultrasoft pseudopotentials for first-row and transition elements,’ *J. Phys.: Condens. Matter*, **6**, 8245–8257 (1994).
- [28] A. van der Walle and G. Ceder, ‘Automating first-principles phase diagram calculations,’ *J. Phase Equilib.*, **23**, 348–359 (2002).
- [29] V. Blum and A. Zunger, ‘Structural complexity in binary BCC ground states: the case of BCC Mo-Ta,’ *Phys. Rev. B*, **69**, R020103 (2004).
- [30] A. P. J. Jansen and W. K. Offermans, ‘Lateral interactions in O/Pt(111): density-functional theory and kinetic Monte Carlo,’ in *Computational Science and Its Applications — ICCSA-2005, LNCS 3480* (editor O. Gervasi), Springer, Berlin (2005).
- [31] Y. Zhang, V. Blum and K. Reuter, ‘Accuracy of first-principles lateral interactions: oxygen at Pd(100),’ *Phys. Rev. B*, **75**, 235406–235406 (2007).
- [32] D. Sivia and J. Skilling, *Data analysis: a bayesian tutorial*, Oxford University Press, Oxford (2006).

- [33] C. Popa and A. P. J. Jansen, private communication.
- [34] J. J. Lukkien, J. P. L. Segers, P. A. J. Hilbers, R. J. Gelten and A. P. J. Jansen, ‘Efficient Monte Carlo methods for the simulation of catalytic surface reactions,’ *Phys. Rev. E*, **58**, 2598–2610 (1998).
- [35] A. P. J. Jansen, ‘An introduction to Monte Carlo simulations of surface reactions,’ *arXiv:cond-mat/0303028v1 [cond-mat.stat-mech]* (2003).
- [36] M. Mavrikakis, J. Rempel, J. Greeley, L. B. Hansen and J. K. Nørskov, ‘Atomic and molecular adsorption on Rh(111),’ *J. Chem. Phys.*, **117**, 6737–6744 (2002).
- [37] T. W. Root, L. D. Schmidt and G. B. Fisher, ‘Adsorption and reaction of nitric oxide and oxygen on Rh(111),’ *Surf. Sci.*, **134**, 30–45 (1983).
- [38] M. K. Rose, A. Borg, T. Mitsui, D. F. Ogletree and M. Salmeron, ‘Subsurface impurities in Pd(111) studied by scanning tunneling microscopy,’ *J. Chem. Phys.*, **115**, 10927–10934 (2001).
- [39] G. Witte, ‘Low-energy dynamics of CO and NO chemisorbed on Rh(111),’ *J. Chem. Phys.*, **115**, 2757–2767 (2001).
- [40] G. Kresse, A. Gil and P. Sautet, ‘Significance of single-electron energies for the description of CO on Pt(111),’ *Phys. Rev. B*, **68**, 073401 (2003).

Chapter 4

STM appearances of NO on Rh(111)

4.1 Introduction

In both optical and electron microscopy a sample surface is probed by the reflection or transmission of particles (photons or electrons) the sample is exposed to. The transmitted or reflected signal depends only on the scattering of the particles from the surface features and, under normal circumstances, the surface will always be imaged in the same way. In scanning tunneling microscopy (STM), however, the sample is probed by tunneling electrons, the current of which is not only dependent on the sample but also on the tip as is shown in equation (2.1.2). For a relatively blunt tip, the density of states is rather smooth and can be taken constant. For a sharp tip, however, the density of states consists of local electron states and has to be taken into account explicitly [1]. This effect is greatest when a foreign species (atom or molecule) is adsorbed on the tip apex, a so-called functionalized tip. Although enhancing/changing the image contrast [2, 3, 4] or even providing chemical contrast [5, 6, 7], care must be taken when using STM to determine adsorbate structures [8]. A small change in the configuration of the tip could have a great influence on the imaging of the surface. In fact, many topographic STM images are wasted by experimentalists qualifying them to be taken with so-called "bad" tips. Previously, STM simulations have been used to study the influence of the tip apex structure on the imaging [9,

4. STM appearances of NO on Rh(111)

10, 11, 12, 13]. In this chapter we have taken a different view. As each tip leaves its fingerprint on the image, the role of the tip and sample is interchanged and the relatively simple and well defined NO/Rh(111) system is used to probe the tip apex. To this end the tip is scanned with different known NO structures and the results are compared to STM simulations using different kind of tips.

4.2 Experiment

In section 2.3 the Rh(111) cleaning procedure and the NO deposition method was described. The two structures that we are focussing on in this chapter are the $(4 \times 2) - 4\text{NO}$ and $(2 \times 2) - 2\text{NO}$ structure (see Fig. 3.1 and Fig. 3.4). Since the tip is already mounted in the STM during exposure of the sample to the NO gas (section 2.3.1), it will also be covered by NO molecules. As soon as stable imaging is obtained, an STM image of the structure is recorded. Then, the tip apex is changed in order to obtain a stable tip with a different termination. As soon as the same structure appears differently, a new image is recorded.

In STM there are two ways of modifying the tip apex. In the first method, the tip is quickly indented (up to 7.5 Å) into the rhodium sample after which it is gently retracted. Due to adhesive forces between tip and sample, a neck will form upon retraction [14, 15]. As tungsten is one of the hardest metals, the pulled neck will consist mainly of the sample material. At a certain point during retraction, the neck will break and the shape of the tip apex is modified. Alternatively, voltage pulses up to ± 10 V can be applied between tip and sample. Due to the sharpness of the tip and the close tip-sample distance, the high electric field thus generated induces material to be transferred from tip to sample or vice versa [16, 17]. It should be noted that, next to transfer of material, voltage pulses might also break the intermolecular bond [18] and hence could dissociate the NO molecule.

Although the tip can be changed, it is very hard to experimentally *determine* what the tip apex looks like. Therefore STM topographic images have been simulated using different kind of model tips. The simulated images are compared to the experimental results in order to discover a relation between the apparent imaging of the structure

and the tip functionalization.

4.3 Theory

Theoretically, the topographic STM image is obtained as follows: at a certain position on the substrate, the feedback loop moves the tip towards or away from the surface until the setpoint current is reached. The height of the tip is recorded and it is moved to the next position. This way, as the tip is scanned over the surface, a topographic image is obtained.

4.3.1 GREEN formalism

Within the GREEN formalism [19, 20, 21, 22], the building of the STM configuration goes part by part using building blocks called principal layers (PL). A PL is a stack of atomic planes thick enough so that interactions between second neighboring PLs can be neglected, meaning that the cut-off radius of the Hamiltonian should be less than the thickness of two PLs.

First the semi-infinite bulk parts of the tip T and sample S are built. To this end a PL is constructed and infinitely stacked. Neighboring PLs in the stack are coupled electronically through a Green's function (G_{TT} for the tip and G_{SS} for the sample) that is obtained from an iterative algorithm [20, 23]. After the semi-infinite tip electrode T is finished, the tip apex PL t is added according to the surface Green's function matching method (SGFM) [24]. The Green's function G_{tt}^0 of the combined Tt block projected at the tip apex PL t , may be expressed as

$$G_{tt}^0(E) = \frac{1}{EO_{tt} - H_{tt} - \Sigma_{Tt}}, \quad (4.3.1)$$

where E is the energy and H_{tt} and O_{tt} are the intra PL Hamiltonian and overlap matrices at t , respectively. The self-energy Σ_{Tt} accounts for the presence of the bulk tip electrode T at PL t and can be written as

$$\Sigma_{Tt} = F_{tT}G_{TT}F_{Tt}, \quad (4.3.2)$$

4. STM appearances of NO on Rh(111)

where $F_{tT} = EO_{tT} - H_{tT}$ is the secular matrix. Similarly, the surface PL s is added to the bulk sample electrode S and the Green's function G_{ss}^0 at the sample surface has a form similar to (4.3.1).

Generally, since the sample electrode is periodic in two dimensions, G_{ss}^0 is calculated over a fine grid of k -points in the surface Brillouin zone. The tip apex, however, does not have any periodicity and hence, G_{tt}^0 is only evaluated at the Gamma point.

Finally, both electrodes are brought close to each other. The matching of the block Green's functions is carried out using the Dyson equation, that may be reduced to the following set of equations:

$$G_{ss} = G_{ss}^0 - G_{ss}^0 F_{st} G_{ts} \quad (4.3.3a)$$

$$G_{ts} = G_{ts}^0 - G_{tt}^0 F_{ts} G_{ss} \quad (4.3.3b)$$

$$G_{tt} = G_{tt}^0 - G_{tt}^0 F_{ts} G_{st} \quad (4.3.3c)$$

$$G_{st} = G_{st}^0 - G_{ss}^0 F_{st} G_{tt}, \quad (4.3.3d)$$

where $G_{st}^0 = G_{ts}^0 \equiv 0$ and G_{st} and G_{ts} are the Green's functions after matching. Typically, in an STM configuration, the interactions between the tip and sample are weak and hence equations (4.3.3) for PL s and t may be approximated up to first order:

$$G_{st} = G_{st}^0 - G_{ss}^0 F_{st} G_{tt}^0 + G_{ss}^0 F_{st} G_{tt}^0 F_{ts} G_{st}^0 - G_{ss}^0 F_{st} G_{tt}^0 F_{ts} G_{ss}^0 F_{st} G_{tt}^0 + \dots \approx -G_{ss}^0 F_{st} G_{tt}^0. \quad (4.3.4)$$

Although an approximation, typically it yields very accurate results for STM simulations, due to the relatively large distance between tip and sample as compared to atomic distances.

The total elastic current at zero temperature between tip and sample can now be written as a sum of dimensionless transmission coefficients across the surface (or tip) PL $\mathcal{T}_s(E, V, k, \sigma)$:

$$I_s(V) = \frac{e}{\pi\hbar} \int_0^{eV} \sum_{k,\sigma} \mathcal{T}_s(E, V, k, \sigma) dE, \quad (4.3.5)$$

where k runs over all k -points of the Brillouin zone and σ is the spin component. Dropping the E , V , k and σ dependence, \mathcal{T}_s may be written as [25]

$$\mathcal{T}_s = \text{Tr}[G_{st}\Gamma_{Tt}G_{st}^\dagger\Gamma_{Ss}], \quad (4.3.6)$$

where Tr stands for the trace and the contact matrices Γ_{Tt} and Γ_{Ss} may be viewed as charge injection velocities at the tip apex and surface, respectively:

$$\Gamma_{Tt(Ss)} = i(\Sigma_{Tt(Ss)} - \Sigma_{Tt(Ss)}^\dagger). \quad (4.3.7)$$

Using (4.3.4), we obtain

$$\mathcal{T}_s = \text{Tr}[G_{ss}^0 F_{st} G_{tt}^0 \Gamma_{Tt} [G_{tt}^0]^\dagger F_{st}^\dagger [G_{ss}^0]^\dagger \Gamma_{Ss}]. \quad (4.3.8)$$

This expression may be simplified by defining the matrices $A_t = G_{tt}^0 \Gamma_{Tt} [G_{tt}^0]^\dagger$ and $A_s = G_{ss}^0 \Gamma_{Ss} [G_{ss}^0]^\dagger$ which only depend on the unperturbed tip and sample system. After some arrangements within the trace we have

$$\mathcal{T}_s = \text{Tr}[F_{st} A_t F_{st}^\dagger A_s]. \quad (4.3.9)$$

The A matrices may be diagonalized at PLs s and t :

$$A_{s(t)} = \sum_m |u_{A_{s(t)}}^m\rangle \langle u_{A_{s(t)}}^m|, \quad (4.3.10)$$

where the eigenvectors $|u_{A_{s(t)}}^m\rangle$ are scaled by the square root of the corresponding eigenvalue and the summation over m is restricted to those eigenstates with a non zero eigenvalue. This expression allows us to rewrite the transmission coefficient \mathcal{T}_s as

$$\mathcal{T}_s = \sum_{ms,mt} |\langle u_{A_s}^{ms} | F_{st} | u_{A_t}^{mt} \rangle|^2, \quad (4.3.11)$$

which is very reminiscent to broadly used Landauer-Büttiker formula [26]. Notice the convenience of this expression for a fast evaluation of the current. The eigenvectors $|u_{A_t}^{mt}\rangle$ and $|u_{A_s}^{ms}\rangle$ may be saved on disk after a reference calculation performed

4. STM appearances of NO on Rh(111)

independently for the tip and the sample. For STM imaging, it is then sufficient to read these eigenvectors and evaluate F_{st} for each position of the tip above the surface.

Expression (4.3.11) also permits a decomposition of \mathcal{T} into orbitals in terms of tunneling paths linking states at the apex and substrate together with the interference among these tunneling paths. Denoting the orbitals at PL s by α and those at t by β , we obtain

$$\mathcal{T}_s = \sum_{\alpha\beta\alpha'\beta'} \sum_{ms,mt} \langle u_{A_s}^{ms} | \alpha \rangle F_{st}^{\alpha\beta} \langle \beta | u_{A_t}^{mt} \rangle \langle u_{A_t}^{mt} | \beta' \rangle F_{ts}^{\beta'\alpha'} \langle \alpha' | u_{A_s}^{ms} \rangle. \quad (4.3.12)$$

By defining transmission amplitudes

$$TA_{ms,mt}^{\alpha\beta} = \langle u_{A_s}^{ms} | \alpha \rangle F_{st}^{\alpha\beta} \langle \beta | u_{A_t}^{mt} \rangle, \quad (4.3.13)$$

an expression can be written that is suitable for the explicit evaluation of the interference terms \mathcal{I} between any two tunneling paths $(\alpha - \beta)$ and $(\alpha' - \beta')$, see Fig. 4.1:

$$\mathcal{I}^{\alpha\beta\alpha'\beta'} = \sum_{ms,mt} TA_{ms,mt}^{\alpha\beta} [TA_{ms,mt}^{\alpha'\beta'}]^*. \quad (4.3.14)$$

The total transmission coefficient can now be written as

$$\mathcal{T} = \sum_{\alpha\beta\alpha'\beta'} \mathcal{I}^{\alpha\beta\alpha'\beta'}. \quad (4.3.15)$$

4.3.2 Extended Hückel theory

Ideally, when performing any tight-binding based calculation, it is desirable to have an ab-initio Hamiltonian available. The self-consistent Hamiltonian matrix elements calculated using an external LCAO based code, can then be used within GREEN. However, first-principles calculations for any reasonably large system result in highly expensive calculations. Alternatively, one may use an empirical tight-binding Hamiltonian which, although not as accurate as the first-principles one, may provide reasonably good results from a qualitative (or even quantitative) point of view. Generally, the STM is a complex system in which short-range interaction within and long-range

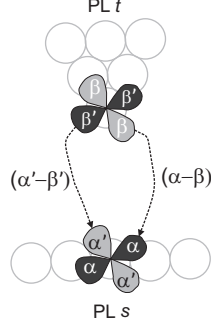


Figure 4.1: Schematic illustration showing different tunnel trajectories between tip and sample giving rise to interference effects. Each labeled two-lobed figure represents an atomic orbital at which an electron trajectory can start or end.

interactions between tip and sample (i.e. exponential decay of the wave functions in the vacuum) have to be described properly by the Hamiltonian. The extended Hückel theory (EHT) provides a fairly good qualitative description of the main processes that control the contrast in STM, as is shown in [21].

In the EHT [27], the interaction $H_{ai,bj}$ between atomic orbitals (AO) i and j centered at atoms a and b are proportional to their corresponding overlap $O_{ai,bj}$:

$$H_{ai,bj} = K_{EHT} \frac{E_{ai} + E_{bj}}{2} O_{ai,bj}. \quad (4.3.16)$$

Here, the on-site energy E_{ai} corresponds to the matrix diagonal element $H_{ai,ai}$ and the constant of proportionality K_{EHT} is a dimensionless constant, taken to be 2.3 [19].

In the AO basis set used, each AO i is associated to a set of numbers (σ, n, l, m) , where n is the principal quantum number, σ the spin component, l the angular momentum and m the z component of the angular momentum. The radial part of the wave function for each AO is described by a double- ζ Slater wave function. Apart from the on-site energies, this leads to three parameters per l quantum number: the exponents ζ_1 and ζ_2 and the coefficient c_1 of the first exponential. The coefficient of the second exponential, c_2 , is determined by imposing normalization of the wave function.

For bulk materials, these parameters are fitted to band structure calculations and are given in [19]. The surface and apex PL structures are first optimized using DFT

4. STM appearances of NO on Rh(111)

calculations. The optimized atom coordinates are directly used in the PLs and the EHT parameters are obtained by fitting the PDOS of each atom to the DFT calculated PDOS.

Using NO molecules, it is more natural to speak about molecular orbitals (MO) instead of atomic orbitals. The MOs are obtained by diagonalization of the Hamiltonian for the isolated molecule. Having four AOs per atom, the NO molecule has eight MOs (see Fig. 1.1). In Fig. 4.2, plots of the calculated LDOS for each MO of the NO molecules in the $(2 \times 2) - 2\text{NO}$ structure are shown for the energy range from -10 eV to 10 eV. The fcc adsorbed N and O atoms are indicated by black and gray circles in the plots of the total LDOS. The hcp N and O atoms are symbolized by black and gray boxes. In the side views, both fcc and hcp bound molecules are visible. In the top view the honeycomb-like structure of the molecules can be recognized. The π_{2p_x} and π_{2p_y} orbitals are degenerate and therefore grouped together in $\pi_{2p_{xy}}$. Similarly $\pi_{2p_x}^*$ and $\pi_{2p_y}^*$ are grouped into $\pi_{2p_{xy}}^*$.

The PDOS for each MO is shown in the last column of the figure. The full line represents the fcc adsorbed molecule, the dashed line the hcp molecule. Note that for each MO, the PDOS is scaled by a factor that is indicated at the curve. As in STM only small bias voltages are used, it is useful to consider the PDOS in a small energy range around the Fermi energy. Here $\pi_{2p_{xy}}^*$ has the highest PDOS, followed by $\pi_{2p_{xy}}$ and σ_{2p_z} . Therefore, these MOs might be expected to contribute most to the total tunneling current. It is important to notice that in top view, the MOs of the fcc molecule are brighter than of the hcp molecule. As the PDOS of the fcc and hcp molecules are very similar, this difference is attributed to the fcc MOs extending further in the z -direction than the MOs of the hcp molecule. The LDOS and PDOS of the MOs of the molecules in the $(4 \times 2) - 4\text{NO}$ structure qualitatively look similar to the ones shown in Fig. 4.2.

4.3.3 STM configurations

Two different structures for the NO on Rh(111) system have been constructed: the $(2 \times 2) - 2\text{NO}$ and $(4 \times 2) - 4\text{NO}$ structure. Each structure was optimized [28] in both the VASP [29, 30, 31] and SIESTA [32, 33, 34, 35] code and are depicted in

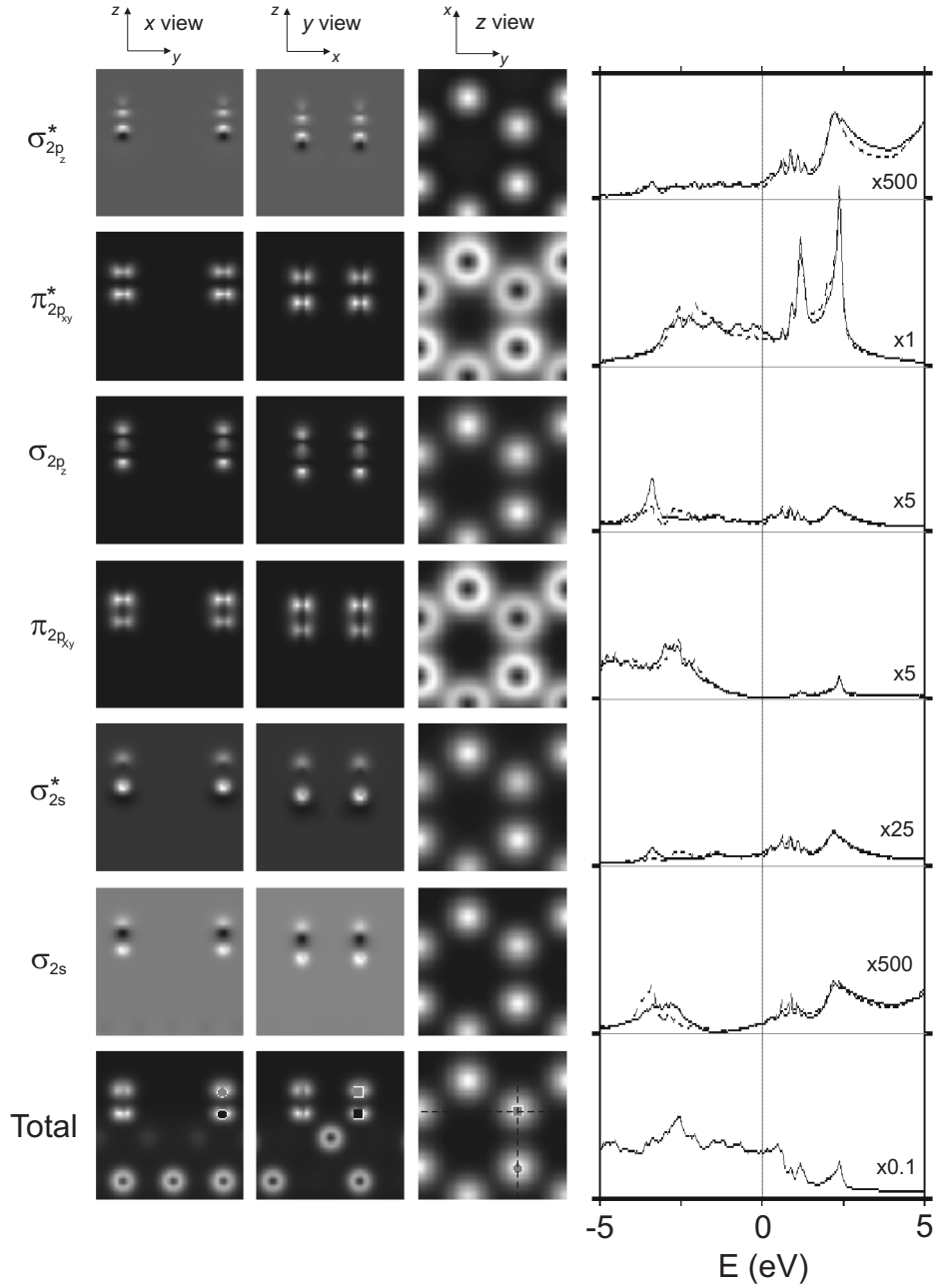


Figure 4.2: Plot of the LDOS of the molecular orbitals of the NO molecules in the $(2 \times 2) - 2\text{NO}$ structure. In the total LDOS, black labels represent oxygen atoms, gray labels nitrogen atoms. Circles are used to refer to the fcc adsorption site and boxes symbolize the hcp sites. In the z view, the dashed lines indicate the position of the cross sections taken for the x and y views. In the last column, the PDOS for each molecular orbital is shown from -5 eV to 5 eV. Full and dashed lines represent the fcc and hcp molecules, respectively. For each MO, the PDOS is scaled by a factor that is indicated at the curve.

4. STM appearances of NO on Rh(111)

Fig. 4.3.

In Fig. 4.4 and Fig. 4.5, ten different tip apex PLs that were all optimized using SIESTA are illustrated. Each of the apexes consists of a pyramid of W atoms. The crystal structure of the W tips is BCC except for tips 4.5(c) to 4.5(e) that have an FCC structure. The crystallographic direction along the z -axis is either $\langle 111 \rangle$ or $\langle 110 \rangle$, as is indicated in the text at each tip. In BCC crystals the $\langle 111 \rangle$ direction is relatively open, while the $\langle 111 \rangle$ direction of the FCC structure is the most compact one, just as the $\langle 110 \rangle$ direction in BCC crystals.

A clean apex consists solely of W atoms (Fig. 4.4(a) and 4.4(b)). Note that recently, STM simulations have been performed on different NO structures on Rh(111) using these kind of tips [36]. A contaminated tip can have an NO molecule adsorbed (Fig. 4.5) or one of the molecule's constituents, an N or O atom (Fig. 4.4(c) to 4.4(e)). Adsorption can take place either directly on top of a single W atom (Fig. 4.5(b) and 4.5(d)) or the adsorbate can bind to multiple W atoms (Fig. 4.4(c) to 4.4(e), 4.5(a), 4.5(c) and 4.5(e)). Finally, the NO molecules can adsorb upright (Fig. 4.5(b), 4.5(d) and 4.5(e)) and flat (Fig. 4.5(a) and 4.5(c)) to the tip apex.

Prior to starting a scan, a tip can be rotated around its x , y and z -axis. This is illustrated in the second picture of Fig. 4.5(c). Here the tip is rotated 45° around its y -axis in order to expose the NO molecule to the substrate to ensure the tunneling current is going through the molecule. Note that, due to this rotation, the atoms from the bulk tip electrode approach the surface very closely. However, these atoms do not contribute to the current as it is only the atoms from the tip apex PL that interact with the sample.

4.4 Results and discussion

4.4.1 $(2 \times 2) - 2\text{NO}$

In the first column of Fig. 4.6, several different experimental appearances of the $(2 \times 2) - 2\text{NO}$ structure are shown. In the second and third column of each row, the theoretically simulated STM images are depicted that match the experimental one best. The accompanying text indicates the tip with which the image is created. The

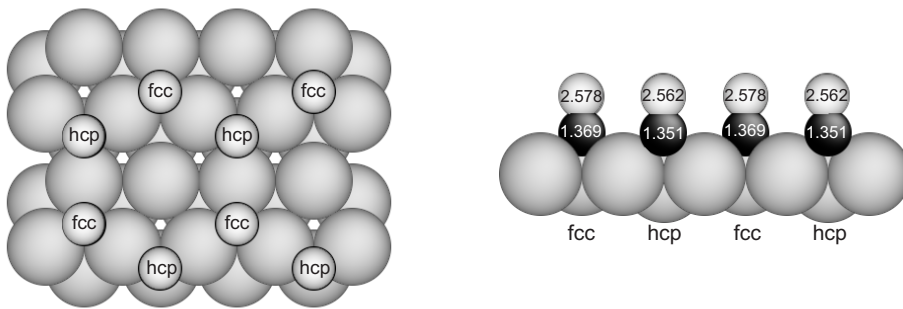
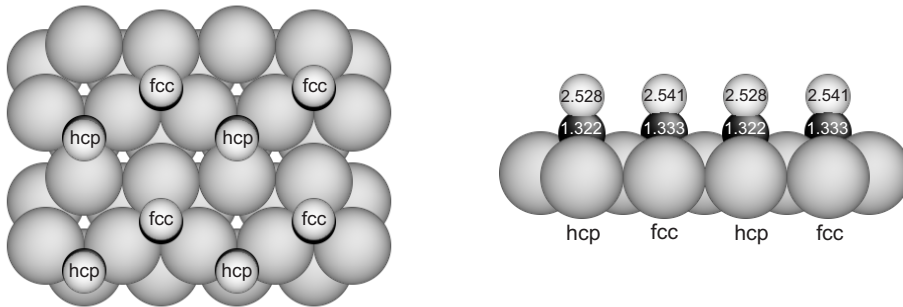
(a) $(2 \times 2) - 2\text{NO}$ structure(b) $(4 \times 2) - 4\text{NO}$ structure

Figure 4.3: Top and side view of the two VASP optimized sample structures. The height of the N and O atoms with respect to the top layer of Rh atoms are given in Å. Black, light gray and white atoms represent the N, Rh and O atoms, respectively.

4. STM appearances of NO on Rh(111)

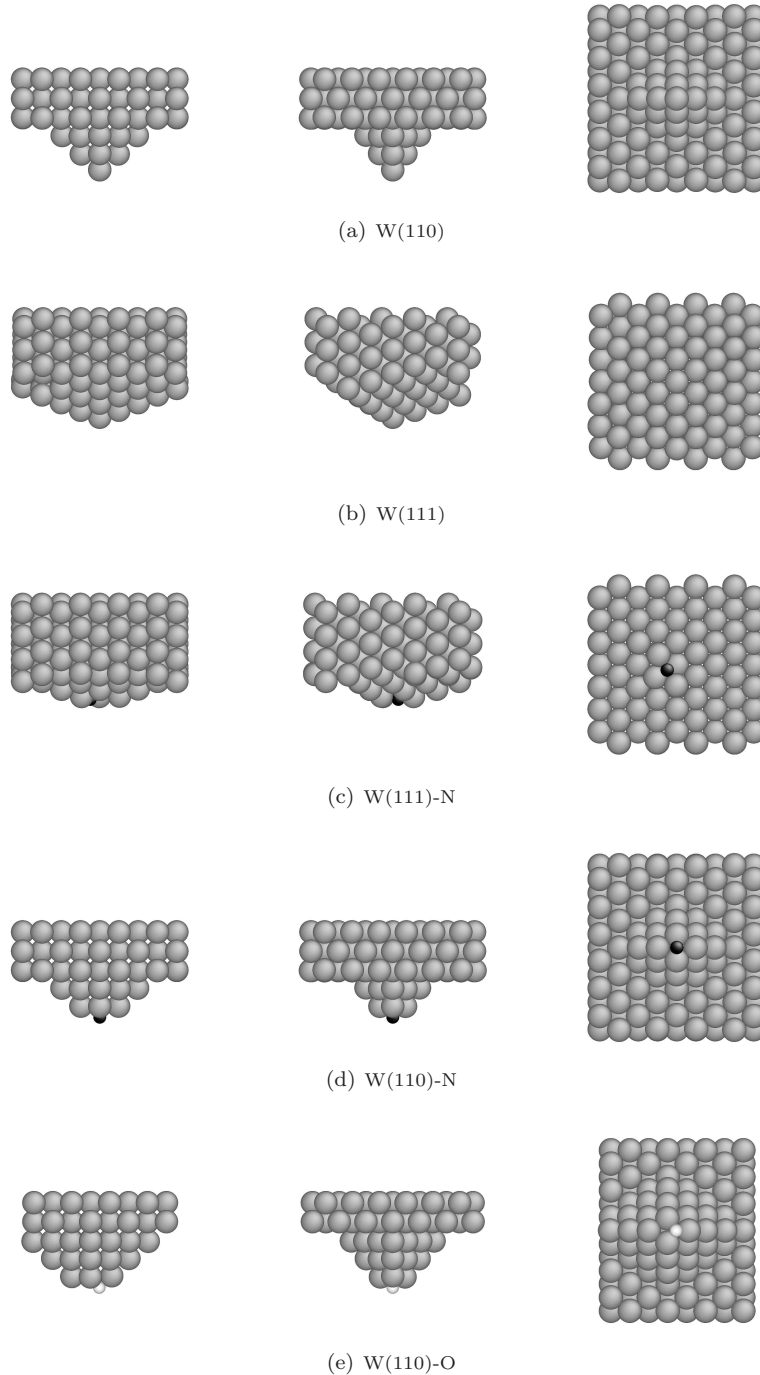


Figure 4.4: The tips used for the simulation of the STM images. The top two tips are clean, the other tips are contaminated by the constituents of the NO molecule: an N (tip (c) and (d)) or an O atom (tip (e)). Each tip is shown along the x -axis (left), the y -axis (middle) and the z -axis (right). All tips have the BCC structure. The crystallographic direction along the z -axis is $\langle 110 \rangle$ for tip (a), (d) and (e) and $\langle 111 \rangle$ for tip (b) and (c). Black atoms represent nitrogen, gray tungsten and white oxygen.

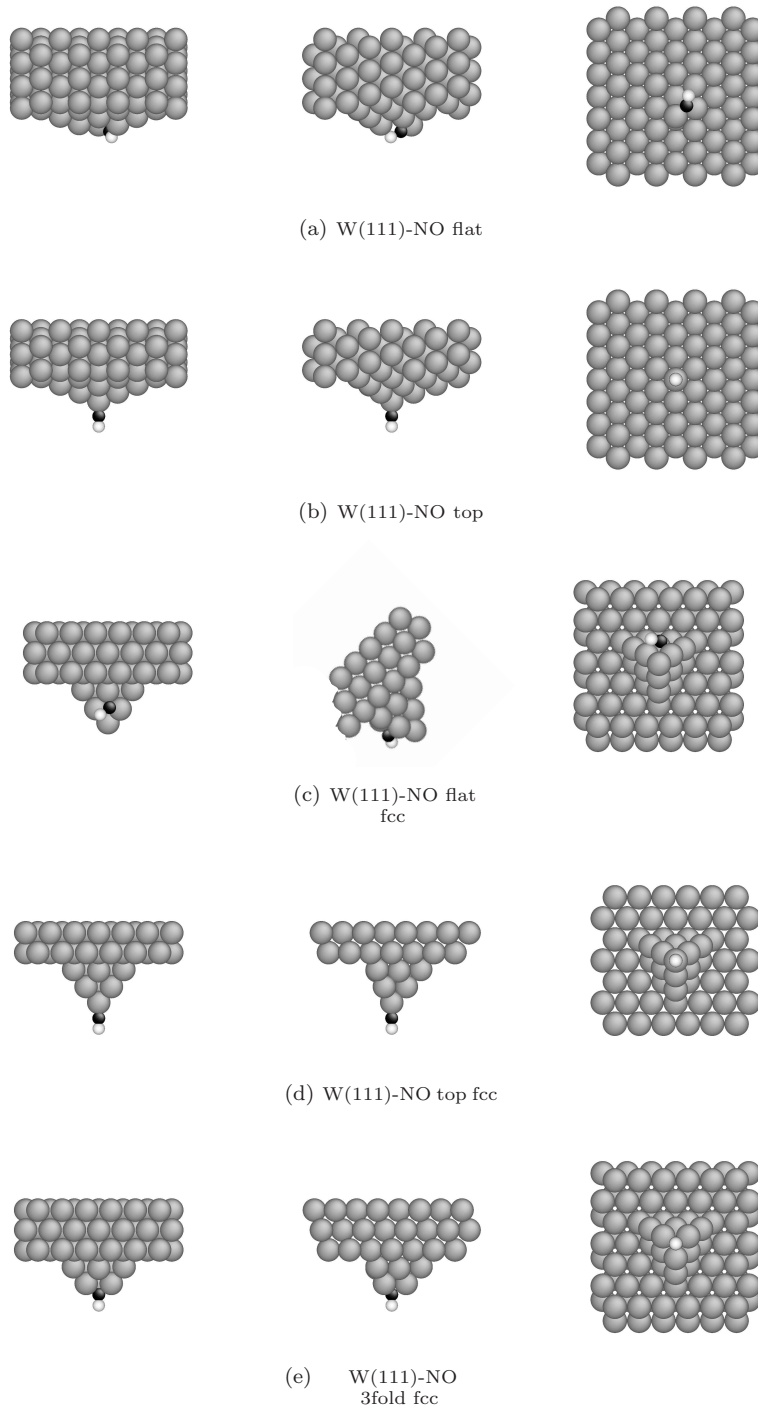


Figure 4.5: The modeled NO terminated tips. Tip (a) and (b) have the BCC structure, tip (c), (d) and (e) the FCC structure. The crystallographic direction along the z -axis is $\langle 111 \rangle$ for all tips. In the second picture of tip (c), the tip is shown rotated by 45° around the y -axis. This rotated configuration is used in the calculations in order to expose the NO to the surface. Black atoms represent nitrogen, gray tungsten and white oxygen.

4. STM appearances of NO on Rh(111)

corrugation d , which is the difference between the minimum and maximum height of the imaged structure, is given for each picture. When applicable, the apparent height difference Δ between the NO molecules adsorbed at the fcc and hcp position is indicated. The dark filled circle and box in the theoretical images symbolize the fcc and hcp adsorption site, respectively.

Fig. 4.6(a) shows a mixture of the $(2 \times 2) - 2\text{NO}$ and the $(2 \times 2) - 3\text{NO}$ structure (cf. Figs. 3.1 and 3.4): $\sim 30\%$ of the honeycombs in the $(2 \times 2) - 2\text{NO}$ structure are filled. In the $(2 \times 2) - 2\text{NO}$ structure, all six NO molecules that constitute the honeycomb are clearly resolved. The molecules adsorbed in fcc and hcp positions appear almost equally bright. With a height difference $\Delta = 3$ pm on a total corrugation of 60 pm, the contrast between the two molecules $\frac{\Delta}{d} = 5\%$. The simulated image in Fig. 4.6(b) is taken using tip 4.5(b) having an NO molecule standing upright on the tip. This image does not only qualitatively look similar to the experimental one, but d and $\frac{\Delta}{d}$ also match closely ¹. The result is approximately the same for all tips in which the NO molecule is standing upright on the apex, as is illustrated by Fig. 4.6(c) that is taken by tip 4.5(e).

In order to gain a more detailed understanding of the tunneling process of this type of configuration, the contribution of each atomic orbital to the total current flowing across the tip-sample interface is evaluated for a fixed position of the tip above the surface. In Fig. 4.7(a), the sample contribution per MO α on the sample, $\sum_{\beta\alpha'\beta'} \mathcal{I}^{\alpha\beta\alpha'\beta'}$, see equation (4.3.14), is shown. Similarly, the contribution for each tip MO β , $\sum_{\alpha\alpha'\beta'} \mathcal{I}^{\alpha\beta\alpha'\beta'}$ is shown in Fig. 4.7(b). The NO molecules have 8 MOs (Fig. 4.2) whereas the substrate Rh and tip W atoms have 9: s, p_x , p_y , p_z , $d_{x^2-y^2}$, $d_{x^2-z^2}$, d_{xy} , d_{xz} and d_{yz} . In both graphs, the current contribution is considered above the hcp and fcc NO molecule (square and circle in Fig. 4.6(b)) and is illustrated by the dark and light gray bar, respectively.

The main contribution (90%) of both electrodes comes from $\pi_{2p_{xy}}^*$ of both tip and sample NO molecules. From equations (2.1.2), it can be seen that the tunneling current is proportional to the PDOS of both tip and sample. On the right side of

¹It must be noted that as the GREEN code is semi-quantitative, we cannot always expect perfect agreement for the corrugation values.

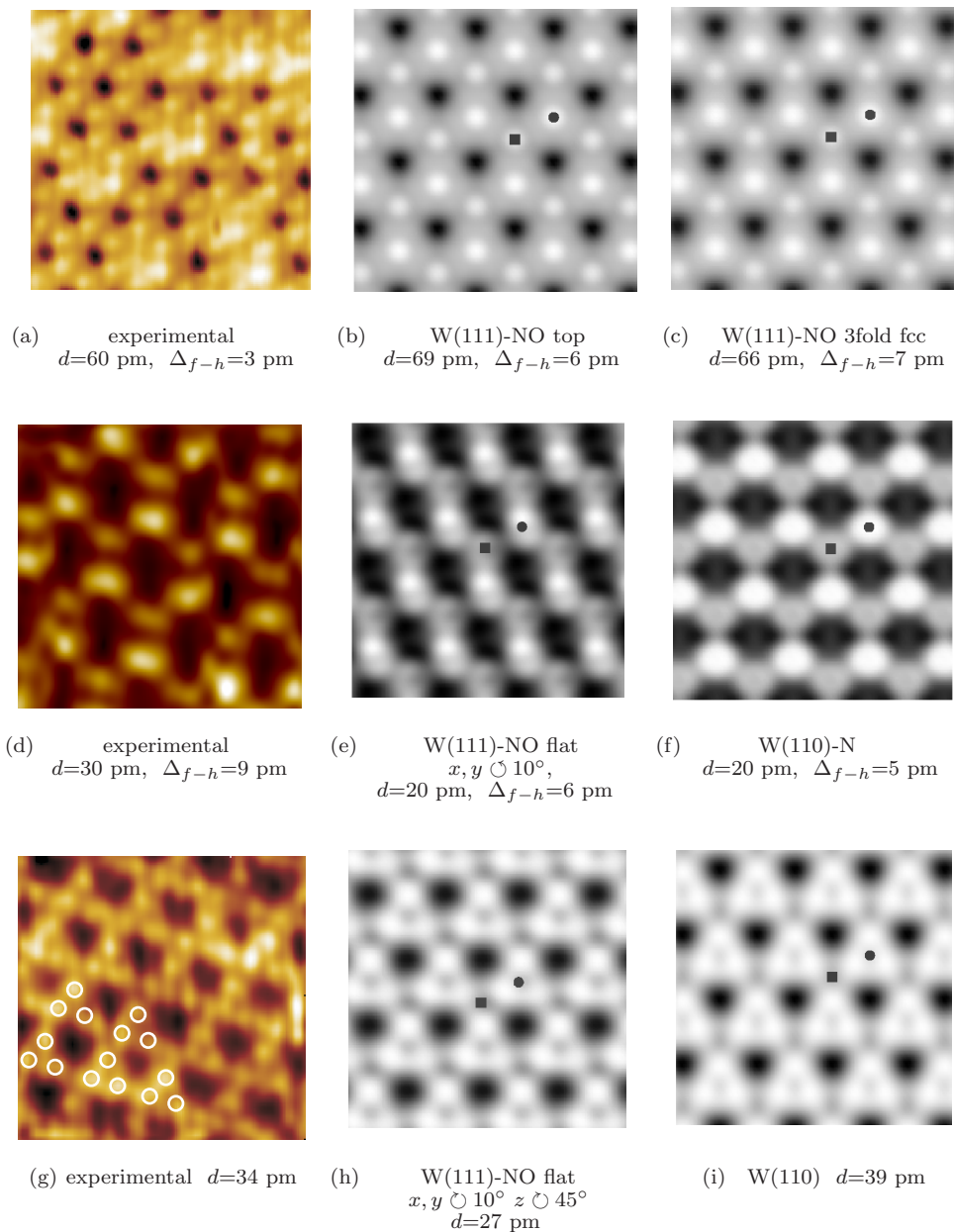
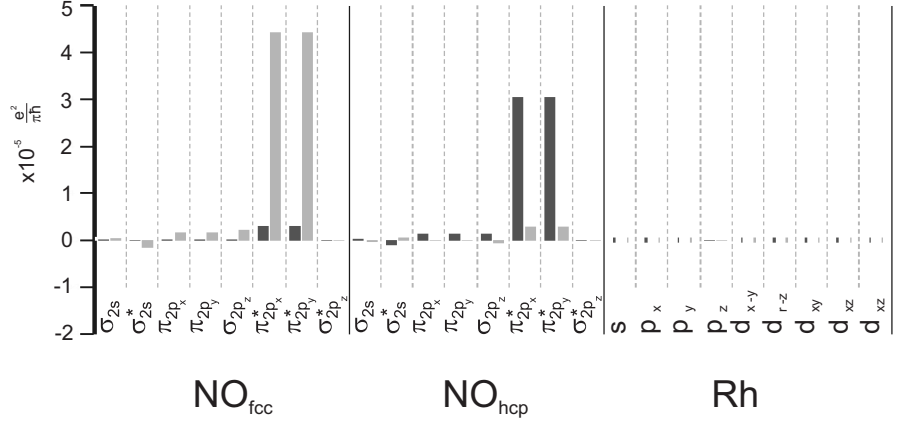
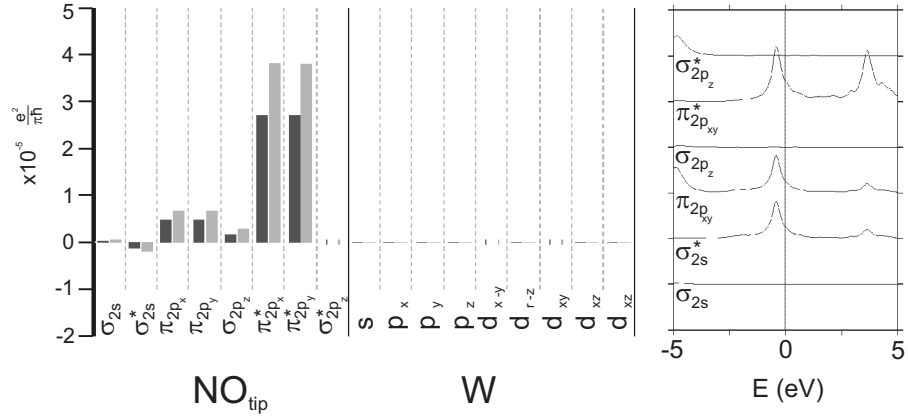


Figure 4.6: Comparison between the experimental and calculated appearances of the $(2 \times 2) - 2\text{NO}$ structure. Each row represents one kind of imaging. The first column depicts the experimentally obtained pictures. The second and third column show the theoretical pictures that match the experimental one best. The accompanying text indicates which tip the picture is simulated with. In (e) and (h) the tip is rotated. For all images, the corrugation d is given. The height difference Δ between the hcp and fcc adsorbed molecules is given when applicable. The hcp and fcc sites are indicated by the dark square and circle, respectively. The white circles in (g) emphasize the bright dots being grouped in triangles. The theoretical images are 2×2 nm² and are taken with $V = 100$ mV, $I = 0.500$ nA. The substrates in (h) and (i) are optimized in SIESTA, the rest using VASP. The experimental parameters are: (a) 3×3 nm², $V = -99$ mV, $I = 0.44$ nA, (d) 2×2 nm², $V = -99$ mV, $I = 0.44$ nA, (g) 3×3 nm², $V = -99$ mV, $I = 0.25$ nA.

4. STM appearances of NO on Rh(111)



(a) $(2 \times 2) - 2\text{NO}$ structure



(b) W(111)-NO top tip (tip 4.5(b))

Figure 4.7: Analysis of the orbital contribution to the tunneling current for the configuration of Fig. 4.6(b). The main orbital contribution comes from $\pi_{2p_{xy}}^*$ of the molecules on both tip and sample. In (b), next to the orbital contribution, the PDOS of the NO atom on the tip is shown.

Fig. 4.7(b) the PDOS of the tip-bound NO is shown. Comparing this graph to the PDOS of the NO molecule on the substrate (Fig. 4.2) the PDOS of $\pi_{2p_{xy}}^*$ is highest at the Fermi energy in both cases. As opposed to the molecules at the sample, σ_{2s}^* and $\pi_{2p_{xy}}$ of the tip also have a considerable amount of states at E_F . Indeed, though smaller, the contribution of these orbitals is also visible in Fig. 4.7(b).

The physical height difference between the molecules adsorbed at the fcc and hcp site is 1.6 pm (Fig. 4.3), too small to explain the apparent height difference Δ , ranging from 3-7 pm. In the Tersoff-Haman approximation (see section 2.1), however, the STM imaging is proportional to the LDOS of the substrate. As can be seen in the top view of Fig. 4.2, the MOs at the fcc site appear brighter than the MOs of the hcp bound molecule. Since their PDOS is similar, this means that the MOs of the fcc molecule extend further in the z -direction. Therefore, although an approximation, Δ can be expected to be larger than the physical height difference between the molecules. The relatively high corrugation d of the images in Fig. 4.6(a) to 4.6(c) can be explained by a geometrical effect: a tip with an NO attached upright is very sharp. When the tip is positioned over the middle of a hexagon in the $(2 \times 2) - 2NO$ structure, the distance between the tip molecule and the molecules that constitute the hexagon is too large ever to reach the setpoint current. Therefore, the tip has to move down in the hexagon until its NO molecule has sufficient overlap with the rhodium atoms of the substrate.

For a tip that does not have an NO molecule upright at its apex, the individual NO molecules in the $(2 \times 2) - 2NO$ structure could either not be resolved so well or $\frac{\Delta}{d}$ is larger than 5%. Fig. 4.6(d) is an example of an experimental image in which the fcc adsorbed NO molecule is clearly imaged brighter than the NO molecule adsorbed at the hcp site ($\frac{\Delta}{d} = 30\%$). Tips that could resolve the individual molecules with this contrast have an apex with either a flat lying NO or an N or O atom at its end. Fig. 4.6(e) and 4.6(f) show calculated images taken with the W(111)-NO flat tip (tip 4.5(a)) and the W(110)-N tip (tip 4.4(d)), respectively. The W(111)-NO flat tip was rotated by 10° in the counter clockwise direction around the x and y axis to expose the molecule fully to the substrate, a procedure similar to the one explained in Fig. 4.5(c). The absolute values for d and Δ are higher for the experimental picture

4. STM appearances of NO on Rh(111)

than for the calculated ones, although $\frac{\Delta}{d}$ is similar. The corrugation $d = 30$ pm is about half the corrugation of Fig. 4.6(a), which can be explained by the fact that the used tips are less sharp. When positioned over the center of the hexagon, the adsorbate does not reach all the way to the substrate rhodium atoms. Instead, the AOs of the tungsten atoms at the tip will start to overlap with the MOs of the molecules in the hexagons and thus contribute to the current when moving down in the hexagon.

The orbital analysis similar to Fig. 4.7 indicates that in this case, mainly the p_z orbital from the tip adsorbate contributes to the current. Next to having the largest PDOS at the Fermi energy, the p_z orbital reaches out furthest, so that the overlap with the MOs at the substrate will be largest. From the sample surface, however, several MOs contribute to the current. Here, interference effects between pathways from different surface MOs to the tip p_z orbital become important. In Table 4.1, the interference terms $\mathcal{I}^{\alpha\beta\alpha'\beta'}$ (equation (4.3.14)) for the W(110)-N tip over the NO_{fcc} are listed. On top of the hcp molecule, similar interference effects are found. The diagonal terms $\mathcal{I}^{\alpha\beta\alpha\beta}$ (gray shaded cells) represent the transmission from sample orbitals α to tip AOs β without interference. The off-diagonal elements show the interference of the pathway $(\alpha - \beta)$ with tunneling path $(\alpha' - \beta')$. As $\mathcal{I}^{\alpha\beta\alpha'\beta'} = \mathcal{I}^{\alpha'\beta'\alpha\beta}$, the lower left part of the table is the same as the upper right part. The last column of the table shows the total contribution for each pathway including interference, $\sum_{\alpha'\beta'} \mathcal{I}^{\alpha\beta\alpha'\beta'}$. To limit the size of the table, only pathways with $\sum_{\alpha'\beta'} \mathcal{I}^{\alpha\beta\alpha'\beta'} > 5\%$ are considered. Because of this, the sum of a row is usually not equal to the value of the last column, as it should be. Similarly, the sum of the last column, $\sum_{\alpha\beta\alpha'\beta'} \mathcal{I}^{\alpha\beta\alpha'\beta'}$ is not 100%.

By far, the largest contribution to the current comes from the $\sigma_{2p_z} - \text{N}p_z$ path: 395% of the total current without interference and 151% including interference. This large difference is mainly due to the $\sigma_{2s}^* - \text{N}p_z$ electron pathway that interferes destructively with $\sigma_{2p_z} - \text{N}p_z$ (see Fig. 4.1). Consequently, the $\sigma_{2s}^* - \text{N}p_z$ pathway has a negative total contribution to the current. For clarity, the rows of these negatively contributing pathways are shaded light gray. This kind of interference between different pathways involving different MOs of the same molecule has been observed before [37, 38, 39].

4. STM appearances of NO on Rh(111)

It is remarkable that σ_{2s}^* has such a strong contribution to the tunneling current while it has a low PDOS around the Fermi energy (see Fig. 4.2). However, as explained in equations (2.1.3) and (2.1.4), the tunneling current does not only depend on the PDOS of both tip and sample, but also on the overlap of the wave functions. Indeed, although the PDOS of σ_{2s}^* is lower than the PDOS of $\pi_{2p_{xy}}^*$, its wave function extends further in the z -direction and a larger overlap can be expected. These important current contributions of an MO far away from the Fermi energy have been observed before [38].

Note that not only pathways between closest atoms i.e. the apex N atom and the substrate NO molecule, have significant contributions. As opposed to tunneling via the MOs of the molecule, the "through molecule" trajectory, there are also important contributions from tunneling "through space". In the latter case, the electrons skip the molecule and directly tunnel to an AO of a Rh substrate atom. Interference effects between the through molecule and through space trajectories have been reported in literature before as well [40, 41].

The total current at the NO_{fcc} , including interference effects is smaller than without interference effects. This can be seen by adding up diagonal terms of the pathways that contribute positively to the total current (the diagonal cells in the light gray rows should be omitted). The obtained value of 415% should be compared to the 100% of the total current including interference effects.

Finally, the structure in Fig. 4.6(g) looks totally different from what might have been expected based on the positions of the molecules. The NO molecules adsorbed at the fcc and hcp site are not visible any more. Instead, bright dots form an equilateral triangle, indicated by the white circles of Fig. 4.6(g). By solely looking at the STM image, the $(2 \times 2) - 2\text{NO}$ structure might easily be misinterpreted as a more densely packed $0.75 \text{ ML } (2 \times 2) - 3\text{NO}$ structure with all the NO molecules adsorbed in the same type of site.

Theoretically, however, this kind of imaging could be reproduced when scanning the $(2 \times 2) - 2\text{NO}$ structure using the clean W(110) tip and the W(111)-NO flat tip (tip 4.5(a)), rotated clockwise around the x and y axis by 10° and 45° around the z axis as shown in Fig. 4.6(h) and 4.6(i). The rotation of the W(111)-NO flat tip is

4.4 Results and discussion

Table 4.2: The dominant interference terms $\mathcal{I}^{\alpha\beta\alpha'\beta'}$ and total contribution per pathway $\sum_{\alpha'\beta'} \mathcal{I}^{\alpha\beta\alpha'\beta'}$ of the $(2 \times 2) - 2\text{NO}$ sample MOs α and the $\text{W}(110)$ tip AOs β , taken at the midpoint between the fcc and hcp molecules of the SIESTA optimized surface structure. The values are in percentage of the total current. The gray shaded diagonal elements represent the current contributions of each trajectory excluding interference effects.

		$(\alpha' - \beta')$										$\sum_{\alpha'\beta'} \mathcal{I}^{\alpha\beta\alpha'\beta'}$
		fcc $\pi_{2p_x}^* - \text{Wd}_{r^2-z^2}$	hcp $\pi_{2p_x}^* - \text{Wd}_{r^2-z^2}$	fcc $\pi_{2p_x}^* - \text{Wp}_z$	fcc $\pi_{2p_x}^* - \text{Ws}$	hcp $\pi_{2p_x}^* - \text{Wp}_z$	hcp $\pi_{2p_x}^* - \text{Ws}$	fcc $\pi_{2p_y}^* - \text{Wd}_{r^2-z^2}$	fcc $\sigma_{2p_z} - \text{Wd}_{r^2-z^2}$	fcc $\sigma_{2p_z} - \text{Wp}_z$	fcc $\sigma_{2p_z} - \text{Ws}$	
$(\alpha - \beta)$	fcc $\pi_{2p_x}^* - \text{Wd}_{r^2-z^2}$	7	1	4	2	1	0	0	0	0	0	13
	hcp $\pi_{2p_x}^* - \text{Wd}_{r^2-z^2}$	1	5	1	0	3	1	1	-1	-1	0	11
	fcc $\pi_{2p_x}^* - \text{Wp}_z$	4	1	3	2	1	0	0	0	0	0	9
	fcc $\pi_{2p_x}^* - \text{Ws}$	2	0	2	3	0	1	0	0	0	0	8
	hcp $\pi_{2p_x}^* - \text{Wp}_z$	1	3	1	0	2	2	0	-1	-1	0	7
	hcp $\pi_{2p_x}^* - \text{Ws}$	0	1	0	1	2	2	0	0	0	-1	6
	fcc $\pi_{2p_y}^* - \text{Wd}_{r^2-z^2}$	0	1	0	0	0	0	3	0	0	0	6
	fcc $\sigma_{2p_z} - \text{Wd}_{r^2-z^2}$	0	-1	0	0	-1	0	0	5	4	2	6
	fcc $\sigma_{2p_z} - \text{Wp}_z$	0	-1	0	0	-1	0	0	4	4	3	6
	fcc $\sigma_{2p_z} - \text{Ws}$	0	0	0	0	0	-1	0	2	3	4	5

performed in order to move the NO molecule away from the tunnel junction, i.e. to scan with the tungsten atoms of the tip. Usually, the difference between the VASP and SIESTA optimized surface structures were marginal. Here, however, the bright dots only appear for the SIESTA optimized surfaces. In the VASP optimized structure, instead of bright dots at the corners of the triangles, the triangles appear bright as a whole at the position of the fcc molecule.

The orbital contributions on top of the fcc and hcp molecule are analogous to the ones for the $\text{W}(110)\text{-N}$ tip (Table 4.1): destructive interference between the paths from σ_{2p_z} and σ_{2s}^* at the surface to $\text{Wd}_{r^2-z^2}$, Wp_z and Ws at the tip.

When looking at the midpoint in between the molecules though, there are clear differences. Both tables 4.2 and 4.3 show the interference terms $\mathcal{I}^{\alpha\beta\alpha'\beta'}$ at the midpoint between the fcc and hcp molecule of the $\text{W}(110)$ and $\text{W}(110)\text{-N}$ tips, respectively. Probing in between the molecules, both of them contribute to the current and hence

4. STM appearances of NO on Rh(111)

Table 4.3: The dominant interference terms $\mathcal{I}^{\alpha\beta\alpha'\beta'}$ and total contribution per pathway $\sum_{\alpha'\beta'} \mathcal{I}^{\alpha\beta\alpha'\beta'}$ of the $(2 \times 2) - 2\text{NO}$ sample MOs α and the W(110)-N tip AOs β , taken at the midpoint between the fcc and hcp molecules. The values are in percentage of the total current. The gray shaded diagonal elements represent the current per trajectory excluding interference effects. The light gray shaded rows indicate the pathways that contribute negatively to the current due to destructive interference effects.

$(\alpha - \beta)$	$(\alpha' - \beta')$									$\sum_{\alpha'\beta'} \mathcal{I}^{\alpha\beta\alpha'\beta'}$
	fcc $\sigma_{2p_z}^* - \text{Np}_z$	fcc $\pi_{2p_x}^* - \text{Np}_z$	hcp $\pi_{2p_x}^* - \text{Np}_z$	fcc $\sigma_{2s}^* - \text{Np}_z$	hcp $\sigma_{2p_z}^* - \text{Np}_z$	fcc $\pi_{2p_y}^* - \text{Np}_z$	hcp $\pi_{2p_y}^* - \text{Np}_z$	hcp $\sigma_{2s}^* - \text{Np}_z$		
fcc $\sigma_{2p_z}^* - \text{Np}_z$	55	0	-4	-35	9	0	-2	-6	22	
fcc $\pi_{2p_x}^* - \text{Np}_z$	0	25	5	0	-4	0	3	3	22	
hcp $\pi_{2p_x}^* - \text{Np}_z$	-4	5	17	2	0	2	0	0	17	
fcc $\sigma_{2s}^* - \text{Np}_z$	-35	0	2	22	-6	0	1	4	-14	
hcp $\sigma_{2p_z}^* - \text{Np}_z$	9	-4	0	-6	32	-2	0	-20	12	
fcc $\pi_{2p_y}^* - \text{Np}_z$	0	0	2	0	-2	11	1	1	9	
hcp $\pi_{2p_y}^* - \text{Nd}_z$	-2	3	0	1	0	1	9	0	9	
hcp $\sigma_{2s}^* - \text{Np}_z$	-6	3	0	4	-20	1	0	13	-8	

the MOs are labeled according to their adsorption site: fcc or hcp.

In case of the W(110) tip (Table 4.2), the main current carrying orbital at the sample for both fcc and hcp molecules is $\pi_{2p_x}^*$. From the tip, the important orbitals are $\text{Wd}_{r^2-z^2}$, Wp_z and Ws . The orbitals σ_{2p_z} and σ_{2s}^* do not play a large role and hence, as opposed to the case when probing on top of a molecule, destructive interference effects between MOs from the same molecule are small. Interference effects between the MOs from different molecules are mainly constructive. Therefore, with more positive than negative interference, the total current at the midpoint including interference effects is larger than without interference (i.e. the sum of the diagonal elements is larger than the sum of the last column). Table 4.4 shows the current with and without interference effects taken into account evaluated at the fcc, hcp and midpoint position. In the last column, the ratio of these currents is shown, which is equal to the sum of the diagonal elements of the relevant interference table. If the percentage is larger than 100%, the total interference is destructive, if it is smaller, it is constructive. Having destructive interference effects on top of the molecules, but

Table 4.4: Total current (nA) with and without interference effects taken with the W(110) and W(110)-N tip over the fcc and hcp molecule and at the midpoint in between the molecules of the $(2 \times 2) - 2\text{NO}$ structure. The last column lists the ratio of the currents in percentage of the total current including interference.

	Position	with interference	without interference	Ratio
W(110)	fcc	0.16	0.20	125%
	hcp	0.12	0.14	117%
	midpoint	0.20	0.13	65%
W(110)-N	fcc	0.48	2.2	458%
	hcp	0.38	1.5	395%
	midpoint	0.39	0.79	203%

constructive interference effects in between the molecules, Table 4.4 shows that the midpoint gives the largest total current followed by the fcc and hcp sites. Hence, this is the position where the brightest spot will appear in the topographic image. Without interference effects, the midpoint has the lowest current. In that case, the bright spots in the image would have coincided with the NO molecules themselves.

For the W(110)-N tip, σ_{2p_z} and σ_{2s}^* have a much more prominent role, resulting in destructive interference effects at midpoint, see Table 4.3. Therefore, in this case, the total current without interference is larger than with interference (see Table 4.4). Overall, the current at midpoint is lower than at the fcc site and equal to the hcp site. Hence, bright spots appear at the fcc and hcp molecules and the region in between the molecules has the same apparent height as the hcp molecule itself. Without interference the order of importance of the current is barely changed.

As is shown, the importance of the σ_{2p_z} and σ_{2s}^* contribution to the current plays a crucial role in the type of imaging that is obtained. The interplay between the different orbitals, however, is subtle and it cannot be predicted on forehand what type of imaging will be obtained. For example when using the rotated W(111)-NO flat tip at the midpoint, σ_{2p_z} and σ_{2s}^* do still play an important role. Their negative contribution, however, is counteracted by a stronger constructive interference between the MOs from the fcc and hcp molecules, giving rise to the triangular appearance of Fig. 4.6(h). Without this compensating constructive interference, the W(111) tip,

4. STM appearances of NO on Rh(111)

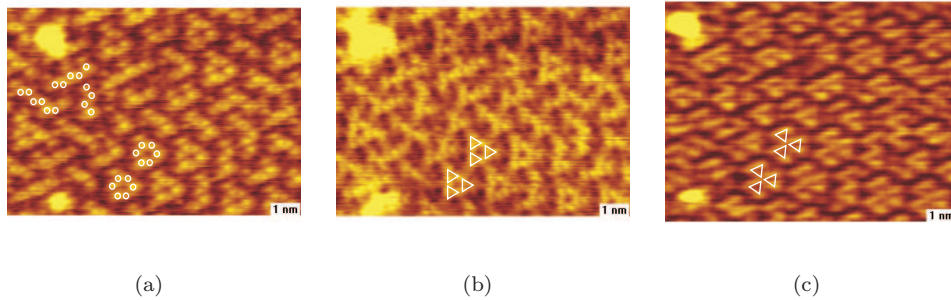


Figure 4.8: Three $10 \times 7 \text{ nm}^2$ images taken consecutively on the same position showing different appearances. The adlayer consists of a mixture of small grains of the $(2 \times 2) - 2\text{NO}$ and the $(4 \times 2) - 4\text{NO}$ structure. In (a), the real positions of the molecules are imaged, indicated by the white circles to guide the eye. In (b), the imaging is similar to Fig. 4.6(g), white triangles showing the triangular structure. In (c), the honeycombs have a flower-like appearance that was not found theoretically. Scan parameters: $V = 1 \text{ V}$, $I = 1.04 \text{ nA}$.

however, shows the molecules as bright spots with σ_{2p_z} and σ_{2s}^* playing the most crucial role on all three positions. Furthermore, as mentioned before, the SIESTA optimized structure does show the dots at the midpoint whereas the VASP optimized structure shows bright triangles at the position of the fcc molecules. This might be due to slight differences in the atomic positions. Alternatively, differences in the electronic properties could also play a role.

Changes between the different imaging sometimes occurred spontaneously during scanning. Fig. 4.8 shows three consecutive STM images taken on the same area, as can be seen from the bright contamination spots in the upper and lower left corner of each picture. After deposition, the NO molecules form small patches of the $(2 \times 2) - 2\text{NO}$ and the $(4 \times 2) - 4\text{NO}$ structure: only a few zigzags in case of the $(4 \times 2) - 4\text{NO}$ structure and single honeycombs for the $(2 \times 2) - 2\text{NO}$ structure. In Fig. 4.8(a), the individual molecules are imaged as single dots, indicated by white circles. In Fig. 4.8(b) the imaging of Fig. 4.6(g) is obtained and the triangular appearance of the fcc site is now indicated by white triangles. In Fig. 4.8(c) yet another, flower-like appearance of the honeycombs is observed. Still, the fcc site is imaged as triangles, but now they are individually rotated 30° with respect to the triangles of Fig. 4.8(b).

The transition between any three of the figures is completely reversible. An explanation could be that in all three images, an NO molecule was adsorbed at the tip. Scanning over the contamination might have such a strong interaction with the NO molecule that it changes its orientation/position on the tip and hence, the difference between Fig. 4.8(a) and (b) could be the difference between scanning with and without an NO terminated tip apex. The appearance of (c) was not found in our simulations. However, there are many more possibilities of the NO molecule to adsorb on the tip than modeled here.

4.4.2 $(4 \times 2) - 4\text{NO}$

In Fig. 4.9, a comparison between the experimental and theoretical appearance of the $(4 \times 2) - 4\text{NO}$ structure is made. The first column shows the experimentally found appearances, the second column shows the best theoretical match. For all images, the corrugation d is given and for the theoretically obtained images, the used tip is indicated.

The experimental image of Fig. 4.9(a) could be well reproduced theoretically using the W(111)-NO top tip (tip 4.5(b)), see Fig. 4.9(b). Not only the qualitative appearance, but also the corrugation matches closely. All tips with the NO molecule adsorbed upright at the apex give a similar kind of imaging. The current is mainly carried by $\pi_{2p_{xy}}^*$ of the molecules on the tip and on the sample, similar to the case for the $(2 \times 2) - 2\text{NO}$ structure, see Fig. 4.7. The corrugation of the $(4 \times 2) - 4\text{NO}$ structure, however, is only half the corrugation of the $(2 \times 2) - 2\text{NO}$ structure. This is due to the different ordering of the NO molecules in both structures. When probing away from a molecule, the current is determined by the amount of overlap of the MOs of the tip and sample molecules and, hence, by their mutual distance. This distance is largest when the tip is positioned in the middle of the hexagon of the $(2 \times 2) - 2\text{NO}$ structure. As discussed before, the overlap of the MOs is too small to reach the set-point current. Instead the NO at the apex moves down in the hexagon in search for extra overlap from the AOs of the rhodium substrate, giving rise to the large corrugation. For the $(4 \times 2) - 4\text{NO}$ structure, however, the distance between the molecules is smaller and the overlap between the MOs of the tip and sample bound molecules

4. STM appearances of NO on Rh(111)

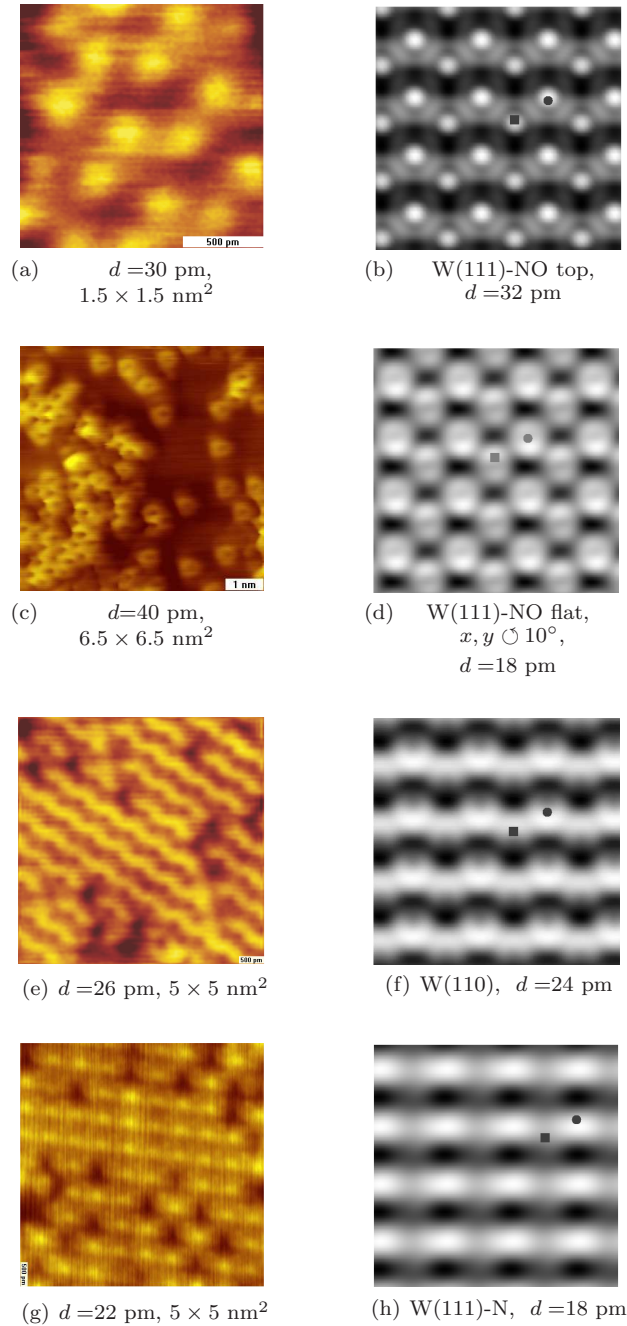


Figure 4.9: Four different appearances of the $(4 \times 2) - 4\text{NO}$ structure. In the first column, the experimental picture is shown. The second column shows the theoretical image that matches the experimental one closest. For each picture the corrugation d is given, for the theoretical pictures, the used tip is indicated. The molecules adsorbed in hcp and fcc sites, are indicated by the dark square and circle, respectively. The theoretical images are 2×2 nm² and are taken at $V=100$ mV and $I=0.500$ nA. All structures are optimized in VASP. The experimental parameters are: (a) $V=94$ mV, $I=0.35$ nA, (c) $V=221$ mV, $I=1.07$ nA, (e) $V=127$ mV, $I=0.422$ nA and (g) $V=90$ mV, $I=0.374$ nA.

completely govern the current.

In Fig. 4.9(c), the molecules are imaged as bright rings with a dip in the center. The picture mainly shows single molecules with a small area of the $(4 \times 2) - 4\text{NO}$ structure in the lower left corner. This image can be best reproduced when scanning with an N or O terminated tip. Alternatively, tips with an NO molecule adsorbed flat on the apex also give this kind of imaging. Similar to Fig. 4.6(e) and (f), mainly the apex adsorbate's p_z orbital contributes to the current. The corrugation of the experimental ($d = 40$ pm) and theoretical ($d = 18$ pm) images differs considerably. However, the imaging qualitatively looks the same.

According to the Tersoff-Hamann approximation (see section 2.1), the STM imaging is proportional to the LDOS of the surface. Therefore, the ring shape appearance of the molecules might be explained by the shape of the LDOS of the molecule's molecular orbitals, see Fig. 4.2. Indeed, being brightest at the center, σ_{2p_z} and σ_{2s}^* are the orbitals that mainly contribute to the current when evaluated right on top of the molecules. Away from the center on the other hand, $\pi_{2p_{xy}}^*$ is the main current carrying orbital. Now, analogous to the case described for the $(2 \times 2) - 2\text{NO}$ structure, $\pi_{2p_{xy}}^*$ does not show large interference effects whereas σ_{2p_z} and σ_{2s}^* interfere destructively. Therefore, at center of the molecule, instead of obscuring the dip by positive current contributions, it will only be enhanced due to the negative interference between σ_{2p_z} and σ_{2s}^* . The larger this interference effect is, the more pronounced the ring will appear. Although not as clear, the NO molecules in the $(2 \times 2) - 2\text{NO}$ structure of Fig. 4.6(f) also show a shallow dip on top of the molecule.

In order to be able to see any detail of the ring, the size of the orbital with which the ring is scanned, should not be larger than the size of the ring shaped orbital $\pi_{2p_{xy}}^*$. Having a low principle quantum number ($n = 2$), this condition is fulfilled for the s and p orbitals of the N and O atoms. The orbitals of the W atoms, however are too large to sharply image the rings. Consequently, for W apex atoms, the molecules appear as bright dots.

The imaging of Fig. 4.9(e) shows the zigzag pattern of the $(4 \times 2) - 4\text{NO}$ structure without resolving the individual molecules. Theoretically, this kind of appearance is obtained using W terminated tips. The image shown in Fig. 4.9(f) is scanned

4. STM appearances of NO on Rh(111)

using the W(110) tip. On top of the molecules, the main orbital contributions come from σ_{2p_z} , $\pi_{2p_x}^*$ and σ_{2s}^* . The negative interference between σ_{2s}^* and σ_{2p_z} is smaller than 10% of the total current which is canceled by a positive interference between $\sigma_{2p_z} - \text{W}d_{r^2-z^2}$ and $\sigma_{2p_z} - \text{W}p_z$. In between the molecules, all interference terms decrease. Overall, the current is approximately the same at the fcc, hcp and midpoint position. As a consequence, all positions are imaged equally bright and the individual molecules cannot clearly be resolved.

Finally, in Fig. 4.9(g) the $(4 \times 2) - 4\text{NO}$ structure appears as straight lines with bright dots. Fig. 4.9(h) which is obtained by the W(111)-N tip, closely resembles the experimental picture. The position of the straight lines coincides with the zigzag lines of the NO molecules in the $(4 \times 2) - 4\text{NO}$ structure, with the bright spots located at the position of the fcc molecule. A close inspection of the W(111)-N tip (Fig. 4.4(c)), however, reveals that the N atom is buried in between the tungsten atoms. Therefore, it does not contribute to the current. Instead, three W apex atoms surrounding the N atom do, all with approximately the same intensity. Furthermore, at each position on the substrate (fcc, hcp and midpoint) both NO molecules at the surface contribute to the current. Simultaneously imaging two molecules with three apex atoms is too complex to analyze. Despite its complexity, this appearance could be reproduced experimentally rather easily indicating that blunt tips typically give the line shape appearance of the $(4 \times 2) - 4\text{NO}$ structure.

4.5 Conclusion

In this chapter, the appearance of the $(2 \times 2) - 2\text{NO}$ and $(4 \times 2) - 4\text{NO}$ adlayer structures on a Rh(111) surface were studied in STM in relation to the functionalization of the tip. Different apex adsorbates give rise to a variety of possible manifestations of these structures. The theoretically calculated STM images match the experimental ones so closely that some hints about the apex configurations could be derived from a one-to-one comparison. The knowledge about the tip apex configuration does not only help to interpret the STM topographic images, it also paves the way for a better understanding of STM spectroscopy and STM-IETS in particular. Tips used in

the modeling have clean tungsten apices, apices with NO molecules adsorbed (both upright and flat) and N or O terminated tip ends.

The total tunneling current results from electrons taking different orbital pathways. The contribution of these pathways cannot just be added since, due to the wave-like nature of particles in quantum mechanics, different electron pathways give rise to interference effects. For tips with an NO molecule adsorbed upright at the apex, the interference effects are negligible. All the other tips show a similar kind of interference.

When positioned right over an adsorbed NO molecule on the surface, there is a strong destructive interference of electron trajectories that involve the σ_{2s}^* and the σ_{2p_z} orbitals of the molecule. Hence, the total current on top of a molecule including interference effects is lower than the current when the interference effects would be excluded. Although the σ_{2s}^* molecular orbital has a low PDOS at the Fermi energy, its participation to the tunneling current is high due to a large overlap with the orbitals of the tip. We would therefore like to stress that it is the combination of both PDOS and wave function overlap that determines an orbital's contribution to the tunneling current.

When the tip is positioned in between the molecules adsorbed at the fcc and hcp sites, the interplay between the different orbitals is so subtle that it cannot be predicted on forehand what type of imaging will be obtained. There is a balance between the importance of the destructive interference from the σ_{2s}^* and σ_{2p_z} orbitals of the same molecule and the mainly constructive interference from the MOs from the fcc and hcp molecules. For most of the tips used, the destructive interference is larger than the constructive so that the total current in between the molecules remains smaller than on top of a molecule. Hence the NO molecules appear as the bright spots in the image. However, when using some of the clean tungsten tips, the positive interference dominates the balance. This effect can be so large that the current in between the molecules is larger than on top of a molecule. As a result, bright spots in the STM image do not coincide with the positions of the NO molecules in the $(2 \times 2) - 2\text{NO}$ structure and hence, a higher density $(2 \times 2) - 3\text{NO}$ structure would be wrongly determined. This shows that care must be taken when

4. STM appearances of NO on Rh(111)

determining molecular adlayer structures solely by using the STM as it might lead to misinterpretation of the results.

References

- [1] R. M. Tromp, E. J. van Loenen, J. E. Demuth and N. D. Lang, ‘Tip electronic structure in scanning tunneling microscopy,’ *Phys. Rev. B*, **37**, 9042–9045 (1988).
- [2] D. M. Eigler, C. P. Lutz and W. E. Rudge, ‘An atomic switch realized with the scanning tunnelling microscope,’ *Nature*, **352**, 600–603 (1991).
- [3] T. Komeda, Y. Kim and M. Kawai, ‘Scanning tunneling microscopy observation of CO on Pd(110) at cryogenic temperature; imaging mechanism and novel one-dimensional array formation,’ *Jpn. J. Appl. Phys. Part 1*, **40**, 4403–4408 (2001).
- [4] F. Calleja, A. Arnau, J. J. Hinarejos, A. L. V. de Parga, W. A. Hofer, P. M. Echenique and R. Miranda, ‘Contrast reversal and shape changes of atomic adsorbates measured with scanning tunneling microscopy,’ *Phys. Rev. Lett.*, **92**, 206101 (2004).
- [5] L. Bartels, G. Meyer and K.-H. Rieder, ‘Controlled vertical manipulation of single CO molecules with the scanning tunneling microscope: a route to chemical contrast,’ *Appl. Phys. Lett.*, **71**, 213–215 (1997).
- [6] M. Schmid, H. Stadler and P. Varga, ‘Direct observation of surface chemical order by scanning tunneling microscopy,’ *Phys. Rev. Lett.*, **70**, 1441–1444 (1993).
- [7] L. Ruan, F. Besenbacher, I. Stensgaard and E. Laegsgaard, ‘Atom resolved discrimination of chemically different elements on metal surfaces,’ *Phys. Rev. Lett.*, **70**, 4079–4082 (1993).
- [8] L. Bartels, G. Meyer and K.-H. Rieder, ‘The evolution of CO adsorption on Cu(111) as studied with bare and CO-functionalized scanning tunneling tips,’ *Surf. Sci. Lett.*, **432**, L621–L626 (1999).

-
- [9] M. Tsukada, K. Kobayashi, N. Isshiki and H. Kageshima, ‘First-principles theory of scanning tunneling microscopy,’ *Surf. Sci. Rep.*, **13**, 265–304 (1991).
- [10] J. C. Dunphy, D. F. Ogletree, M. B. Salmeron, P. Sautet, M.-L. Bocquet and C. Joachim, ‘Tip dependent contrast in STM imaging of adsorbed sulfur layers: theory and experiment,’ *Ultramicroscopy*, **42-44**, 490–497 (1991).
- [11] C. Joachim, P. Sautet and P. Lagier, ‘The tip apex structure of the Eigler atomic switch,’ *Euro. Phys. Lett.*, **20**, 697–702 (1992).
- [12] B. J. McIntyre, P. Sautet, J. C. Dunphy, M. Salmeron and G. A. Somorjai, ‘STM tip-dependent image contrast of S/Pt(111) by controlled atom transfer,’ *J. Vac. Sci. Technol. B*, **12**, 1751–1753 (1994).
- [13] P. Sautet, J. C. Dunphy, D. F. Ogletree, C. Joachim and M. Salmeron, ‘Imaging a p(2x2) layer of sulfur on Re(0001) with the scanning tunneling microscope: an experimental and theoretical study of the effect of adsorption site and tip structure,’ *Surf. Sci.*, **315**, 127–142 (1994).
- [14] U. Landman, W. D. Luedtke, N. A. Burnham and R. J. Colton, ‘Atomistic mechanisms and dynamics of adhesion, nanoindentation, and fracture,’ *Science*, **248**, 454–461 (1990).
- [15] J. H. A. Hagelaar, E. Bitzek, C. F. J. Flipse and P. Gumbsch, ‘Atomistic simulations of the formation and destruction of nanoindentation contacts in tungsten,’ *Phys. Rev. B*, **73**, 045425 (2006).
- [16] H. J. Mamin, P. H. Guethner and D. Rugar, ‘Atomic emission from a gold scanning-tunneling-microscope tip,’ *Phys. Rev. Lett.*, **65**, 2418–2421 (1990).
- [17] I. W. Lyo and P. Avouris, ‘Field-induced nanometer- to atomic-scale manipulation of silicon surfaces with the STM,’ *Science*, **253**, 173–176 (1991).
- [18] R. Martel, P. Avouris and I. W. Lyo, ‘Molecularly adsorbed oxygen species on Si(111)-(7×7): STM-induced dissociative attachment studies,’ *Science*, **272**, 385–388 (1996).

4. STM appearances of NO on Rh(111)

- [19] J. Cerdá and F. Soria, ‘Accurate and transferable extended Hückel-type tight-binding parameters,’ *Phys. Rev. B*, **61**, 7965–7971 (2000).
- [20] J. Cerdá, M. A. V. Hove, P. Sautet and M. Salmeron, ‘Efficient method for the simulation of STM images. I. Generalized Green-function formalism,’ *Phys. Rev. B*, **56**, 15885–15899 (1997).
- [21] J. Cerdá, A. Yoon, M. A. V. Hove, P. Sautet, M. Salmeron and G. A. Somorjai, ‘Efficient method for the simulation of STM images. II. Application to clean Rh(111) and Rh(111)+c(4 × 2) – 2S,’ *Phys. Rev. B*, **56**, 15900–15918 (1997).
- [22] <http://www.icmm.csic.es/jcerda>.
- [23] M. P. L. Sancho, J. M. L. Sancho and J. Rubio, ‘Quick iterative scheme for the calculation of transfer matrices: application to Mo(100),’ *J. Phys. F*, **14**, 1205–1215 (1984).
- [24] M. C. Muñoz, V. R. Velasco and F. García-Moliner, ‘Tight binding models for non ideal semiconductor interfaces,’ *Prog. Surf. Sci.*, **26**, 117–133 (1987).
- [25] S. Datta, *Electronic transport in mesoscopic systems*, Cambridge University Press, Cambridge (1995).
- [26] M. Büttiker, Y. Imry, R. Landauer and S. Pinhas, ‘Generalized many-channel conductance formula with application to small rings,’ *Phys. Rev. B*, **31**, 6207–6215 (1985).
- [27] J. H. Ammeter, H.-B. Bürgi, J. C. Thibeault and R. Hoffmann, ‘Counter-intuitive orbital mixing in semi-empirical and ab initio molecular orbital calculations,’ *J. Am. Chem. Soc.*, **100**, 3686–3692 (1978).
- [28] The DFT calculations are performed by J. Cerdá, private communication.
- [29] G. Kresse and J. Furthmüller, ‘Efficiency of ab-initio total energy calculations for metals and semiconductors using a plane-wave basis set,’ *Comput. Mater. Sci.*, **6**, 15–20 (1996).

-
- [30] G. Kresse and J. Furthmüller, ‘Efficient iterative schemes for ab-initio total-energy calculations using a plane-wave basis set,’ *Phys. Rev. B*, **54**, 11169–11186 (1996).
- [31] G. Kresse and J. Hafner, ‘Norm-conserving and ultrasoft pseudopotentials for first-row and transition elements,’ *J. Phys.: Condens. Matter*, **6**, 8245–8257 (1994).
- [32] D. Sánchez-Portal, P. Ordejón, E. Artacho and J. M. Soler, ‘Projection of plane-wave calculations into atomic orbitals,’ *Solid State Commun.*, **95**, 685–690 (1995).
- [33] D. Sánchez-Portal, P. Ordejón, E. Artacho and J. M. Soler, ‘Density-functional method for very large systems with LCAO basis sets,’ *Int. J. Quantum Chem.*, **65**, 453–461 (1997).
- [34] P. Ordejón, E. Artacho and J. M. Soler, ‘Self-consistent order-N density-functional calculations for very large systems,’ *Phys. Rev. B*, **53**, R10441–R10444 (1997).
- [35] J. M. Soler, E. Artacho, J. D. Gale, A. García, J. Junquera, P. Ordejón and D. Sánchez-Portal, ‘The Siesta method for ab initio order-N materials simulation,’ *J. Phys.: Condens. Matter*, **14**, 2745–2779 (2002).
- [36] C. Popa, C. F. J. Flipse, A. P. J. Jansen, R. A. van Santen and P. Sautet, ‘NO structures adsorbed on Rh(111): theoretical approach to high-coverage STM images,’ *Phys. Rev. B*, **73**, 245408 (2006).
- [37] L. Jurczyszyn and B. Stankiewicz, ‘Inter-orbital interference in STM tip during electron tunneling in tip-sample system: influence on STM images,’ *Prog. Surf. Sci.*, **74**, 185–200 (2003).
- [38] P. Sautet and M.-L. Bocquet, ‘Shape of molecular adsorbates in STM images: A theoretical study of benzene on Pt(111),’ *Phys. Rev. B*, **53**, 4910–4925 (1996).

4. STM appearances of NO on Rh(111)

- [39] M.-L. Bocquet and P. Sautet, ‘STM and chemistry: a qualitative molecular orbital understanding of the image of CO on a Pt surface,’ *Surf. Sci.*, **360**, 128–136 (1996).
- [40] P. Sautet and C. Joachim, ‘Are electronic interference effects important for STM imaging of substrates and adsorbates? A theoretical analysis,’ *Ultramicroscopy*, **42-44**, 115–121 (1992).
- [41] E. N. J. A. Nieminen and K.-H. Rieder, ‘Interference between competing tunneling channels and chemical resolution of STM,’ *Surf. Sci.*, **552**, L47–L52 (2004).

Chapter 5

STM-IETS on NO on Rh(111)

5.1 Introduction

In this chapter, the NO on Rh(111) system is studied by inelastic electron tunneling spectroscopy (IETS) using the STM at 5 K (see section 2.2.2 for an explanation of IETS). The loss peaks observed in the IET spectra in the energy regime 20-500 meV are typically due to molecular vibrations. Generally in the gas phase, each atom in a molecule has 3 degrees of freedom - one for each translation along the x , y or z axis. Hence, a molecule with N atoms has $3N$ degrees of freedom. Collective movements of the atoms that do not alter the molecule's bond, however, are not related to vibrations. Non-linear molecules, for example, have three unique translational and rotational degrees of freedom, leaving $3N-6$ vibrational degrees of freedom. Linear molecules have $3N-5$ vibrational degrees of freedom: the rotation about the molecule's axis does not count, because it changes neither the positions of the atoms nor the angular momentum. When a molecule is adsorbed on a surface, however, the bond formed between the molecule and surface frustrates the translational and rotational motion of the molecule. The molecule's attempts to translate or rotate transform into vibrations of the molecule-substrate bond. Hence, a molecule adsorbed on a substrate has $3N$ vibrational modes.

For the diatomic NO molecule adsorbed on the Rh(111) surface, there are thus six vibrational modes: the molecule's internal N - O stretch, two hindered rotations

5. STM-IETS on NO on Rh(111)

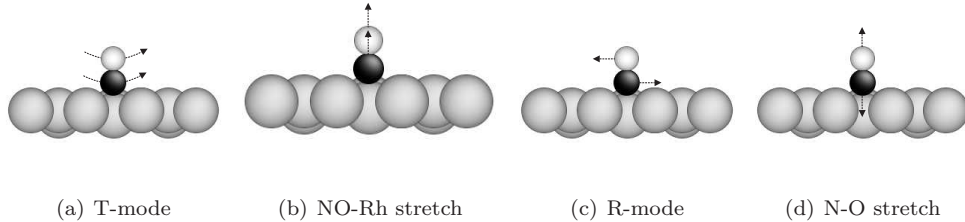


Figure 5.1: Schematic illustration of the possible vibrations of NO on Rh(111). There are two T-modes and two R-modes since the molecule can perform these vibrations in both lateral directions of the surface.

(R-modes) and three hindered translations (T-modes). The translational mode in which the molecule moves up and down on the substrate is usually called the NO - Rh stretch. Fig. 5.1 schematically shows the possible vibrations of NO on Rh(111). The exact value for the energy associated with each vibrational mode depends on the adsorption site of the molecule and the lateral interactions between the molecules, e.g. the coverage. In a HREELS study on this system [1], the Rh - NO stretch was observed at around 45 meV but the adsorption site and coverage were not indicated. The N - O stretch frequency was found to range from 184 meV to 204 meV for coverages between 0 ML and 0.68 ML. In a similar study [2], the Rh - NO stretch and N - O stretch in the $(4 \times 2) - 4\text{NO}$ structure (see Fig. 3.1) were reported to be 54 meV and 197 meV, respectively. The T-modes were determined by helium atom scattering and have values of 7.5 meV and 11.5 meV for the isolated NO molecules on the hcp and top sites, respectively [3]. No values for the R-modes have been reported so far. An overview of the vibrational energies for NO adsorbed in a hollow site is given in Table 5.1.

The NO on Rh(111) system has not been studied using STM-IETS before. However, the diatomic CO molecule which is also adsorbing upright to the sample surface has been studied rather extensively. It must be noted, however, that while both molecules interact with metal surfaces through the donation of electrons via their σ_{2p_z} orbital and a back donation from the metal to the $\pi_{2p_{xy}}^*$ orbital [4], the presence of an additional electron in the anti-bonding $\pi_{2p_{xy}}^*$ orbital (Fig. 1.1(b)) in NO could alter its IET behavior.

Table 5.1: Literature values for the vibrational energy of an NO molecule adsorbed in a hollow site on the Rh(111) surface in meV

Vibration	Energy	Reference
N-O stretch	184-204	[1], [2]
NO-Rh stretch	45, 54	[1], [2]
R-mode	unknown	–
T-mode	7.5	[3]

On the Cu(100), Cu(110) and Ag(110) surfaces, the frustrated translational mode of the CO molecule could not be detected [5], while on the Cu(111), it was observed with an intensity of $\frac{\Delta\sigma}{\sigma} = 15\%$ [6]. The frustrated rotation around $\hbar\omega = 35$ meV is seen in all studies with a rather high intensity of $\frac{\Delta\sigma}{\sigma} = 8 - 20\%$ [5, 6, 7]. The metal - CO stretch frequency around $\hbar\omega = 42$ meV seems to be inactive, while the molecule's internal stretch frequency has been reported to have low intensities of about $\frac{\Delta\sigma}{\sigma} = 1\%$ [5].

When adsorbed on the transition metal Pd(110) surface, the CO molecule hops over the surface when the C - O stretch frequency is excited [8]. In another study, in which a CO molecule is adsorbed to a single Pd atom on a NiAl(110) surface [9], the detectable vibrations were the frustrated rotation ($\frac{\Delta\sigma}{\sigma} = 6\%$) and the C - O stretch ($\frac{\Delta\sigma}{\sigma} = 1.5\%$). Although shifting in energy, the same vibrational modes are active, independent on the nature of the material the CO molecule is adsorbed to. So far, no general selection rules for the excitation of vibrational modes as in HREELS or infrared spectroscopy, have been defined.

In most STM-IETS studies, the dependence of the IET signal on the tip configuration is ignored, except for [10, 11]. In [10], the tip is actively modified by adsorbing different molecular species at the tip apex. It is shown that some vibrational modes, which are not observed by a bare tip, become visible when using the modified tip apex. In chapter 4 of this thesis, it was already shown that the appearance of molecules adsorbed on the surface strongly depends on the kind of tip the molecules are scanned with. Changing the tip apex will change the type of wave functions from both tip and

sample that carry the elastic tunneling current. Therefore, the inelastic current will probably also be influenced by the nature of the wave functions. In this chapter, the dependence of the tip-sample configuration on the measured IET signal is studied. The procedure followed is similar to the one of chapter 4: the tip is changed until a different appearance of the NO structures is obtained, after which an IET spectrum is recorded. From the type of imaging, the tip apex structure is determined and related to the observed loss peaks in the spectrum.

5.2 Results and discussion

5.2.1 Loss peaks coming from the molecules on the substrate

Fig. 5.2(a) shows an image of NO on Rh(111) at low coverage: parts of the surface show isolated single molecules. The measured height of such an isolated molecule is 18 pm. Other parts of the rhodium surface are covered by the $0.50 \text{ ML } (4 \times 2) - 4\text{NO}$ structure (cf. Fig. 3.1) with a corrugation $d = 15 \text{ pm}$. The molecules in this structure are individually resolved and equally bright. Comparing Fig. 5.2(a) to Fig. 4.9(a) and Fig. 4.9(b) that are taken with a tip apex on which an NO is adsorbed upright, the images qualitatively look the same, but the corrugation of the structure is only half of the expected corrugation. Notice, however, that the GREEN code of chapter 4 is only semi-quantitative so that perfect agreement between the corrugations cannot be expected. Tips with a flat lying NO or one of the molecule's constituent atoms typically image the adsorbates at the surface as bright rings (see Fig. 4.9(c) and (d)) and can therefore be ruled out. Although clean tungsten tips do image the molecules as bright dots, it was shown in Fig. 4.9(e) and Fig. 4.9(f) that they usually cannot resolve them individually. Hence, although the corrugation does not match, the image of Fig. 5.2(a) is probably taken using an apex with a vertically adsorbed NO attached to it (for example, see Fig. 4.5(b)).

The crosses in the image mark the spots where IET spectroscopy is performed: on top of an isolated NO molecule, on a bare spot on the Rh(111) substrate and on a molecule in the $(4 \times 2) - 4\text{NO}$ structure. In Fig. 5.2(b), the three corresponding IET

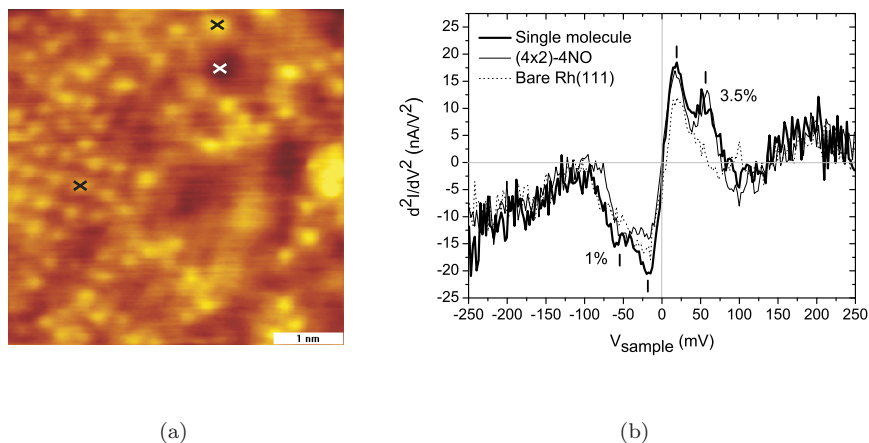


Figure 5.2: (a) Topographic STM image ($4.9 \times 4.9 \text{ nm}^2$) showing a mixture of isolated NO molecules and molecules arranged in the $(4 \times 2) - 4\text{NO}$ structure ($V = 100 \text{ mV}$, $I = 2 \text{ nA}$). The three crosses mark the spots where the IET spectra of (b) are recorded. (b) IET spectra measured on the spots marked by the crosses in (a). The dotted line is taken on the bare Rh(111) surface (white cross), the thick and thin full lines show the IET spectrum on top of an isolated molecule and on a molecule in the $(4 \times 2) - 4\text{NO}$ structure, respectively (black crosses). Anti-symmetric loss peaks show up at -57 meV and 56 meV with respective intensities $\frac{\Delta\sigma}{\sigma}$ of 1% and 3.5%. The IET spectra are averages of 4 curves of 1 minute each ($V_{ref,RMS} = 14 \text{ mV}$, $f = 4.7 \text{ kHz}$).

spectra are depicted. In order to separate the contribution of the NO molecule on the substrate from the background $\frac{d^2I}{dV^2}$ signal, anti-symmetric peaks in the spectrum taken on top of a molecule should not be present in the spectrum that is taken on the bare Rh(111) surface. This way, for both the isolated molecule as the molecule in the structure, a peak can be observed at around $+56 \text{ meV}$ and a dip at -57 meV , with an error of $\pm 2 \text{ meV}$. To guide the eye, the loss peaks in the spectra will be indicated throughout this chapter by a dash just above (below) the peak (dip). The full width at half maximum (FWHM) of the peaks is about 32 meV , which is in accordance to the calculated value of 33 meV following equation (2.2.4). The amplitude of the AC reference signal is almost solely responsible for this width. The intensities $\frac{\Delta\sigma}{\sigma}$ of the peaks at positive and negative bias voltage are 3.5% and 1%, respectively.

This asymmetry in intensity arises from the asymmetry in the tunnel junction (see

5. STM-IETS on NO on Rh(111)

Table 5.2: Vibrations of the NO molecule on the Rh(111) surface in meV [12]

		Single molecule	$(2 \times 2) - 2\text{NO}$	$(4 \times 2) - 4\text{NO}$
NO-Rh	stretch	-	-	43
		-	-	44
		-	49	45
		25	53	60
R-mode		-	49	53
		47	53	54
		47	58	56
		47	59	57
N-O	stretch	-	-	186
		-	-	187
		-	184	191
		187	198	197

section 2.2.2): when the molecule is adsorbed on the substrate and the sample voltage is positive, electrons from the tip will first tunnel over the vacuum gap before losing energy to the molecule. For negative sample biases, however, the electrons, now going from sample to tip, first scatter at the molecule after which they have to traverse the gap with a lower energy. Equation (2.1.1) shows that the tunnel probability is lower for electrons with lower energies and as a consequence, more electrons can tunnel inelastically at $V > 0$ than at $V < 0$.

In Table 5.2, the SIESTA calculated energies of some vibrational modes of an NO molecule on a Rh(111) substrate are given for an isolated molecule ¹ and a molecule in the $(2 \times 2) - 2\text{NO}$ and the $(4 \times 2) - 4\text{NO}$ structure [12]. Strictly speaking, the modes of the structures are not vibrations of single molecules but molecular phonon modes. The $(4 \times 2) - 4\text{NO}$ structure, for example, having four molecules in the unit cell, exhibits four different stretch modes, each with a different phase between the individual molecules. When going from the low coverage regime of the single molecule to the 0.50 ML coverage of the two structures, all the frequency modes increase in energy due to the lateral interactions between the molecules. Note that the frequency

¹The values for the isolated molecule were calculated from a 4×4 unit cell.

of the NO - Rh stretch mode doubles, whereas for the other modes it goes up by only 5-10 meV. Comparing Table 5.2 to Table 5.1, the experimentally obtained values for the Rh - NO stretch and the N - O stretch are similar to their theoretical counterparts.

Although possible to measure energy differences of about ~ 3 meV in our set-up, no difference could be detected between the loss peaks obtained on top of the isolated NO molecule and on the molecule in the structure. In [6], it was shown that, for an isolated CO molecule on Cu(111) and a molecule in a chevron structure, the IET peak for the R-mode shifted by less than 1 meV. It is not clear why the shift measured in STM-IETS is smaller than expected from vibrational calculations. A possible explanation could be the influence of the probing tip that is located closely above the molecule. Nevertheless, even though the vibrational shifts are not as large as anticipated on, it should still be possible to detect the shift of the NO - Rh stretch mode. The fact that no shift is observed together with the fact that in all other IETS studies the CO - metal stretch mode is found to be inactive leads us to attribute the obtained 55 meV feature of Fig. 5.2(b) to the R-mode of the NO molecule on the rhodium surface.

At smaller bias voltages, another pair of anti-symmetric peaks can be observed at around ± 15 meV. Although not so intense, the peaks are also visible in the spectrum taken on the bare Rh(111). This is due to the fact that in IETS not only vibrations of a molecule adsorbed in the tunnel junction can be excited but also phonons of the tip and sample electrodes themselves [13] that have energies typically in the region $\lesssim 20$ meV [14, 15]. Although the intensity of the peaks is higher on top of the molecule, their assignment to the T-mode at $\hbar\omega \sim 8$ meV is complicated due to two factors. First, the separation between the peaks at positive and negative bias is comparable to the width of the peaks. As a result, the resolution is too low to accurately determine the peak position. Additionally, as was shown in chapter 4, different electron trajectories will dominate the current when probing on top of the molecule or on the bare surface. Consequently, the coupling to the phonons could change, implying that the higher peak intensity of the spectrum taken on top of the molecule does not necessarily arise from the excitation of the T-mode. Although the first issue could be solved by using a smaller reference amplitude to reduce the line

5. STM-IETS on NO on Rh(111)

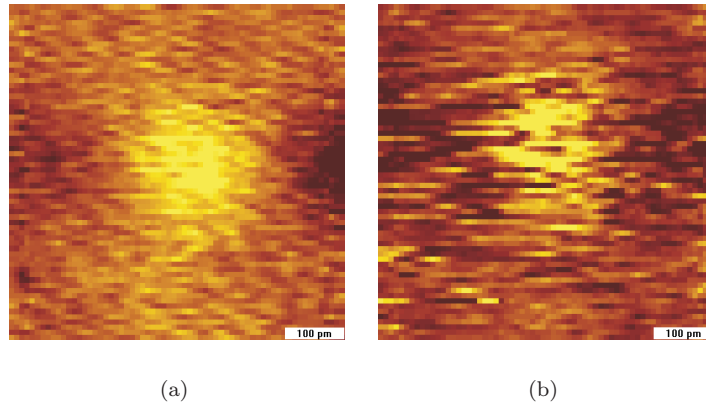


Figure 5.3: (a) A 64×64 pixel topographic STM image ($0.6 \times 0.6 \text{ nm}^2$) showing an isolated NO molecule on the surface ($V = 55 \text{ mV}$, $I = 2.1 \text{ nA}$). (b) The $\frac{d^2I}{dV^2}$ signal recorded simultaneously with the topographic image of (a). Since at $V = 55 \text{ mV}$ the molecular vibration is excited, the $\frac{d^2I}{dV^2}$ signal on top of the molecule is higher than on the bare Rh(111), see Fig. 5.2(b) ($V_{ref,RMS} = 14 \text{ mV}$, $f = 4.7 \text{ kHz}$ and dwell time is 270 ms per pixel).

width of the loss peaks (equation (2.2.4)), the interplay between tip and substrate phonons on one side and the molecule's T-mode on the other cannot be disentangled without proper theoretical support.

It is remarkable that although this interesting zero bias feature can be found in all IETS experiments, it is never explicitly mentioned, except for [6], in which it is fully ascribed to a molecular vibration. In fact, to our knowledge the work of [13] is the only systematic study of the phonon contributions from the electrode to the IET signal².

Fig. 5.3 shows two images of a zoom on a single NO molecule of Fig. 5.2(a). Both images are taken at a bias voltage of $V = 55 \text{ meV}$, i.e. tuned to the energy of the vibration. Together with the topographic signal of Fig. 5.3(a), the $\frac{d^2I}{dV^2}$ signal is recorded and shown in Fig. 5.3(b). Although in the topography the molecule is visible at in principle any voltage, in the vibrational image it disappears when taken at a bias voltage away from the threshold of the molecular vibration. This way, the STM

²As the phonon modes of graphite are also observed at higher energies [16], this study is not taken into account.

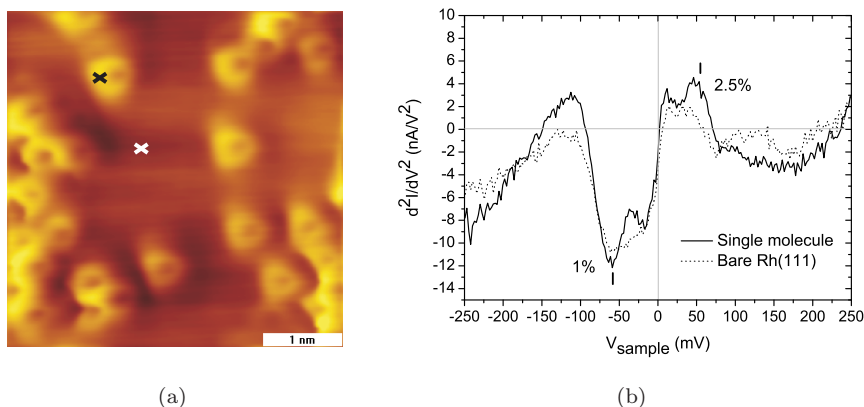


Figure 5.4: (a) Topographic STM image ($4.3 \times 4.3 \text{ nm}^2$) showing isolated NO molecules on the surface ($V = 99 \text{ mV}$, $I = 0.36 \text{ nA}$). The two crosses in the image mark the spots where the IET spectra of (b) are taken. (b) IET spectra measured on the spots marked by a cross in (a). The dotted line is taken on the bare Rh(111) surface (white cross), the full line shows the IET spectrum on the single molecule (black cross). Antisymmetric loss peaks are observed at $\pm 55 \text{ meV}$ with intensities $\frac{\Delta\sigma}{\sigma}$ of 1% and 2.5% for negative and positive sample bias, respectively. The IET spectra are averages of 23 curves of 1 minute each ($V_{ref,RMS} = 14 \text{ mV}$, $f = 4.7 \text{ kHz}$).

can be turned into a chemical sensitive microscope because each molecule has its own specific vibrations to which the bias voltage can be tuned [17].

Fig. 5.4(a) shows an image that is taken after changing the tip apex. Just as Fig. 5.2(a), it again shows a mixture of isolated molecules and the $(4 \times 2) - 4\text{NO}$ structure, but the molecules now appear as bright rings with a depression in the middle. The height of an isolated molecule is 50 pm and the corrugation of the structure is 35 pm . This appearance is very similar to the appearance of Fig. 4.9(c), where the main contribution from the tip to the tunneling current is through the p_z orbital of an adsorbate at the apex. Therefore, the tip apex is probably terminated by an N or O atom or a flat lying NO molecule (Fig. 4.4 and 4.5).

Analogously to Fig. 5.2, the crosses in Fig. 5.4(a) mark the spots where the IET spectra of Fig. 5.4(b) are taken. This time, the spectra are taken only on an isolated molecule and on the bare Rh(111), not on the structure. As opposed to Fig. 5.2(b), the

5. STM-IETS on NO on Rh(111)

intensity of the low energy feature ($|V| < 20$ meV) is the same on top of the molecule as on the bare rhodium, making it even more difficult to attribute this feature to the molecule's T-mode. Again a peak and dip are observed at +54 meV and -56 meV, respectively. Their intensities are $\frac{\Delta\sigma}{\sigma} = 1\%$ for negative and $\frac{\Delta\sigma}{\sigma} = 2.5\%$ for positive sample voltage and are thus lower than the intensities of the spectra of Fig. 5.2(b). Since the electronic properties of the single molecules on the surface are similar in both cases, the intensity difference must be due to a change in the tip configuration and hence, the coupling between tip and sample. Only proper modeling of the tunnel junction as is done in the previous chapter, but now including electron loss processes, could shed more light on the exact parameters responsible for the IET intensities.

In Fig. 5.5(a), a topographic image is shown in which the molecules appear similar to the ones of Fig. 5.4(a). Again, the ring-like shape is an indication that the image is taken with an adsorbate's p_z orbital. However, the height of a single molecule is lower (35 pm) and the depression in the middle of the rings is not as clear, indicating small differences in the exact configuration of the tunnel junction as compared to Fig. 5.4(a). The IET spectra of Fig. 5.5(b), however, look completely different from Fig. 5.4(b). The low bias feature around 15 meV comes up very strong on top of the molecule. Here, it has a dip at positive bias voltages whereas the spectra of Fig. 5.2(b) and 5.4(b) exhibit a peak. As explained in section 2.2.2, the observation of a dip at positive sample voltages is ascribed to second order electron processes that become important when the electronic levels with large electron-phonon coupling are close to resonance. This shows again that, as these features are a mix of molecular vibrations and phonons, the flipping from peak to dip needs be thoroughly studied for proper understanding.

Furthermore, the IET spectra in Fig. 5.5(b) do not show any loss peaks around ± 55 meV. From Fig. 5.5, it becomes surprisingly clear that a small change in imaging of the tip may lead to large changes in the IET spectra. In fact, for most tips, only the low bias feature could be observed without any clear peak in the rest of the spectrum.

In order to gain more understanding of the activity of the 55 meV peak, the results of Fig. 5.2, Fig. 5.4 and Fig. 5.5 are summarized in Table 5.3. In the second column, the apex configuration is indicated with which the image is most probably scanned

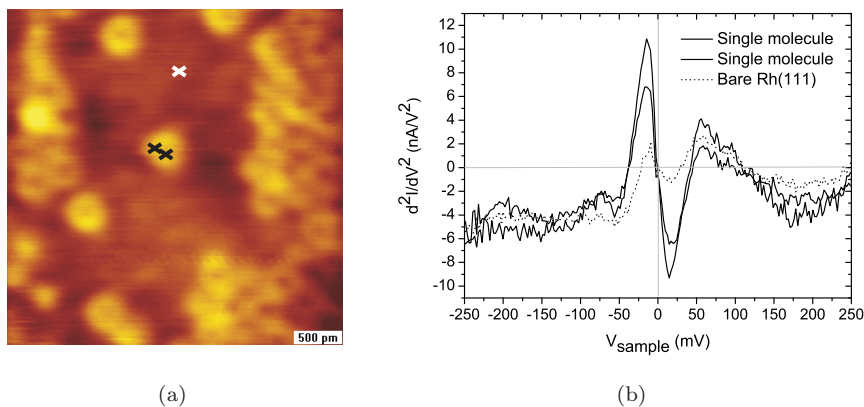


Figure 5.5: (a) Topographic STM image ($3.5 \times 3.5 \text{ nm}^2$) showing isolated NO molecules on the surface ($V = 102 \text{ mV}$, $I = 0.41 \text{ nA}$). The crosses in the image mark the spots where the IET spectra of (b) are taken. (b) IET spectra measured on the spots marked by a cross in (a). The dotted line is taken on the bare Rh(111) surface (white cross), the full lines show the IET spectra on the single molecule (black crosses).

(for the configurations, see Fig. 4.5). The third column gives an overview of the intensity of the loss peak at $+55 \text{ meV}$ and the last column indicates the molecular orbital of the NO molecule on the substrate that is mainly carrying the tunneling current. These orbitals are derived from the data obtained in chapter 4. For an apex with an NO molecule standing upright, the current is almost completely going via the $\pi_{2p_{xy}}^*$ orbital, as is shown in Fig. 4.7. Having a ring-like shape, from Fig. 4.2 it is clear that this orbital also dominates the current in Fig. 5.4(a) and Fig. 5.5(a). However, although being imaged with the same type of tip, the center of the rings in Fig. 5.5(a) does not appear as deep as in Fig. 5.4(a). This implies that there also is a contribution from an orbital with high LDOS along the axis of the molecule, i.e. a σ orbital. From all the σ orbitals of the molecule, this most probably is σ_{2p_z} as it has the highest PDOS at the Fermi energy (see Fig. 4.2).

From Table 5.3, it seems that there is a tendency for the R-mode to be active when the $\pi_{2p_{xy}}^*$ is the main current carrying orbital. Apparently, the electron-phonon coupling between this MO and the molecule's frustrated rotation is strong. This rela-

5. STM-IETS on NO on Rh(111)

Table 5.3: Summary of the results of the IETS experiments.

Figure	Most probable tip configuration	Intensity of the +55 meV loss peak	Main current carrying MO of surface adsorbed NO
5.2(b)	NO upright	3.5%	$\pi_{2p_{xy}}^*$
5.4(b)	flat NO	2.5%	$\pi_{2p_{xy}}^*$
5.5(b)	flat NO	—	$\pi_{2p_{xy}}^*$ and σ_{2p_z}

tionship is tentatively attributed to the similarity between the shape of the orbital's wave function and the movement of the nuclei when the R-mode is excited. This is schematically shown in Fig. 5.6(a). The lobed figure represents the wave function of the $\pi_{2p_{xy}}^*$ orbital. The gray shaded areas have a different phase³ than the white lobes and give the wave function the same symmetry as the movement of the atoms in the frustrated rotational mode that is indicated by the arrows in the same figure.

This intuitive symmetry based relationship does not only explain the observation of the R-mode, it can also explain why the internal and external molecular stretch modes are not observed. Following the same reasoning, these axial symmetric vibrational modes should couple to the axial symmetric σ orbitals, as is shown in Fig. 5.6(b). However, as the σ orbitals barely contribute to the current, the intensity of these vibrations will be very low and can therefore not be detected. In the case of Fig. 5.5(b), where no loss peaks could be observed at all in the IET spectrum, it was assumed, based on the shallow dip in the rings, that both the $\pi_{2p_{xy}}^*$ and the σ_{2p_z} orbital contributed to the current. As a result, although the vibrations connected to either molecular orbital can be excited, their intensity is probably too small to be detectable in our set-up.

Generally, when two or more orbitals contribute to the current, interference effects between the different inelastic electron pathways could have a large impact on the IET signal, just as the interference between elastic pathways can completely change the appearance of a structure. For example, when two MOs couple to a vibrational mode, negative interference between electron pathways via these orbitals could make

³Note that Fig. 5.6 represents a wave function that has a phase, whereas the molecular orbitals shown in Fig. 4.2 are plots of the LDOS obtained from the square of the wave function.

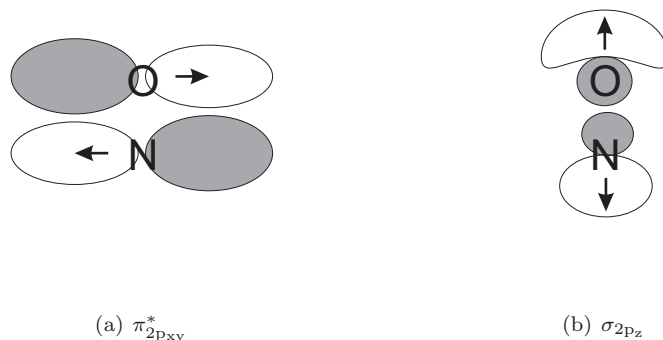


Figure 5.6: Side view of the NO molecule. The atoms are denoted by their chemical symbol and the lobed cartoons symbolize the molecular orbitals. Areas with similar phase have the same color. The arrows symbolize the movement of the nuclei according to the symmetry of the wave function. In (a) this movement is according to the R-mode of the molecule (see Fig. 5.1(c)) and in (b) it can either be the N - O stretch (Fig. 5.1(b)) or the metal - NO stretch (Fig. 5.1(d)).

the intensity of the mode undetectable. Constructive interference effects on the other hand, could enhance the IET signal. In chapter 4 it was already shown that subtle differences in the contributing molecular orbitals could have large implications for the interference effects. Clearly, these differences cannot be predicted based on intuitive models. Instead, they have to be derived from models like the GREEN model of chapter 4 in which inelastic processes need to be included.

Next to using the symmetry arguments for explaining the active vibrations in IETS, the symmetry of the molecular orbital and the vibrational mode can also be used to explain the symmetry of the vibrational image of Fig. 5.3(b). According to [18], the symmetry of the IET image is determined by the symmetry characters of the vibration and deformation potential at the Fermi energy. Seen from top, both the $\pi_{2p_{xy}}^*$ and the R-mode are anti-symmetric. As a result, the vibrational image is expected to be symmetric, which is confirmed by Fig. 5.3(b).

As indicated in Table 5.3, all the tips that were used in the IETS experiment were assumed to be contaminated by an NO molecule. Hence, an electron might also be expected to excite a vibrational mode of the molecule at the tip. However,

5. STM-IETS on NO on Rh(111)

when probing on the bare substrate, no loss peaks could be observed. This effect is especially strange for the NO molecule standing upright at the apex. After all, when this tip is positioned over the molecule at the sample, the current is carried solely by the $\pi_{2p_{xy}}^*$ of both tip and sample molecules. Based on the tentative selection rule, both molecules should contribute to the inelastic signal. The reason of seeing no peaks when positioned over the bare substrate could be explained by a change in tip-sample coupling. The importance of the tip molecule's $\pi_{2p_{xy}}^*$ orbital in the tunnel current has to decrease significantly when moving the tip from the sample bound molecule to the bare substrate. As a result, multiple MOs from the tip molecule could couple to the bare substrate so that all possible IET processes are too weak to be detectable. This argument is actually similar to the reason why no loss peaks could be observed in Fig. 5.5(b), but now with the molecule adsorbed at the other electrode. In the next section cases are discussed in which the IET signal can be proven to come from an adsorbate at the tip.

5.2.2 Loss peaks coming from a tip adsorbate

As shown before, the appearance of an imaged structure gives a strong indication about an adsorbate being present at the tip. When having an NO molecule at the apex, under the right conditions, loss peaks should be visible in the IET spectrum. There are two criteria to distinguish between loss peaks coming from the tip or the sample surface. First, when adsorbed at the tip apex, peaks should be visible at any spot on the surface, also on the bare substrate. Secondly, as the molecule is expected to adsorb differently on the tip apex than on the sample surface, the molecule's vibrational energies will shift. This can be detected in IETS by the observation of loss peaks that do not match the values of Table 5.1 and Table 5.2.

In this section, the loss peaks that come from the tip are discussed. As far as we know, this is the first time IET signals originating from an adsorbate at the tip are studied. In the first part of this section, a tungsten tip is used to study the NO on Rh(111) system. The apex of the tip to which the NO molecule binds consists of either tungsten or rhodium atoms that could have been transferred from sample to tip by the dipping procedure described in section 2.3.3. For comparison, the same

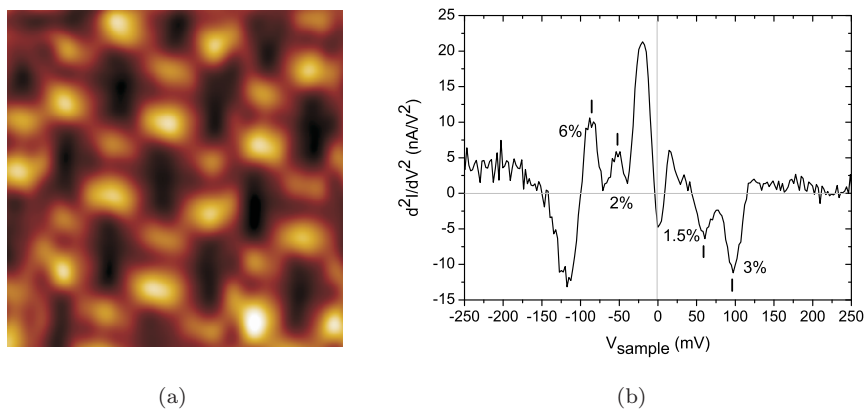


Figure 5.7: STM image ($2 \times 2 \text{ nm}^2$) of the $(2 \times 2) - 2\text{NO}$ structure. (b) The IET spectrum has peaks at -89 meV , -55 meV , $+58 \text{ meV}$ and $+97 \text{ meV}$. The respective peak intensities $\frac{\Delta\sigma}{\sigma}$ are 6%, 2%, 1.5% and 3%. The spectrum is an average of 18 curves of 75 s per curve, taken on different spots on the surface. ($V_{\text{ref,RMS}} = 14 \text{ mV}$, $f = 810 \text{ Hz}$).

experiment is performed with a tungsten tip on a $\text{Ag}(100)$ sample and the results are shown in the second part of this section. In this experiment, the tungsten tip is repeatedly dipped in the substrate to ensure the apex to be silver terminated prior to NO exposure.

Transition metal tip apex

In Fig. 5.7(a), an STM image showing the $(2 \times 2) - 2\text{NO}$ structure (see Fig. 3.4) is depicted. As opposed to the previous topographic pictures, the structure fully covers the surface. Comparing the appearance of the structure to Fig. 4.6(d), this type of imaging is typically obtained when the main current contribution of the tip is through an adsorbate's p_z orbital. In Fig. 5.7(b) the IET spectrum that is taken on the structure of Fig. 5.7(a) is shown. Note that this graph is an average of 18 spectra taken on different spots of the surface, i.e. on top of a molecule but also in the middle of the hexagon. The averaging is justified by the fact that the spectra that are taken at different locations all show peaks at the same position, which is an indication that the signal is coming from the adsorbate at the tip.

5. STM-IETS on NO on Rh(111)

Table 5.4: SIESTA calculated vibration energies of the NO terminated tips of Fig. 4.5 in meV [12]

Tip	W(111)-NO flat	W(111)-NO top	W(111)-NO flat fcc	W(111)-NO top fcc	W(111)-NO 3fold fcc
Figure	4.5(a)	4.5(b)	4.5(c)	4.5(d)	4.5(e)
R-mode	45	29	40	33	38
R-mode	52	30	66	33	38
NO-W stretch	56	69	59	64	49
N-O stretch	115	200	109	204	169

Although, the dip in the spectrum at about $V = -120$ meV is not understood, it cannot be related to IET processes because no peak at $V = +120$ meV is observed. Nevertheless, two pairs of anti-symmetric peaks are found with positions at -89 meV, -55 meV, $+58$ meV and $+97$ meV. Their respective peak intensities $\frac{\Delta\sigma}{\sigma}$ are 6%, 2%, 1.5% and 3%. Although the peaks at about ± 57 meV can be matched to the vibrational energy of an NO molecule on the substrate (Table 5.1 and Table 5.2), the peak at about ± 95 meV cannot. Therefore, the energies must be associated with the vibrational modes of a foreign species adsorbed at the tip apex. As these values do not match the vibrations of oxygen or nitrogen atoms on tungsten either [19, 20], frequency calculations have been performed [12] in SIESTA for the NO terminated tips of Fig. 4.5, and the resulting values of the molecular vibrations are shown in Table 5.4.

The numbers in the first row of the table refer to the pictures of the tip configurations of Fig. 4.5. When an NO molecule is adsorbed upright on top of an apex atom (third and fifth column), the vibrational energies do not depend on the tip crystallographic structure being FCC or BCC. When adsorbed vertically in a threefold hollow site (column six), however, the energies of the modes change. The downshift of the N - O stretch frequency suggests a weakening of the N - O bond. When adsorbed flat at the tip apex (columns two and four), the shifts are larger and the N - O bond is even further weakened. Finally, comparing the values for an NO molecule standing upright at the tip with the values of the NO that is bound to the rhodium surface (Table 5.1 and Table 5.2), the most remarkable difference is the change of order between

the frustrated rotation and the metal - NO stretch.

From all the values shown in Table 5.4, the N - O stretch for a flat lying molecule gives the best match for the peak observed at ± 95 meV. The small difference between the experimental and theoretical values might be due the fact that the tip apex is contaminated by rhodium atoms due to the dipping procedure. Alternatively, although lying flat at the apex, a slightly different adsorption geometry could also shift the energy of the vibration. Overall, not only from the fact that the experimentally obtained vibrational energies match the calculated ones reasonably well, but also based on the position-independency of the IET signal and the appearance of the $(2 \times 2) - 2\text{NO}$ structure, it can be concluded that the IET signal is coming from an NO molecule lying flat at the tip apex.

It is, however, not straightforward to assign the peak at about ± 57 meV because the 'substrate-spectra' of Figs. 5.2 and 5.4 also show a loss peak around this value. Hence, at this energy it is difficult to determine whether the signal is coming from the tip or from the substrate. A big difference between the substrate-spectra and the tip-spectrum of Fig. 5.7(b) is that the latter shows dips instead of peaks at positive sample bias. If the signal would have come from the sample, a peak would have been expected. Therefore, this dip is assigned to a vibrational mode coming from the tip: either the R-mode or the NO - W stretch of the flat lying molecule (Table 5.4), which are too close in energy to be resolved in the experiment. Note, however, that the intensity of the dip might have been reduced by the 55 meV peak coming from the molecules on the substrate.

In literature, the appearance of the loss feature (peak or dip) is explained by the position of the molecule's energy level with respect to the Fermi energy, as is explained in section 2.2.2 and Fig. 2.4. Indeed, as is shown in the PDOS picture of Fig. 5.8(a), all MOs of the molecule that contribute to the current have states close to the Fermi energy, whereas for the sample bound molecule it is only the $\pi_{2p_{xy}}^*$ orbital ⁴ (see Fig. 4.2). However, this hand-waving argument has to be verified theoretically.

⁴Note that also the NO molecule that is vertically adsorbed at the apex has multiple MOs with states at the Fermi energy, see Fig. 4.7(b). For this tip, however, the $\pi_{2p_{xy}}^*$ was the only orbital contributing to the current and it therefore looks more like the case of the NO molecule adsorbed at the surface.

5. STM-IETS on NO on Rh(111)

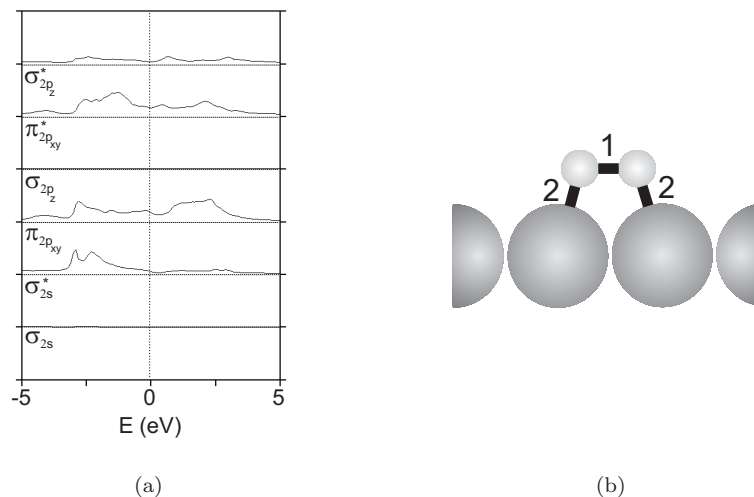


Figure 5.8: (a) Graph showing the PDOS of an NO molecule lying flat at the apex of the BCC tip, see Fig. 4.5(a). The curves are shifted upwards with respect to each other for clarity. The horizontal line at each curve represents the line of zero DOS. (b) Schematic representation of the adsorption of O₂ on Ag(110). The large gray circles symbolize the Ag(110) surface and the smaller white circles denote O atoms. There are two types of bonds: the bond labeled as 1 is the intramolecular O - O bond whereas the bond indicated by 2 is a Ag - O bond.

In order to explain the observed vibrations using the selection rule explained in Fig 5.6, we have to look at the MOs of the molecule that mainly carry the current. However, as there are several contributing orbitals (σ_{2s} , σ_{2s}^* , σ_{2p_z} and $\pi_{2p_{xy}}^*$, see chapter 4) that show large interference effects among each other, this case is too complex to understand using the intuitive approach and detailed theoretical calculations should be performed.

In a comparable IETS study in which an O₂ molecule is adsorbed flat on a Ag(110) sample [21], the only observable vibrational modes were the O - O stretch and the antisymmetric Ag - O₂ stretch. Not only the vibrational modes themselves but also their observation as dips at positive sample voltages is akin to the spectrum of Fig. 5.7(b). In [21], it could be derived from the imaging of the molecule, that almost all the tunneling current was mediated by the oxygen's $\pi_{2p_{xy}}$ orbital. This simplification compared to the multiple MOs contributing from the flat tip adsorbed NO molecule, allows us to test our selection rule. Since the $\pi_{2p_{xy}}$ is symmetrical along the axis of

the molecule, it correctly predicts the O - O stretch to be active and the frustrated rotational mode to be inactive in IETS. Yet, it fails to predict the activity of the observed antisymmetric Ag - O₂ stretch. The bonding geometry of the O₂ molecule on the Ag(110) substrate is schematically depicted in Fig. 5.8(b). As both atoms of the molecule have a bond to the substrate silver atoms, it could be argued that this vibrational mode is more related to the local excitation of the Ag - O bond (type 2) rather than the O - O bond (type 1). Therefore, for proper application of the selection rule, the symmetry of the contributing Ag - O bond orbital should be considered instead of the symmetry of the MO of the oxygen molecule.

The peaks in the spectrum of Fig. 5.7(b) at negative bias are more intense than the dips at positive bias, in accordance with the fact that the molecule is adsorbed at the tip apex (section 2.2.2). Next to the intensity difference, there is also a clear difference between the positive and negative value of the peak positions. The difference is largest for the N - O stretch frequency at +97 meV and -89 meV. When the IET signal is coming from molecules adsorbed at the sample, the shift is negligibly small. This clear distinction suggests that the Stark effect could be the responsible mechanism behind this shift: at the highly curved tip apex the electric field could be much larger than at the flat sample surface. For NO on Rh(111), the frequency shift as a function of the electric field is $\frac{d\nu}{dE} \approx 20 \text{ meV } \text{\AA}V^{-1}$ [22]. Assuming planar electrodes gives a reasonable estimation of the electric field at the sample surface. Using a potential difference between the peaks of about 0.2 V and 5 Å tip-sample separation, the frequency shift is only 0.8 meV. Indeed, this small shift is barely detectable. As opposed to the surface, the field at the tip depends on the shape of the apex and could be as much as 10 times larger than the field at the surface [23], which gives rise to the observed shift of 8 meV. It should be noted however, that in [5], the peak shift of the frustrated rotational mode of CO adsorbed on copper surfaces could not be fully accounted for by the Stark effect.

Fig. 5.9 shows a similar kind of imaging as in Fig. 5.7(a): the molecules adsorbed at the fcc site appear much brighter than the ones adsorbed at the hcp site. The accompanying IET spectrum shown in Fig. 5.9(b) is again taken on different spots of the structure. This time a dip is visible at +113 meV and a peak at -106 meV.

5. STM-IETS on NO on Rh(111)

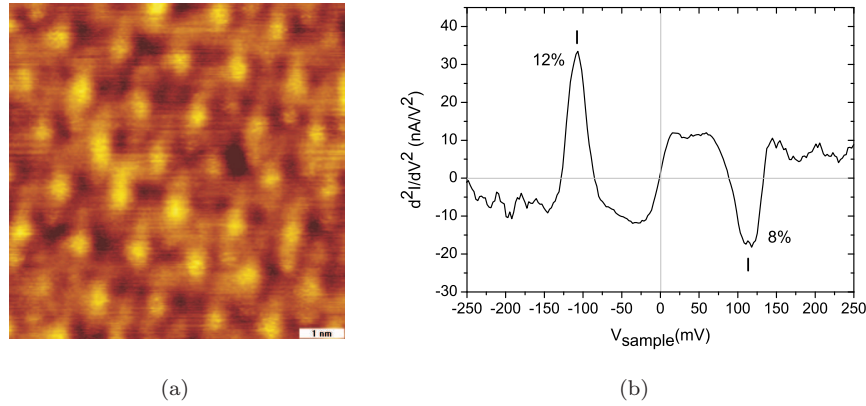


Figure 5.9: STM image ($7.5 \times 7.5 \text{ nm}^2$) of the $(2 \times 2) - 2\text{NO}$ structure ($V = 105 \text{ mV}$, $I = 0.55 \text{ nA}$). (b) The IET spectrum belonging to the topographic image with peaks at -106 meV and $+113 \text{ meV}$. The peak intensities are 12% and 8%, respectively. The spectrum is an average of 2 curves of 1 minute each. ($V_{\text{ref},\text{RMS}} = 14 \text{ mV}$, $f = 4.7 \text{ kHz}$).

These values are even closer to the values for the N - O stretch when the molecule is adsorbed flat to the tip apex (Table 5.4). The -106 meV peak has an intensity of 12% whereas the dip at positive voltage has an intensity of 8%. Although their intensity is higher than in Fig. 5.7(b), no peaks could be detected at $\pm 55 \text{ meV}$. This shows again that the IET behavior is more sensitive to the exact tip-sample configuration, than the imaging behavior is and can only be understood from detailed theoretical calculations.

Silver contaminated tip apex

In order to compare the behavior of an NO molecule adsorbed at a transition metal apex to a molecule on a silver terminated tip, a tungsten tip was repeatedly dipped into a Ag(100) substrate prior to bleeding in the NO gas at 20 K. When a molecule was expected to be adsorbed at the apex, IETS was performed over the bare Ag(100) surface and Fig. 5.10 shows a typical spectrum that is obtained. It has a peak at $+25 \text{ meV}$ and a dip at -23 meV . This spectrum looks very similar to the one observed for a CO molecule attached to a silver coated tungsten tip [10]. There, the molecule

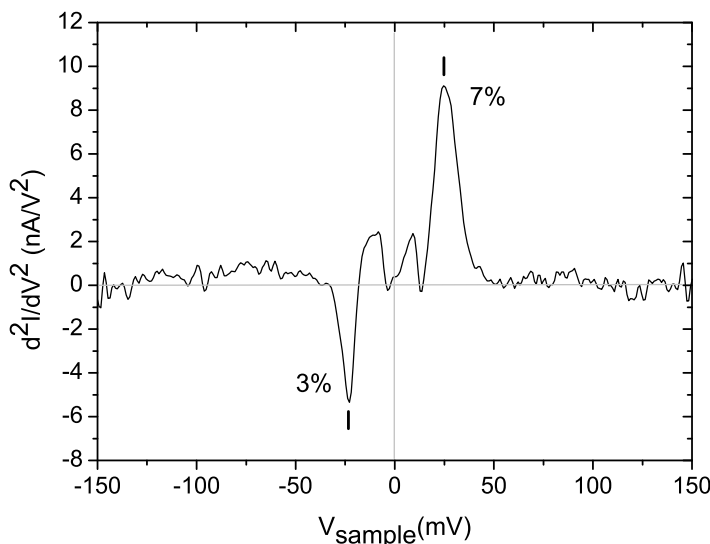


Figure 5.10: An IET spectrum taken with an NO terminated W tip over a clean Ag(100) substrate. Due to dipping, the tip apex probably consists of silver atoms from the sample. Peaks are observed at -23 meV and +25 meV with intensities of 3% and 7%, respectively (Measurement parameters: $V = 100$ mV and $I = 0.21$ nA, $V_{ref,RMS} = 12$ mV, $f = 1.8$ kHz. The spectrum is an average of 20 spectra of 10 s each.).

was adsorbed upright at the apex and the peak was attributed to its frustrated rotational mode. As opposed to CO, there is very little literature about the low energy vibrations of NO on silver. Experimentally, on the Ag(111) surface, the Ag - NO stretch for a vertically adsorbed molecule is reported around 30 meV [24] and it was theoretically calculated to be 22 meV [25], very close to the experimentally measured value. Although no value for the frustrated rotational mode of NO on silver has been reported, it usually lies close to the metal-molecule stretch. Hence, the observed mode at 24 meV can be attributed to either the R-mode or the Ag - NO stretch mode of the NO molecule standing upright at the silver tip apex. From Fig. 5.6, the preference for either mode depends on the MO of the molecule that contributes strongest to the current. If it is the $\pi_{2p_{xy}}^*$, the peak could be assigned to the R-mode and for the σ_{2p_z} it would be the Ag - NO stretch. Note that for unknown reasons, the peak at positive

sample bias has a larger intensity than that at negative sample bias.

5.3 Conclusion

In this chapter the IET signal of the NO on Rh(111) system was studied in relation to the functionalization of the tip. Based on the STM image, that is taken prior to performing spectroscopy, the orbitals of the NO molecule that dominate the tunneling current could be derived. For all different kind of tips used in this study, a zero-bias feature related to the phonons of tip and sample could be observed. On the other hand, only specific tip configurations showed loss peaks that could be related to the R-mode of the molecule on the surface. No other vibrational modes could be observed. From the topographic imaging, it is found that the R-mode can only be experimentally observed when the $\pi_{2p_{xy}}^*$ orbital of the NO on the surface has a strong contribution to the current. The symmetry of the $\pi_{2p_{xy}}^*$ wave function is similar to the symmetry of the movement of the atoms in the molecule in the R-mode. It is therefore suggested that the strength of the electron-phonon coupling between a molecular orbital and the molecule's vibrational mode depends on the similarity of their symmetry. Based on this assumption, the following selection rule is tentatively posed: *the molecular vibrations that can be excited in an IETS experiment must have a symmetry that is similar to the symmetry of the molecular orbital that is mainly contributing to the tunneling current.* However, unless it is known what molecular orbitals contribute to the current, this selection rule does not contain any predictive power. Although consistent with the experimental observation, this rule has to be theoretically confirmed.

In some cases, inelastic scattering of an electron from an NO molecule adsorbed flat against the tungsten tip apex was observed. The excited molecular vibrations are the W - NO stretch and the N - O stretch. The contribution of multiple molecular orbitals, that interfere among each other make the application of the intuitive selection rule impossible. As opposed to the observation of peaks when the molecule is adsorbed at the substrate, the molecular vibrations of the tip adsorbate showed up as dips at positive sample voltage. When adsorbed vertically at a silver terminated apex, however, the IET spectrum shows a peak at a positive sample bias of 25 meV, that is

related to either the Ag - NO stretch or the frustrated rotation of the NO molecule.

Finally, it is emphasized that decent theoretical support is desirable to get insight in several inelastic processes that are not well understood. Examples are the behavior of the zero bias feature, the interference effects among inelastic electron trajectories, the intensity of the peaks, the transition from peak to dip at positive sample voltages and the validity of the formulated selection rule.

References

- [1] T. W. Root, G. B. Fisher and L. D. Schmidt, ‘Electron energy loss characterization of NO on Rh(111). I. Coordination and Dissociation,’ *J. Chem. Phys.*, **85**, 4679–4686 (1986).
- [2] C. T. Kao, G. S. Blackman, M. A. van Hove and G. A. Somorjai, ‘The surface structure and chemical reactivity of Rh(111)-(2x2)-3NO by HREELS and dynamical LEED analysis,’ *Surf. Sci.*, **224**, 77–96 (1989).
- [3] G. Witte, ‘Low-energy dynamics of CO and NO chemisorbed on Rh(111),’ *J. Chem. Phys.*, **115**, 2757–2767 (2001).
- [4] G. J. Blyholder, ‘Molecular orbital view of chemisorbed carbon monoxide,’ *J. Phys. Chem.*, **68**, 2772–2777 (1964).
- [5] L. J. Lauhon and W. Ho, ‘Single-molecule vibrational spectroscopy and microscopy: CO on Cu(001) and Cu(110),’ *Phys. Rev. B*, **60**, R8525–R8528 (1999).
- [6] A. J. Heinrich, C. P. Lutz, J. A. Gupta and D. M. Eigler, ‘Molecule cascades,’ *Science*, **298**, 1381–1387 (2002).
- [7] J. R. Hahn and W. Ho, ‘Oxidation of a single carbon monoxide molecule manipulated and induced with a scanning tunneling microscope,’ *Phys. Rev. Lett.*, **87**, 166102 (2001).
- [8] T. Komeda, Y. Kim, M. Kawai, B. N. J. Persson and H. Ueba, ‘Lateral hopping of molecules induced by excitation of internal vibration mode,’ *Science*, **295**, 2055–2058 (2002).

5. STM-IETS on NO on Rh(111)

- [9] N. Nilus, T. M. Wallis and W. Ho, ‘Vibrational spectroscopy and imaging of single molecules: Bonding of CO to single palladium atoms on NiAl(110),’ *J. Chem. Phys.*, **117**, 10947–10952 (2002).
- [10] J. R. Hahn and W. Ho, ‘Single molecule imaging and vibrational spectroscopy with a chemically modified tip of a scanning tunneling microscope,’ *Phys. Rev. Lett.*, **87**, 196102 (2001).
- [11] F. Moresco, G. Meyer and K.-H. Rieder, ‘Vibrational spectroscopy of CO/Cu(211) with a CO terminated tip,’ *Mod. Phys. Lett. B*, **13**, 709–715 (1999).
- [12] J. Cerdá, private communication.
- [13] M. E. Taylor, ‘Inelastic processes in tunnelling electrodes,’ *Ultramicroscopy*, **42-44**, 215–222 (1992).
- [14] G. Witte, J. P. Toennies and C. Wöll, ‘Comparison of surface phonon dispersion curves for clean and hydrogen covered Rh(111) surfaces,’ *Surf. Sci.*, **323**, 228–240 (1995).
- [15] A. Eichler, K. P. Bohnen, W. Reichardt and J. Hafner, ‘Phonon dispersion relation in rhodium: Ab initio calculations and neutrons scattering investigations,’ *Phys. Rev. B*, **57**, 324–333 (1998).
- [16] L. Vitali, M. A. Schneider, K. Kern, L. Wirtz and A. Rubio, ‘Phonon and plasmon excitation in inelastic electron tunneling spectroscopy of graphite,’ *Phys. Rev. B*, **69**, R121414 (2004).
- [17] B. C. Stipe, M. A. Rezaei and W. Ho, ‘Single-molecule vibrational spectroscopy and microscopy,’ *Science*, **280**, 1732–1735 (1998).
- [18] N. Lorente, M. Persson, L. J. Lauhon and W. Ho, ‘Symmetry selection rules for vibrationally inelastic tunneling,’ *Phys. Rev. Lett.*, **86**, 2593–2596 (2001).
- [19] W. Ho, R. F. Willis and E. W. Plummer, ‘A vibrational frequency and intensity analysis of the bonding structure of N₂ on W(100),’ *Surf. Sci.*, **95**, 171–189 (1980).

- [20] H. Froitzheim, H. Ibach and S. Lehwald, ‘Surface vibrations of oxygen on W(100),’ *Phys. Rev. B*, **14**, 1362–1369 (1976).
- [21] J. R. Hahn, H. J. Lee and W. Ho, ‘Electronic resonance and symmetry in single-molecule inelastic electron tunneling,’ *Phys. Rev. Lett.*, **85**, 1914–1917 (2000).
- [22] M. T. M. Koper, R. A. van Santen, S. A. Wasileski and M. J. Weaver, ‘Field-dependent chemisorption of carbon monoxide and nitric oxide on platinum-group (111) surfaces: quantum chemical calculations compared with infrared spectroscopy at electrochemical and vacuum-based interfaces,’ *J. Chem. Phys.*, **113**, 4392–4407 (2000).
- [23] O. Hansen, J. T. Ravnkilde, U. Quaade, K. Stokbro and F. Grey, ‘Field-induced deformation as a mechanism for scanning tunneling microscopy based nanofabrication,’ *Phys. Rev. Lett.*, **81**, 5572–5575 (1998).
- [24] S. K. So, R. Franchy and W. Ho, ‘The adsorption and reactions of NO on Ag(111) at 80 K,’ *J. Chem. Phys.*, **91**, 5701–5706 (1989).
- [25] J. H. M. Gajdoš and A. Eichler, ‘Ab initio density-functional study of NO on close-packed transition and noble metal surfaces: I. molecular adsorption,’ *J. Phys.: Condens. Matter*, **18**, 1340 (2006).

Appendix A

Using a Lock-in amplifier to measure $\frac{dI}{dV}$ and $\frac{d^2I}{dV^2}$

Generally, given a signal $V(t)$ that may consist of many frequencies, a lock-in amplifier will measure the RMS value of the signal component $V_f(t)$ at frequency f . This is achieved by multiplying the signal $V(t)$ by a pure sine of frequency f . Mathematically, sine waves of different frequencies are orthogonal and average out to zero unless the frequencies are exactly the same.

In STM, the bias voltage between tip and sample is a DC voltage V_{DC} . In order to make use of the lock-in amplifier for spectroscopic purposes, an AC reference voltage $V_{ref} = V_{AC}\cos(2\pi ft)$ of frequency f , is added across the tunnel junction:

$$V = V_{DC} + V_{AC}\cos(2\pi ft). \quad (\text{A-1})$$

An $I(V)$ curve is taken by sweeping V_{DC} and recording the response I_{DC} . For every value of V_{DC} , the AC response I_{res} to V_{ref} is recorded by the lock-in amplifier. Although V_{ref} has a fixed amplitude V_{AC} and frequency f , I_{res} does not. This is illustrated in Fig. A.1, which is a zoom on the $I(V)$ curve of Fig. 2.4(b). The curve can be divided into 3 regions. In region 1 and 3, the $I(V)$ curve is linear with $\frac{dI}{dV}_1 < \frac{dI}{dV}_3$. Due to this linearity I_{res} also is a sinus of frequency f with an amplitude I_{AC} that is proportional to $\frac{dI}{dV}$. Hence, the I_{AC} is a measure for $\frac{dI}{dV}$. In region 2 however, the relationship is not linear any more. The response signal $I_{res,2}$ is a mixture of $I_{res,1}$

A. Using a Lock-in amplifier to measure $\frac{dI}{dV}$ and $\frac{d^2I}{dV^2}$

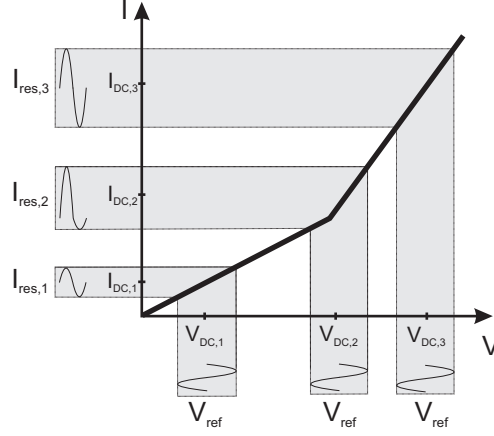


Figure A.1: The $I(V)$ curve showing a zoom on Fig. 2.4(b) can be divided in two linear regimes called 1 and 3, separated by a non-linear regime, named 2. In the linear regime the response I_{res} to a sinusoidal AC voltage V_{ref} of amplitude V_{AC} and frequency f remains sinusoidal with the same frequency. Its amplitude I_{AC} is proportional to $\frac{dI}{dV}$. In regime 2, the non-linearity gives rise to a response that consists of frequency f and all its higher harmonics.

and $I_{res,3}$. Fourier theory states that such a signal is described by a series of sinuses of frequency f and all higher harmonics $2f, 3f, 4f...$

To quantitatively understand why the f and the $2f$ signal as measured by the lock-in amplifiers are related to $\frac{dI}{dV}$ and $\frac{d^2I}{dV^2}$, $I(V)$ is decomposed in a Taylor expansion around V_{DC} :

$$I(V) = I(V_{DC}) + \frac{dI}{dV}(V - V_{DC}) + \frac{1}{2} \frac{d^2I}{dV^2}(V - V_{DC})^2 + \dots \quad (\text{A-2})$$

Combining A-1 and A-2:

$$I(V) = I(V_{DC}) + \frac{dI}{dV} V_{AC} \cos(2\pi ft) + \frac{1}{2} \frac{d^2I}{dV^2} V_{AC}^2 \frac{[1 + \cos(2\pi(2f)t)]}{2} + \dots \quad (\text{A-3})$$

The lock-in tuned to measuring f gives:

$$I_{AC,f} = \frac{\frac{dI}{dV} V_{AC,f}}{\sqrt{2}} \quad (\text{A-4})$$

and tuned to $2f$, it measures:

$$I_{AC,2f} = \frac{\frac{1}{4} \frac{d^2 I}{dV^2} V_{AC,f}^2}{\sqrt{2}} \quad (\text{A-5})$$

Thus the measured f and $2f$ components of the $I(V)$ curve by the lock-in amplifier are proportional to $\frac{dI}{dV}$ and $\frac{d^2 I}{dV^2}$, respectively. The $\sqrt{2}$ in the denominator is because the lock-in measures RMS values, not peak-to-peak values.

Appendix B

Other experimental structures

In addition to the experimentally obtained structures shown in chapter 3, this appendix discusses two additional adlayer configurations that were only occasionally observed and are therefore not well understood. The STM topographic image of Fig. B.1(a) is obtained after inserting the clean Rh(111) sample in the STM stage in a cold (< 20 K) and dilute ($\sim 2 \cdot 10^{-10}$ mbar) NO gas background. The obtained structure is determined to be a $(4 \times 4) - 1\text{NO}$ configuration. Note that, despite the relatively large number of vacant sites, no grain boundaries can be observed, i.e. the obtained $(4 \times 4) - 1\text{NO}$ structure consists of a single grain over a $45 \times 45 \text{ nm}^2$ area.

If we assume that the molecules only diffuse over the energetically most favorable hcp sites with a very low energy barrier, the formed adlayer configuration is fully determined by the lateral interactions. However, the calculated values for the interactions displayed in Table 3.2 are too large to play a role at these low temperatures: since diffusion is a thermally activated process, only interactions of the same order of magnitude as $k_b T$ can be overcome when two molecules are moving towards each other. Consequently, from Fig. B.1(a), the lateral interaction acting over a distance four times the lattice constant ($4 \times 2.69 \text{ \AA} = 10.8 \text{ \AA}$), can be estimated to be of the

B. Other experimental structures

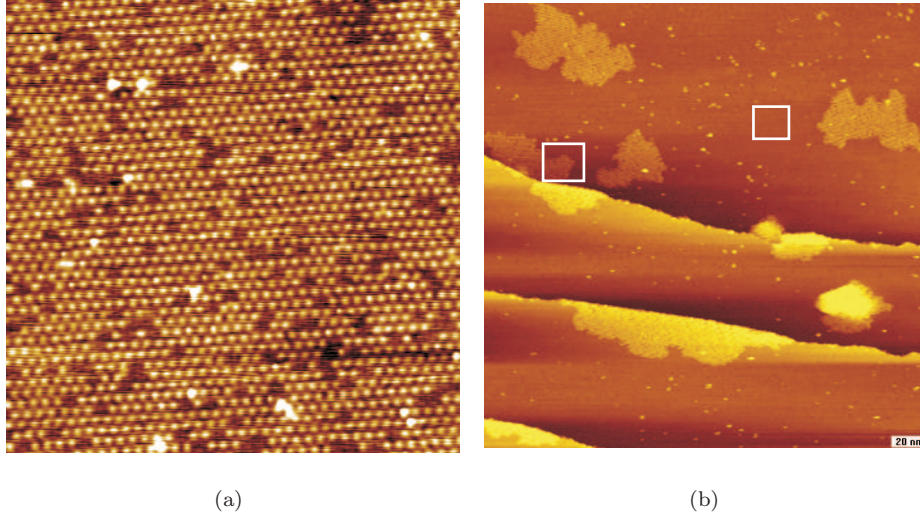
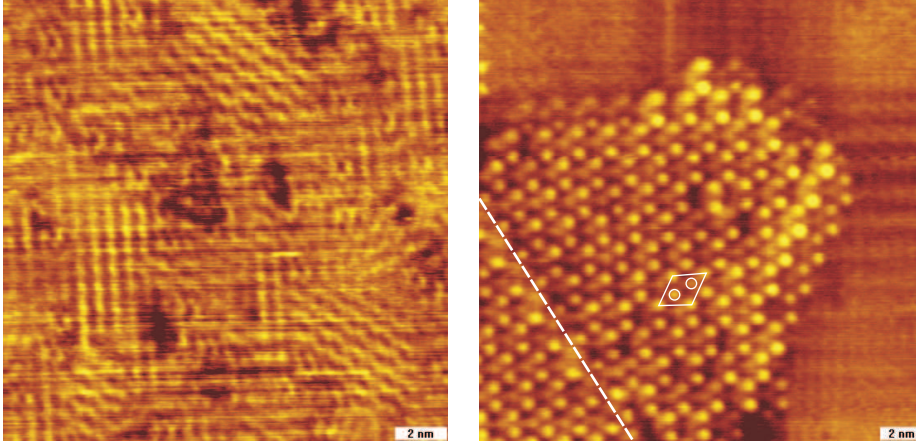


Figure B.1: (a) STM image ($45 \times 45 \text{ nm}^2$) taken after deposition of NO molecules at 5 K ($V = -198 \text{ mV}$, $I = 239 \text{ pA}$). (b) STM image ($244 \times 244 \text{ nm}^2$) of patches formed at 200 K ($V = 102 \text{ mV}$, $I = 385 \text{ pA}$). The right white box indicates the area where the image of Fig. B.2(a) is taken. Similarly, the left box refers to Fig. B.2(b).

order of 10 K or 0.1 kJ/mol, much smaller than could theoretically be determined. This way, lateral interactions can in principle be estimated as a function of distance by varying the temperature.

The weak point in the above reasoning is the assumption that the diffusion barrier is small compared to the lateral interactions. It is, however, more likely that the barrier by itself readily is too large for any diffusion to occur at these low temperatures. As a result, once adsorbed, the molecules cannot move over the surface and a disordered adlayer would be expected. It is not clear what mechanism made it possible for the $(4 \times 4) - 1\text{NO}$ configuration to form. Possibly the diffusion barrier is lower than it is assumed to be. Alternatively, the cold NO molecules could already feel some repulsive (dipole) forces when they are still free to move in the gas phase before adsorbing on the surface.

In Fig. B.1(b), another type of adlayer configuration is shown that is obtained in a way similar to the other structures in this thesis. In the image, three monatomic steps of the Rh(111) surface are visible. Moreover, patches are observed that seem to



(a)

(b)

Figure B.2: (a) $17 \times 17 \text{ nm}^2$ zoom in between the patches as indicated in Fig. B.1(b). (b) $21 \times 21 \text{ nm}^2$ zoom on the patch of Fig. B.1(b). The white dashed line marks a grain boundary within the patch and the white parallelogram indicates the unit cell of the structure. Scanning parameters for both images: $V = 102 \text{ mV}$, $I = 395 \text{ pA}$.

have a preference to nucleate at the edges of these steps. The white boxes in the right and left of the image denote the areas where the images of Fig B.2(a) and Fig B.2(b) are taken, respectively.

Fig. B.2(a) is taken in between the patches and shows a zigzag-like structure, that is determined to be the well-know $0.50 \text{ ML } (4 \times 2) - 4\text{NO}$ configuration (see Fig. 3.1). Fig. B.2(b) is a zoom on the patch, which consists of two domains that are separated by the dashed white line to guide the eye. The bright dots are arranged in a honeycomb-like lattice which qualitatively resembles the $(2 \times 2) - 2\text{NO}$ structure (see Fig. 3.4) but has a unit cell that is about three times larger. Furthermore, the corrugation of the structure of the patch is $d \approx 100 \text{ pm}$, about four times higher than the corrugation of the $(4 \times 2) - 4\text{NO}$ structure next to it. Note that in the middle of the hexagons, another dot can be discerned which is less bright than the dots that constitute the hexagon itself. In the image, the (6×6) unit cell is indicated. The parallelogram has a bright dot at each of its corners and embodies a bright and the less bright dot, as indicated by the circles. If each dot would represent one

B. Other experimental structures

NO molecule, the structure would have a coverage of only 0.08 ML. As the coverage of the neighboring $(4 \times 2) - 4\text{NO}$ structure is 0.50 ML, the system is either out of equilibrium or a bright dot represents more than one molecule so that the structure's actual coverage is higher than the suggested 0.08 ML.

There are three reasons to assume that this configuration is metastable. A metastable structure forms either when the adsorption rate is higher than the diffusion rate so that equilibrium cannot be achieved or when the electronic properties of the adsorption sites on the rhodium surface have changed due to step edges or (subsurface) impurities. The first reason is that this configuration is only observed sporadically on some specific spots on the surface. Secondly, its coverage does not seem to be related to the 0.50 ML coverage of the $(4 \times 2) - 4\text{NO}$ structure and finally, it did not arise from the kinetic Monte Carlo simulations of chapter 3.

Summary

The role of the electron trajectory in scanning tunneling microscopy

elastic and inelastic tunneling through NO on Rh(111)

In this thesis the system of nitric monoxide (NO) adsorbed on the Rh(111) sample surface is used as a model system for studying different phenomena. Binding upright on specific adsorption sites on the substrate, the small NO molecule is a good candidate to use for well-defined scanning tunneling microscopy (STM) experiments. Moreover, the ability of rhodium to efficiently transform the pollutive NO gas into less hazardous compounds is used in car catalytic converters and motivates the choice for this combination of metal and molecule.

The catalytic working of the rhodium is a result of the way the molecules bind to the metal surface upon adsorption. Lateral interactions between neighboring molecules on the surface can influence this bond and hence the catalytic functioning of the metal.

In this work, the lateral interactions of NO molecules adsorbed on the Rh(111) surface are calculated. It is shown that pairwise and three particle interactions are important and that four particle interactions do not play a role. Although the interactions are obtained from total energy calculations of the structures at $T = 0$ K, at finite temperatures it is the structure with lowest free energy that forms. The difference between the total energy and the free energy arises from entropy effects. To take these effects into account, kinetic Monte Carlo simulations using the derived

lateral interactions are performed. The resulting structures can be directly compared to the molecular arrangements observed in the STM experiment. The configuration of the first three structures that form for increasing coverage is the same both experimentally and theoretically. In all three structures, the molecules only occupy the fcc and hcp adsorption sites. Yet, at high coverage, at which the top adsorption sites become occupied, a discrepancy arises.

The imaging of the molecules in the STM experiment is determined by the tunneling current between tip and sample. As opposed to optical or electron microscopy, this current does not only depend on the properties of the sample but also on the type of tip the image is taken with. Small changes of the tip may lead to different appearances of the ordered NO structures.

In this study, the used tungsten tip apexes are clean or contaminated by an NO molecule or one of its constituent atoms. To systematically study the variety of appearances, STM images have been simulated using these different kind of tips. Since the adlayer configuration of the substrate is known, comparing the theoretical and the experimental images gives a hint on the type of tip the image is scanned with.

For all tips, the tunneling current results from electrons taking different orbital pathways. The contribution of these pathways cannot just be added, since, due to the wave-like nature of particles in quantum mechanics, different electron pathways give rise to interference effects. In some cases these interference effects are so strong that the bright spots in the STM image do not coincide with the position of the NO molecules in the structure. Therefore, care must be taken when using STM for the determination of adlayer configurations.

Finally, the STM can also be used to measure the vibrations of a single molecule in the tunnel junction. In inelastic electron tunneling spectroscopy (IETS), the onset at which a tunneling electron can lose energy to a vibrational quantum of the molecule can be measured in the I - V curve. However, not all of the molecular vibrations can be observed and the selection rules for IETS are unknown. Proper knowledge of these selection rules, however, will greatly help to understand electron transport through single molecules in general.

As the simple diatomic NO molecule only has a few vibrational modes, the ob-

tained vibrational spectra can be easily interpreted. Prior to taking an IET spectrum, an image is made from which the functionalization of the tip can be derived as described above. Next to the nature of the tip apex, the theory gives insight in the molecular orbitals that mainly carry the tunneling current.

Only specific tip configurations showed loss peaks that could be related to the vibration in which the molecule attempts to rotate. The molecule-metal bond, however, frustrates the rotational movement. Next to this so-called frustrated rotation, no other vibrational modes could be observed. The frustrated rotational mode seems to be active only when the $\pi_{2p_{xy}}^*$ orbital of the molecule has a strong contribution to the current. As the symmetry of the wave function of the $\pi_{2p_{xy}}^*$ orbital is similar to the movement of the atoms in the molecule in the frustrated rotational vibration, the following selection rule is tentatively posed: the molecular vibrations that can be excited in IETS must have a symmetry that is similar to the symmetry of the molecular orbital wave function that is mainly contributing to the current. However, this suggested selection rule has to be confirmed theoretically.

In some cases, inelastic scattering of an electron from an NO molecule adsorbed flat at the tip apex was observed. The excited molecular vibrations are the W - NO stretch and the N - O stretch. The contribution to the tunneling current of multiple molecular orbitals that interfere among each other, make the application of the intuitive selection rule impossible. Therefore, a decent theoretical framework is indispensable in order to fully understand the mechanism of STM-IETS.

Samenvatting

Het systeem van stikstofmonoxide (NO) moleculen geadsorbeerd op een Rh(111) oppervlak is in dit proefschrift gebruikt als een model systeem voor de studie van verschillende fenomenen. Aangezien het NO molecuul recht op specifieke posities op het rhodium oppervlak adsorbeert, is het een geschikte kandidaat voor goed gedefinieerde experimenten met behulp van een scanning tunneling microscoop (STM). Daarnaast wordt de keuze voor dit systeem sterk gemotiveerd door de toepassing van rhodium in katalysatoren van auto's. Wanneer het schadelijke NO gas in contact komt met het rhodium oppervlak wordt het omgezet in minder giftige gassen zoals stikstof, water en koolstofdioxide. Deze katalytische werking van het rhodium komt voort uit de manier waarop een NO molecuul zich bindt aan het metaaloppervlak. Echter, wanneer er verscheidene moleculen op het oppervlak aanwezig zijn, zullen hun onderlinge interacties de binding van het molecuul met het metaal beïnvloeden waardoor de katalytische werking van het rhodium verandert.

In dit werk is getracht de onderlinge wisselwerking te berekenen tussen NO moleculen die geadsorbeerd zijn op een Rh(111) oppervlak. Het blijkt dat alleen paarsgewijze en drie deeltjes interacties belangrijk zijn. Hogere orde interacties spelen geen rol van betekenis. Ondanks het feit dat de moleculaire wisselwerking wordt afgeleid van de totale interne energie van geordende structuren van NO moleculen bij $T = 0$ K, is het de structuur met minimale vrije energie die zich zal vormen bij eindige temperatuur. Het verschil tussen de interne en de vrije energie komt voort uit de entropie van de geadsorbeerde laag. De berekende moleculaire interacties worden gebruikt in kinetische Monte Carlo simulaties waarbij de entropische effecten worden meegenomen in de bepaling van de moleculaire structuren. Deze structuren kunnen

één op één worden vergeleken met de in het STM experiment waargenomen ordening van de moleculen. De configuratie van de eerste drie structuren die zich vormen bij oplopende bedekkingsgraad van het oppervlak zijn gelijk in zowel het experiment als in de simulatie. In al deze structuren zitten de moleculen geadsorbeerd in de fcc en hcp positie van het rhodium oppervlak. Er treedt echter een discrepantie op bij hogere bedekkingsgraden wanneer de top posities van het oppervlak worden bezet.

De verschijningsvorm van de moleculaire structuren in het STM experiment wordt bepaald door de tunnel stroom die loopt tussen de tip en het oppervlak. Deze stroom wordt niet alleen bepaald door de eigenschappen van het oppervlak zoals in een licht- of een elektronenmicroscop, maar ook door de eigenschappen van de tip waarmee de scan wordt gemaakt. Kleine variaties in de eigenschappen van de tip kunnen tot verschillende topografische beeltenissen van de geordende structuur leiden.

De in deze studie gebruikte wolfram tips zijn schoon of hebben een NO molecuul, een N atoom of een O atoom geadsorbeerd aan hun uiteinde. Om een relatie te kunnen leggen tussen de verschillende verschijningsvormen van een structuur en de gebruikte STM tips zijn STM afbeeldingen gesimuleerd. Aangezien de configuratie van de geadsorbeerde NO structuur steeds gelijk is, kan door een vergelijk tussen experiment en theorie kwalitatief worden bepaald met welk soort tip de afbeelding is genomen.

Het blijkt verder dat voor alle gebruikte tips de tunnel stroom bestaat uit verschillende elektronenpaden tussen toestanden in de tip en in het substraat. Door het golfkarakter van deeltjes in de kwantum mechanica kunnen de bijdragen van de verschillende paden niet worden opgeteld maar is er sprake van interferentie. In enkele gevallen is deze interferentie zo sterk dat de hoogste punten in het topografische STM plaatje niet overeenkomen met de positie van de NO moleculen. Het is daarom raadzaam zorgvuldigheid in acht te nemen wanneer de STM gebruikt wordt voor de bepaling van geadsorbeerde moleculaire structuren.

Tenslotte kan de STM ook gebruikt worden om de vibraties van één enkel molecuul in de tunnel junctie te meten. In inelastic electron tunneling spectroscopy (IETS) kan het moment waarop een tunnel elektron genoeg energie heeft om een vibrationeel kwantum van het molecuul aan te slaan worden bepaald uit de I - V curve. Echter,

niet alle moleculaire vibraties kunnen worden waargenomen en de selectie regels van deze techniek zijn onbekend. Goede kennis van deze regels kan daarentegen enorm bijdragen aan het fundamentele begrip van elektrontransport door één enkel molecuul. Omdat het simpele twee-atomige NO molecuul slechts een paar verschillende manieren van trillen heeft, zijn de verkregen IET spectra eenvoudig te interpreteren. Voordat een vibrationeel spectrum wordt genomen, wordt er eerst een afbeelding van het molecuul gemaakt. Zoals hierboven beschreven kan de aard van het uiteinde van de tip worden bepaald met behulp van de verschijningsvorm van het molecuul op de scan. Daarnaast geeft de theorie inzicht in de moleculaire orbitalen die het belangrijkste deel van de tunnel stroom dragen.

Alleen met bepaalde tip configuraties zijn vibrationele pieken te zien die gerelateerd kunnen worden aan een vibratie waarbij het molecuul een rotatie probeert uit te voeren. Echter, de binding van het molecuul met het rhodium oppervlak frustreert de volledige uitvoering van deze beweging. Naast deze gefrustreerde rotatie konden geen andere vibraties worden waargenomen. Het blijkt dat de gefrustreerde rotatie alleen kan worden aangeslagen wanneer de $\pi_{2p_{xy}}^*$ orbitaal van het NO molecuul sterk bijdraagt aan de tunnel stroom. Aangezien de symmetrie van de golffunctie van de $\pi_{2p_{xy}}^*$ orbitaal gelijk is aan die van de beweging van de atomen in het NO molecuul dat de gefrustreerde rotationele vibratie uitvoert, kan de volgende selectieregel worden gesuggereerd: in IETS kunnen alleen die moleculaire vibraties worden aangeslagen die een symmetrie hebben die gelijk is aan de symmetrie van de golffunctie van het moleculaire orbitaal dat het sterkst bijdraagt aan de tunnel stroom. Echter, om deze intuïtieve selectieregel echt van kracht te kunnen laten worden is een goede theoretische onderbouwing vereist.

In sommige gevallen konden vibrationele pieken worden waargenomen die gerelateerd waren aan vibraties van een NO molecuul dat plat tegen de tip geadsorbeerd is. De aangeslagen moleculaire trillingen waren de strekvibraties van de W - NO en de N - O bindingen. De toepassing van de hierboven geformuleerde selectieregel wordt in dit geval bemoeilijkt door het feit dat er verscheidene moleculaire orbitalen bijdragen aan de tunnel stroom. Voor een volledig begrip van het mechanisme van IETS is daarom een gedegen theoretisch model onmisbaar.

Dankwoord

Als ik mijn afstudeerperiode meetel, heb ik ruim vijfeneenhalf jaar rondgelopen binnen de vakgroep die transformeerde van 'fysica van oppervlakken en grenslagen' (FOG) onder leiding van professor Hidde Brongersma naar 'molecular materials and nanosystems' (M2N) onder leiding van professor René Jansen. Ik heb het deze periode altijd goed naar mijn zin gehad. Een promotie doe je niet alleen en ik wil iedereen die er op de een of andere manier aan heeft bijgedragen hierbij dan ook hartelijk bedanken.

In het bij zonder wil ik mijn copromoter Kees Flipse bedanken voor het enthousiasme waarmee hij mij altijd weer heeft weten te motiveren. Kees staat dicht bij zijn promovendi en heeft altijd tijd om zaken -van welke aard dan ook- te bespreken. Ook op persoonlijk vlak was het vaak erg gezellig. Vele gespreksonderwerpen hebben de revue gepasseerd in cafés en hotels tijdens dienstreizen naar het buitenland. Kees, bedankt!

Hoewel we inhoudelijk weinig raakvlakken hebben, heb ik mijn promotor René Janssen als erg prettige persoonlijkheid ervaren. Ondanks je overvolle agenda, maak je toch nog voor iedereen tijd. Ik wil je daarom erg bedanken dat je het ontwerp van mijn proefschrift tijdens de kerstvakantie hebt doorgelezen!

I would also like to address a special word of thanks to Jorge Iribas Cerdá. Without his contributions, chapter 4 and parts of chapter 5 would not be the way they are now. He was always prepared to answer any of my (sometimes very basic!) questions. I enjoyed my visit to Madrid and it was very nice working with you.

Daarnaast wil ik ook Tonek Jansen en Cristina Popa hartelijk danken voor de samenwerking. Dankzij hun bijdrage aan hoofdstuk 3 is het een veel mooier geheel geworden.

Een experimenteel natuurkundige komt vaak technische problemen tegen met zijn meetopstelling. Het was altijd erg prettig om met Gerard Wijers samen te werken en te denken. Als je hem een knullig ontwerpje gaf van iets wat je graag wilde hebben, dan was het meestal de volgende dag klaar. Bovendien denk ik dat hij de LT-STM beter kent dan de gemiddelde service engineer van Omicron. De opstelling is zo vaak open geweest dat we hem nu kunnen dromen. De tweejarige etentjes met Gerard, Kees en mijzelf die daarbij kwamen kijken, zou ik graag in de toekomst willen voortzetten! Ook wil ik Rein Rumphorst danken zijn hulp bij elektronische vragen en alle zin en onzin des levens. Tenslotte ben ik dank verschuldigd aan Wijnand Dijkstra, met name voor de hulp met onze rekencomputers.

Ook al de overige leden van de groep wil ik graag bedanken. In het bijzonder mijn kamergenoten, Gheorghe Tănasă en Jiří Červenka. We hebben altijd veel gelachen en onze kamer altijd redelijk kunnen verdedigen tegen Rik van Laarhoven, alias de tennisballen terrorist (ik hoop dat de ramen van ons huis wel veilig zijn nu hij naast ons komt wonen). Ook wil ik Nick Podaru niet vergeten. Met hem kon je altijd praten over auto's en vissen. Het weekend in Luxemburg was erg gezellig! Daarnaast wil ik Erwin Rossen en Ondřej Vaculík nog bedanken voor het werk dat ze samen met mij hebben gedaan. Altijd als ik Erwin aan zag komen met een vraag, wist ik dat dat die niet binnen vijf minuten opgelost zou zijn. Verder dank aan Jean-Michel Wulveryck, Juan Amir voor de (meestal ongevraagde) muziek, Hans Gommans, Marco de Ridder, Frank Janssen, Ron Willems, Martijn Kemerink, Marta Fonrodona, Klára Maturová, Alexandre Nardes, Dimitri Charrier, Yinxin Liang, Erik Roeling en Kevin van de Ruit. Simon Mathijssen wil ik nog speciaal bedanken voor de scènes achter het raam. Daarnaast wil ik de (ex-)leden van Calipso wil ik bedanken voor de gezelligheid tijdens de koffie.

Graag wil ik ook mijn familie bedanken voor de belangstelling en steun tijdens mijn promotie en de jaren die eraan vooraf gingen, in het bijzonder mijn lieve Dorine voor het aanhoren van de dagelijkse beslommeringen van mijn werk: heel fijn dat je er voor me bent!

Curriculum Vitae

- December 8, 1978 Born in Geldrop, the Netherlands
- 1991 - 1997 Grammar school, St. Willibrord Gymnasium, Deurne
- 1997 - 2003 M. Sc. (cum laude) in applied physics, Eindhoven university of technology, Eindhoven
- Traineeship at ASML, Veldhoven. Subject: *Comparison of resist line measurements by SEM and AFM*, supervised by prof. dr. P. M. Koenraad
- Traineeship at the laboratoire de physique des gaz et des plasmas (LPGP), université de Paris-sud, Orsay (Paris), France. Subject: *Design of a coaxial set-up for the ionization of pulverized vapor using microwave radiation*, supervised by dr. C. Boisse-Laporte and prof. dr. ir. G. M. W. Kroesen.
- Master thesis project at the group of physics of surfaces and interfaces (FOG) of the department of applied physics, Eindhoven university of technology, Eindhoven. Subject: *Formation of tungsten nanocontacts*, supervised by dr. ir. C. F. J. Flipse and prof. dr. H. H. Brongersma.
- 2003 Researcher at the institut für zuverlässigkeit von bauteilen und systemen (IZBS), universität Karlsruhe, Karlsruhe, Germany. Subject: *Atomistic simulations of the formation and destruction of nanoindentation contacts in tungsten*, supervised by prof. dr. rer. nat. P. Gumbsch.
- 2003 - 2008 PhD project at the group of molecular materials and nanosystems (M2N) of the department of applied physics, Eindhoven university of technology, Eindhoven. Subject: *The role of the electron trajectory in scanning tunneling microscopy: elastic and inelastic tunneling through NO on Rh(111)*, supervised by dr. ir. C. F. J. Flipse and prof. dr. ir. R. A. J. Janssen.

